Electrolyte solutions at heterogeneously charged surfaces

Von der Fakultät für Mathematik und Physik der Universität Stuttgart zur Erlangung der Würde eines Doktors der Naturwissenschaften (Dr. rer. nat.) genehmigte Abhandlung

Vorgelegt von

Maximilian Otto Mußotter

aus Bietigheim-Bissingen

Hauptberichter:	Prof. Dr. Siegfried Dietrich
Mitberichter:	Prof. Dr. Christian Holm
Tag der mündlichen Prüfung:	27. Juli 2020

Institut für Theoretische Physik IV der Universität Stuttgart und
Max-Planck-Institut für Intelligente Systeme, Stuttgart

2020

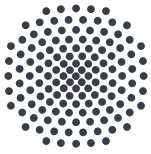

University of Stuttgart
Germany

MAX PLANCK INSTITUTE
FOR INTELLIGENT SYSTEMS

Erklärung

Hiermit erkläre ich, Maximilian Mußotter, dass ich diese Arbeit selbständig verfasst habe, dass ich keine anderen als die ausdrücklich bezeichneten Hilfsmittel benutzt und alle wörtlich oder sinngemäß aus anderen Werken übernommenen Aussagen als solche gekennzeichnet habe und dass die eingereichte Arbeit weder vollständig noch in wesentlichen Teilen Gegenstand eines anderen Prüfungsverfahrens gewesen ist.

Stuttgart, den 28.08.2020

Maximilian Mußotter

Contents

Index of abbreviations

DFT density functional theory

FMT fundamental measure theory

LDA local density approximation

SGA square gradient approximation

WDA weighted density approximation

MCSL Mansoori-Carnahan-Starling-Leland

EDL electric double layer

PB Poisson-Boltzmann

PM primitive model

HNC hypernetted chain

MSA mean spherical approximation

RPA random phase approximation

TIRM total internal reflection microscopy

GIXD grazing incidence X-ray diffraction

Zusammenfassung

In zahllosen Forschungsbereichen und Anwendungen ist das Verständnis des Verhaltens und der Struktur von Fluiden, d. h. Flüssigkeiten oder Gasen, von entscheidender Bedeutung. So spielen Fluide beispielsweise in Batterien und Kondensatoren [1, 2] wie auch in biologischen Systemen [3] oder sogar in Bereichen der Photovoltaik und Katalysatoren [4, 5] eine Schlüsselrolle. Vor allem die Besonderheiten heterogener Systeme, also von Systemen mit Grenz- oder Oberflächen, sind dabei ausschlaggebend für eine Vielzahl von Phänomenen. Zusätzlich sind in natürlichen Systemen Ladungsträger und damit elektrostatische Wechselwirkungen allgegenwärtig. Sie verkomplizieren nicht nur jeglichen Versuch einer Untersuchung solcher Systeme, sie führen zudem zu einer Reihe weiterer interessanter Effekte, deren genaues Verständnis intensiver Forschung bedarf. In großen Teilen solcher Forschungsarbeiten, die sich mit Fluiden in Kontakt mit festen Substraten beschäftigen, werden Näherungen und Einschränkungen verwendet. Eine typische Vereinfachung ist dabei, dass das Substrat als homogen bezüglich der Interaktionen zwischen Fluid und Wand betrachtet wird. Auf der einen Seite macht dies die mathematische Beschreibung solcher Systeme signifikant einfacher, auf der anderen Seite fehlt oftmals die experimentelle Information über die genaue Oberflächenbeschaffenheit der untersuchten Substrate. Für den Fall ungeladener Oberflächen und neutraler Fluide ist diese Näherung durchaus vernünftig, da die Längenskala, auf der die Einflüsse eventueller Heterogenität abklingen, durch die Bulk-Korrelationslänge gegeben ist. Der Ausdruck „Bulk“ bezeichnet hier ein homogenes System in Abwesenheit sämtlicher äußerer Einflüsse, gewissermaßen ein unendlich ausgedehntes System des betroffenen Materials. Sogenannte Bulk-Eigenschaften ergeben sich also stets durch innere Eigenschaften des Materials. Diese Bulk-Korrelationslänge liegt, fernab von Phasenübergängen, in der Größenordnung einiger Partikeldurchmesser, sie ist also von so kurzer Reichweite, dass Inhomogenitäten vernachlässigbar sind. Im Falle von elektrostatischen Wechselwirkungen zwischen einer geladenen Wand und Fluiden, die Ladungsträger beinhalten, ist die relevante Längenskala jedoch durch die Debye-Länge gegeben. Diese ist, vor allem im Falle geringer Salzkonzentrationen, sogenannter verdünnter Elektrolytlösungen, deutlich größer als alle anderen

Längenskalen, die durch Partikelgrößen gegeben sind. Außerdem sind typischerweise auch Inhomogenitäten innerhalb der Verteilung von Oberflächenladungen in der Größenordnung der Debye-Länge voneinander entfernt. Daher ist die oben angesprochene Näherung einer homogenen Oberfläche in solchen Fällen nicht haltbar. Die Vielzahl von Effekten, die bei genauerer Betrachtung mit solchen Inhomogenitäten in Verbindung gebracht werden, stellen den Ausgangspunkt der hier vorgestellten Forschung dar. In der vorliegenden Thesis wurde daher eine planare Wand untersucht, die räumlich variierend chemisch und elektrostatisch mit einer benachbarten Elektrolytlösung wechselwirkt. Insbesondere wurden die Effekte auf die Struktur des Fluides, ausgedrückt durch Teilchenzahldichten, untersucht. Hierfür wurde der mathematische Rahmen der Dichtefunktionaltheorie gewählt, da dieser sich schon wiederholt als leistungsfähiges Werkzeug für Studien gerade solcher Teilchenzahldichten gezeigt hat. Nach einer ausführlichen Motivation und Erläuterung der Fragestellung in Kap. 1 werden die Grundlagen dieser Methode in Kap. 2 eingeführt und erklärt. Basierend auf diesen Ausführungen werden in den Kap. 3 und 4 dann zwei verschiedene Ansätze besprochen, die sich in erster Linie in der Komplexität der zugrundeliegenden Beschreibung des Fluides unterscheiden. In diesen Kapiteln werden die Ergebnisse der hier vorgestellten Forschung präsentiert und eingeordnet. Die Resultate der beiden Ansätze wurden in großen Teilen schon an anderer Stelle veröffentlicht [6, 7].

Mit der oben genannten Motivation wurde in Kap. 3 zunächst eine einfache, grobe Beschreibung des Fluides gewählt. Das Fluid und seine Komponenten wurden hier mit einer quadratischen Gradientennäherung im Stile von Cahn-Hilliard beschrieben (siehe Abschn. 3.2.2). Darüber hinaus wurden die heterogenen chemischen oder elektrostatischen Interaktionszentren, deren Anordnung innerhalb des Modells frei gewählt werden konnten, in ihrer Stärke begrenzt, sodass sie schwach genug waren, um eine lineare Antwort der Teilchenzahldichten anzunehmen. Dies ermöglichte es, geschlossene analytische Ausdrücke für die resultierenden Teilchenzahlprofile herzuleiten (siehe Abschn. 3.2.3). Diese wiederum wurden im Verlaufe dieses Kapitels analysiert, um erste, fundamentale Erkenntnisse zu den Effekten von chemisch oder elektrostatisch inhomogenen Wänden und zur Kopplung von Ionen- und Lösungsmittelvariationen zu erhalten. Zunächst wurden einzelne, isolierte, punktförmige Interaktionszentren untersucht. Deren Analyse zeigte deutliche Unterschiede in den Reaktionen des Fluides auf chemisch im Vergleich zu elektrostatisch wechselwirkenden Wänden. Wie eingangs erwähnt, wurde für chemische Interaktionen zwischen Substrat und Fluid ein Abklingen der Variationen der Dichte auf der Längenskala der Bulk-Korrelationslänge ξ gefunden. Zudem waren die Veränderungen in allen drei Teilchenzahldichten, die des Lösungsmittels sowie die der beiden Ionen, in ihrem Verlauf proportional zueinander (siehe Abb. 3.2, 3.3 und 3.4). Im Gegensatz hierzu wurde im Fall von elektrostatischen Wechselwirkungen zwischen Wand und Fluid keinerlei Veränderung

bei den Teilchenzahldichten des Lösungsmittels gefunden. Die Ionen zeigten dagegen deutliche Reaktionen auf eine elektrostatische Wechselwirkung, wobei ihre Veränderungen in den Dichten identisch waren, mit jeweils unterschiedlichen Vorzeichen für die Ko- und die Gegenionen. Außerdem konnte, wie ebenfalls eingangs ausgeführt, ein Unterschied im Abklingverhalten festgestellt werden, wobei die Bulk-Korrelationslänge durch die Debye-Länge $1/\kappa \gg \xi$ ersetzt wurde (siehe Abb. 3.5). Durch das Einführen einer zweiten Längenskala in Form eines ausgedehnteren Interaktionsgebietes konnte die Wechselwirkung verschiedener Längenskalen analysiert werden. Die Betrachtung verschiedener Kombinationen von Größenordnungen ergab, dass die Ausdehnung der Oberflächenstruktur die Form des Fluides signifikant beeinflussen kann. Dominiert für eine gegebene Struktur, bzw. Ausdehnung der Interaktionsfläche eine interne Längenskala des Fluides, also die Bulk-Korrelationslänge oder die Debye-Länge, so ähneln die resultierenden Dichteprofile stark denen, die sich für punktförmige Interaktionsstrukturen ergeben. Wächst hingegen die Längenskala der Oberflächenstruktur, so steigt deren Einfluss auf den Verlauf der Dichtevariationen bis hin zu Dichteprofilen, die streng der Form der Interaktionen auf der Oberfläche folgen, für den Fall, dass deren Ausdehnung die dominierende Längenskala darstellt (siehe Abb. 3.7). Zuletzt wurde dieser erste, einfache Ansatz zur Beschreibung der Elektrolytlösung im Falle einer regelmäßigen, hexagonalen Verteilung von gaußförmigen Interaktionszentren betrachtet. Eine derartige Verteilung der Interaktionen entspricht der, die z. B. in Kristallen zu erwarten wäre. Erneut zeigte sich der starke Einfluss der Ausdehnung der Interaktionsgebiete auf die Struktur des benachbarten Fluides. Außerdem zeigte sich hier, dass die Distanz benachbarter Interaktionszentren die Bedeutung höherfrequenter Dichtefluktuationen, also Fluktuationen mit größeren Werten der lateralen Wellenzahl $|\boldsymbol{q}_{\parallel}|$, beeinflusst (siehe hierzu Abb. 3.8). In Anbetracht der Simplizität des in diesem Kapitel verwendeten Modells lässt sich an dieser Stelle festhalten, dass die Menge an beobachteten Phänomenen beachtlich ist.

Im folgenden Kap. 4 wurden die Erkenntnisse aus der vorausgegangenen Studie genutzt, um das verwendete Model zur Beschreibung der Elektrolytlösung zu verfeinern und damit genauere, realistischere Ergebnisse zu erhalten. Anstatt, wie bislang, quasi punktförmige Partikel zu betrachten, wurde die Methodik der Dichtefunktionaltheorie um die Konzepte der „fundamental measure theory“ (FMT) erweitert. In dieser werden, anstatt die tatsächlichen Dichteverläufe zu betrachten und in den Berechnungen zu verwenden, geometrische Überlegungen (Kugelvolumen, Kugeloberfläche) genutzt, um gemittelte, sogenannte gewichtete Dichten zu bestimmen, die in der weiteren Berechnung des Fluidverhaltens genutzt werden. Diese Variante sorgt für eine automatische Beschreibung der Partikel in Form von harten, undurchdringlichen Kugeln (siehe Abschn. 4.2). Daher sind in diesem zweiten Model alle internen Wechselwirkungen zwischen den Par-

tikeln und auch zwischen den Partikeln und dem Substrat, also alle Wechselwirkungen, die nicht durch die Elektrostatik erzeugt werden, rein repulsiv. Darüber hinaus wurden hier die Einschränkungen bezüglich der Stärke der Interaktionen zwischen Substrat und Fluid aufgehoben, was den in diesem Kapitel verwendeten Ansatz deutlich realistischer und umfangreicher macht. Allerdings führten diese Änderungen auch dazu, dass keine geschlossenen analytischen Ausdrücke mehr bestimmt werden konnten und das Verhalten des Fluides numerisch bestimmt werden musste. In einem ersten Schritt bestätigte die Untersuchung von homogen geladenen Oberflächen in Abschn. 4.3.2 die Beobachtungen aus dem vorangegangen Kapitel. Alle Profile zeigten exponentiell abklingendes Verhalten für größer werdende Entfernungen zur Wand, wobei die Längenskala dieses Abklingens durch die Debye-Länge $1/\kappa$ gegeben wurde. Zusätzlich zeigten in diesem Fall alle Dichteprofile die für harte Kugeln an harten Oberflächen typische Schichtstruktur. Die bisherigen Ergebnisse aus Kap. 3 erweiternd wurde hier zudem eine qualitative Änderung der Reaktion der Teilchenzahldichten für ausreichend große Wandladungen gefunden. Für geringe Stärken der Wandladung trat noch, wie auch schon im vorangegangenen Kap. 3, eine lineare Antwort des Systems auf die Oberflächenladung auf. Für große Wandladungen wurde jedoch ein zweiter Bereich beobachtet, in welchem die Lösungsmittelteilchen durch die Gegenionen nahe der Oberfläche verdrängt wurden. Dies entspricht einem qualitativ anderen Verhalten und stellt den Übergang in einen Bereich nicht-linearen Fluidverhaltens dar (siehe Abb. 4.2, 4.3, und 4.4). Um von einer homogenen Wandladungsverteilung hin zu heterogenen Ladungsstrukturen zu gelangen, wurde im Anschluss zunächst der Fall einer eindimensionalen, sinusförmigen Ladungsverteilung untersucht. Abgesehen von der lateralen Variation der Oberflächenladung unterscheidet sich dieser Fall gegenüber der homogen geladenen Wand im Hinblick auf eine verschwindende Nettoladung der Wand. Bei Betrachtung verschiedener Konfigurationen dieser Randbedingung konnte zunächst kein Übergang vom linearen in das nicht-lineare Regime der Fluidreaktion gefunden werden; für alle analysierten Amplituden der Wandladung blieb der Verlauf der Lösungsmitteldichten de facto konstant (siehe Abb. 4.5). Außerdem beeinflusste die Amplitude der Wandladung auch die Ionen nur in Form eines Proportionalitätsfaktors und erzeugte keine qualitativen Änderungen. Es liegt daher nahe, dass der Übergang zwischen den beiden Bereichen, lineare und nicht-lineare Fluidantwort, zumindest verschoben ist. Aufgrund der verschwindenden Nettoladung ist diese Änderung nicht überraschend. Allerdings zeigten sowohl die Ionendichten, in Form der lokalen Ladungsdichte, wie auch der Verlauf des elektrostatischen Potentials starke Variationen in Abhängigkeit der Wellenlänge der lateralen Variation der Oberflächenladung. Hierbei führten größere Wellenlängen zu deutlich gesteigerten Abklinglängen der Reaktion der entsprechenden Größen für zunehmende Distanz zur Wand (siehe Abb. 4.6 und 4.7). Als weiterer Schritt hin zu komplexeren heteroge-

nen Oberflächen wurde im letzten Abschn. 4.3.4 eine Auswahl an naheliegenden Oberflächenstrukturen analysiert, wobei die Ladungsstrukturen sowohl laterale Variation als auch eine effektive Wandladung, also eine nicht verschwindende gemittelte Wandladung, zeigten (siehe Abb. 4.8). Zunächst wurden diese Ladungsverteilungen im Hinblick auf die Auswirkungen auf die lokale Ladungsdichte, also die Teilchenzahldichten der Ionen, untersucht (siehe 4.9). Hier ergab sich, dass für Inhomogenitäten mit kurzer Periodenlänge die tatsächliche Form der Ladungsverteilung keine ausgezeichnete Rolle spielt, der einzig relevante Parameter in diesem Fall ist die gemittelte Ladungsstärke, also die Nettoladung der Wand. Des Weiteren wurde die Streifenstruktur (siehe Abb. 4.8 (b)) genauer untersucht, um den Einfluss der Wellenlänge der Oberflächenstruktur genauer zu analysieren. Wie auch schon in Kap. 3 und Abschn. 4.3.3 zu erkennen ist, zeigte sich auch hier erneut der starke Einfluss, den diese Wellenlänge auf die Struktur des Fluides besitzt. Längere Wellenlängen in der Ladungsverteilung führten auch hier zu einem Abklingen der Reaktionen des Fluides für zunehmende Entfernung zum Substrat auf deutlich gesteigerten Längenskalen (siehe Abb. 4.10). Jedoch konnte dieser Effekt, obgleich das zugrundeliegende Model zur Beschreibung der Elektrolytlösung deutlich komplexer war, selbst mit den einfachen Mitteln des in Kap. 3 verwendeten Ansatzes und den daraus folgenden analytischen Ausdrücken hervorragend beschrieben werden, wie in Abb. 4.10 klar zu sehen ist. Hier konnte nicht nur das asymptotische Verhalten für große Entfernungen zur Wand, für welches die mikroskopischen Details erwartungsgemäß an Bedeutung verlieren, sondern auch der Verlauf bspw. des elektrostatischen Potentials in direktem Kontakt zum Substrat mit bemerkenswerter Präzision reproduziert werden. Sogar die Betrachtung lediglich des Beitrages der zwei höchsten Ordnungen in der Entfernung zur Wand zeigte hier schon eine überraschende Übereinstimmung (siehe Abb. 4.11).

Zusammenfassend lässt sich sagen, dass die hier vorgestellte Forschung und ihre Ergebnisse klar die Bedeutung heterogener Oberflächenladungsverteilungen herausstellt. Insbesondere wurde gezeigt, wie wichtig die Berücksichtigung eventueller Inhomogenitäten und deren Auswirkungen auf angrenzende Elektrolytlösungen bei der Untersuchung der Struktur und des Verhaltens solcher Fluide an Oberflächen ist. Die hier untersuchten Modelle stellen dabei ein vielseitiges Fundament für weitere Forschungsarbeiten in diesem Bereich dar. Mögliche Schwerpunkte solcher Arbeiten könnten beispielsweise der Einfluss mehrerer Substrate und die durch das Fluid vermittelten Kräfte oder die Nutzung verschiedener Längenskalen zu Synthese von strukturierten Makromolekülen sein.

Abstract

Understanding the structure of fluids close to solid substrates is of great importance in numerous research applications. When studying these interfaces, a typical assumption is to regard the substrate as homogeneous with respect to wall-fluid interactions. For uncharged walls and fluids comprised of only neutral constituents, this assumption is reasonable. In contrast, in the case of electrolyte solutions in contact with charged walls, the effect of heterogeneities in the interactions is particularly long ranged, because the corresponding relevant length scale is set by the Debye length. This length is large compared to a molecular size scale, and such simplifications are therefore generally unsound. For this reason, in the present thesis the interactions of a planar wall with heterogeneous chemical and electrostatic properties with a nearby electrolyte solution were studied. The research focused on the influence of the interfacial inhomogeneities on the number densities of the fluid constituents. Because it has been proven to be a powerful tool for studies of fluid structure in terms of number density profiles, the analysis was performed within the framework of classical density functional theory. The basic mathematical framework of this theory is provided in Chap. 2. Based on this method, two different approaches were pursued, varying in complexity of the underlying model used to describe the electrolyte solution. The results of these investigations are presented in Chaps. 3 and 4, with the simpler approach of Chap. 3 providing first, basic insights, which were then verified and more extensively studied with the second approach as described in Chap. 4. The results presented in these chapters have mostly been published in Refs. [6, 7].

In Chap. 3, a chemically or electrostatically heterogeneous substrate adjacent to an electrolyte solution is studied. To describe the fluid and its components, a Cahn-Hilliard-like square gradient approximation was used (see Sec. 3.2.2). Moreover, while the model allowed for an arbitrary spatial distribution of nonuniformities of the chemical and electrostatic wall-fluid interactions, their influence was assumed to be sufficiently weak such that a linear response of the number density deviations from the bulk values was deemed justified. Consequently, closed-form analytical expressions could be derived (see Sec. 3.2.3), which were used to obtain basic, elemental insights into ion-solvent

coupling and the effects of chemically or electrically nonuniform walls. The study of single, isolated, δ-like interaction sites revealed significant differences in the reaction of the fluid for chemically as compared to electrostatically interacting walls. For chemical interactions between the substrate and the fluid, the resulting deviations from the bulk densities all decayed on the length scale of the bulk correlation length ξ, with deviations of the three different constituents being proportional to each other (see Figs. 3.2, 3.3, and 3.4). On the other hand, in the case of electrostatic interactions between the wall and the fluid, the solvent density remained unchanged and the density deviations of the two ion types were opposite in direction. An increase in counterion density was accompanied by a decrease in the density of coions. Additionally, the decay length significantly increased for charged walls, with the length scale being the Debye length $1/\kappa$ instead of the bulk correlation length $\xi \ll \kappa^{-1}$ (see Fig. 3.5). Introducing another length scale by increasing the area of interaction to nonvanishing size led to a discernible competition between length scales. If an internal length scale dominated the system, the resulting profiles showed strong similarities with the results for the δ-like interactions. However, upon increasing the external length scale set by the boundary condition, the structure of the surface charge pattern became increasingly relevant, with the density deviations of the fluid increasingly mimicking the structure imposed by the boundary condition (see Fig. 3.7). Lastly, a regular hexagonal lattice of Gaussian-shaped interaction sites, simulating a crystalline structure, was considered. Again, the analysis of the resulting profiles depended on the size and also the distance between separate interaction sites (see Fig. 3.8), influencing the importance of large lateral wave numbers $|\boldsymbol{q}_\parallel|$ on the structure of the fluid response. Considering the simplicity of this first approach, the number of observed effects was remarkable.

In Chap. 4, the insights gained from the first approach were used to refine the model describing the electrolyte solution and therefore produced more informative results. Instead of considering basic point-like particles, the framework of fundamental measure theory was introduced, in which the particles are modeled as hard spheres (see Sec. 4.2). Therefore, the nonelectrostatic interactions between the particles themselves and also between the particles and the wall are purely repulsive in this second model. In addition, the restriction to a linear response regime, as was used in the first approach, was lifted, making the approach taken in this chapter much more versatile. However, these expansions required to numerically determine the equilibrium number density profiles. First, the case of a homogeneously charged wall was explored. Confirming the results in Chap. 3, the observed density deviations all indicated an exponential decay away from the wall with a length scale given by the Debye length $1/\kappa$. Additionally, the resulting profiles exhibited the layer structure, which is known to occur for hard spheres next to hard walls

(see Figs. 4.2, 4.3). Expanding the findings from the first model, the number densities within this second approach revealed a qualitative change in the decay behavior for sufficiently high wall charges. For low surface charge strengths, the findings agreed with those of the simpler model from Chap. 3, exhibiting a linear response of the fluid particle densities. However, if the surface charge was increased, a second regime was revealed, in which the dissolved ions displaced solvent particles, marking the onset of nonlinear fluid response (see Figs. 4.2, 4.3, and 4.4). Introducing the simplest case of a lateral inhomogeneity with a single length scale, a sinusoidal charge distribution was analyzed in Sec. 4.3.3. Besides the lateral variation, this case also differed from the previous one because there was no overall charge on the surface. For this boundary condition, first and foremost, there was no qualitative change in the profile of the solvent and solute densities found. For all examined settings of the surface charge, the profiles of the solvent densities remained de facto unchanged (see Fig. 4.5). In addition, the amplitude of the surface charge only influenced the local charge density and the electrostatic potential in the form of a proportionality factor. Therefore, it appears that the transition of the linear response regime to the nonlinear fluid response is shifted towards higher amplitudes or wavelengths for the case of a sinusoidal surface charge distribution, which is likely a consequence of the vanishing net charge. However, both the solute densities expressed via the local charge density in the fluid and the electrostatic potential displayed strong dependence on the wavelength of the sinusoidal charge pattern. Increasing wavelengths greatly increased the decay length of the respective deviations from the profiles for the uncharged wall (see Figs. 4.6 and 4.7). In a final consideration, more complex surface charge structures were analyzed, wherein the structures combined both lateral variation in the surface charge and a nonvanishing net charge. First, various such structures (see Fig. 4.8) were compared, which revealed that, for small-scale variation, the only relevant parameter determining the response of the fluid was the average charge at the surface (see Fig. 4.9). Different average charges can therefore be used to more precisely resolve the transition regime from linear to nonlinear response, for example. Second, focusing on a striped surface charge pattern, a clear impact of the wavelength of the surface structure on the decay behavior of the electrostatic potential was found. Longer wavelengths not only increased the decay length of the potential away from the wall, but also the strength of the variation of the potential laterally along the wall (see Fig. 4.10). Although the model used in this second approach in Chap. 4 is much more elaborate compared to that of the first approach presented in Chap. 3, the influence of the lateral wavelength on the decay of the electrostatic potential was also detected with the simpler model used in Chap. 3, as is obvious in Fig. 4.10. Not only the asymptotic behavior far from the wall, but also the increase in the potential in close proximity to the wall was verified, with the

two highest orders of the analytical solution (see Sec. 3.2.3) already providing remarkably precise predictions (see Fig. 4.11).

The results of the research presented in this thesis clearly highlight the importance of accounting for possible heterogeneities in the surface charge structure of substrates when studying their impact on electrolyte solutions. The methods and models presented here provide a powerful framework for further studies in this research area. Possible starting points for further research could, for example, be the forces on neighboring walls mediated by a fluid as well as further refinements in the description of the properties of both the electrolyte solution and the charged substrate. Additionally, heterogeneities of different lateral length scales might be used for catalysing macroscopic particles by inducing laterally varying concentrations of fluid components to create, e.g, spatially varying surface chemistry on the particles.

Chapter 1

General introduction

Life without fluids, that is liquids and gases, is hardly imaginable. Not only are we constantly surrounded by a multitude of fluids, even we ourselves, as well as all other animals and plants are water-, and therefore fluid-based [8, 9]. Our modern understanding of a fluid is a substance, which is continuously deformed when being exposed to a shear stress [10], i.e. fluid is a state of matter which can resist only an isotropic pressure [8]. Studying fluids and understanding their properties plays a crucial role in many of our modern day technologies and applications [11], ranging from batteries and capacitors [1, 2] to biomembranes [3] and colloidal self-assembly [12], to photovoltaics and catalysts [4, 5], to name only a few. Due to their importance to our everyday life, it is no surprise, that research on fluids has a long history. I therefore want to start this doctoral thesis with a short overview over the history of fluid research and the development of the tools and methods used in this thesis.

One of the cornerstones of the modern theory of statistical mechanics was laid by Daniel Bernoulli in the early 18th century. He experimentally studied many types of fluid motion, and in his fundamental work *Hydrodynamica* he introduced the kinetic theory of gases, which was one of the first theories describing macroscopic properties of gases by their molecular motion [8, 13, 14]. Although it wasn't immediately accepted, the significance of this concept for the development of modern microscopic theories of fluids is beyond doubt. In the further course of the 18th century, there were several crucial contributions to the description of fluids associated with famous scientists like Euler, d' Alembert and Lagrange [8, 10, 13]. Not only did they introduce the basic mathematical framework of fluid mechanics and dynamics by establishing the differential calculus [8, 10, 13], but they also used these concepts to formulate basic equations of fluid motion, velocity and acceleration [10], thereby adding fundamental knowledge to the understanding of fluid behavior. This insight also laid the foundation for the famous Navier-Stokes equation

describing the motion of viscous fluids, which was derived independently by Claude Louis Marie Henri Navier [15] and George Gabriel Stokes [16] in the first half of the 19th century [8].

At that time the developments in fluid mechanics saw the emergence of a novel branch of physics, namely thermodynamics, which is what I want to focus on in this historic review, although scientific progress in fluid mechanics and dynamics did not stop there. In the beginning thermodynamics was nothing but a collection of loosely connected studies mostly about gases, which described a plethora of phenomena, linking macroscopic parameters, such as e.g. pressure p, temperature T and volume V in a mostly phenomenological way [17–19]. For example, the concept of specific heat capacity has been developed around 1750, Joseph Louis Gay-Lussac developed his well-known law linking pressure and temperature of a given mass of gas in 1808, and John Dalton published his lecture series *Experimental Essays* about the nature of mixed gases, describing among other things the expansion and contraction of gases at various temperatures, in 1802 [13, 20]. Also, first insights in the relationship between heat and energy emerged from the experiments of Lord Rumford in 1798 [19]. These studies were often motivated by observations made on guns or steam engines [17]. Over the course of the 19th century, a more axiomatic approach to thermodynamics has been developed [17]. One of these axioms was built on the research of the French physicist Nicolas Carnot, who originally published his famous reflections on the working mechanism of steam engines in 1824 [21], and who is often considered to be the founding father of thermodynamics [22]. His work initially received only little attention from other scientists. He died very young, and only when Lord Kelvin established his temperature scale inspired by Carnot's work and Rudolf Clausius explicitly mentioned Carnot almost 25 years later, his work received broader attention and acknowledgement. These two gentlemen, Lord Kelvin and Clausius, independently of each other refined Carnot's work and developed, in the early 1850s, what is now known as the second law of thermodynamics, describing conditions and limitations to the possibility of thermodynamic processes [17–19, 22–24]. It was also Clausius, who coined the term entropy in his studies on the kinetic theory of gases [22], which nowadays is universally used to express the second law of thermodynamics. Another axiom of thermodynamics was developed around the same time mainly by Julius Rudolf Mayer and James Joule [17–19, 22]. Mayer was first to theoretically derive the concept of conservation of energy by claiming the interchangeability of heat and work; Joule provided support for this concept by measuring the mechanical equivalent of heat, and connecting the amount of heat put into and the amount of work extracted from a cyclical process. Later Hermann von Helmholtz recognized the universal applicability of Mayer's statement and expanded it [17, 18, 22, 25]. This was essentially what is known today as the first law of thermo-

dynamics. The third fundamental law was established only years later at the beginning of the 20th century by Nernst [17, 22]. Together these three laws build the foundation of all thermodynamic considerations.

With the advances in the more phenomenological thermodynamics, the second half of the 19th century also saw an increasing interest in a microscopic description of thermodynamic processes and attempts to derive the fundamental assumptions of thermodynamics via a microscopic treatment [17–19, 26]. In a way, the continuum mechanical approach which had been developed by Euler and others and which eventually led to the thermodynamic theory stood in contrast to the atomistic approach via Newtonian mechanics [17]. For example, this atomistic approach was embodied by the kinetic theory of gases Bernoulli introduced in 1738 (see above [22]). In the late 1850s James Clerk Maxwell entered the scene, and after reading works of Clausius on Bernoulli's theory he recognized, that various properties of dilute gases in thermal equilibrium can be derived with Newtonian mechanics and some statistics [17, 27]. With his description of the distribution of molecular velocities he derived the first statistical law in physics, and thus founded the theory of statistical mechanics [17–19, 22, 26]. With this velocity distribution he could derive both the caloric and the thermal equations of state of ideal gases [18]. Several years later and inspired by Maxwell's work Ludwig Boltzmann started his extensive work on this theory, in which he revisited Maxwell's ideas and started to properly introduce statistical mechanics [18, 19, 22, 26]. In his work, much of which was published collectively in 1896 [22], he introduced his famous equation on the dynamics of ideal gases [17–19, 22] and tried to derive the second law of thermodynamics with this (H-theorem) [17] — to name only a couple of his research accomplishments. With his lifelong devotion to this field he is one of the most important figures in establishing statistical mechanics [17, 26, 28]. The second invaluably important contributor to statistical mechanics was Josiah Willard Gibbs. He coined the term statistical mechanics in 1884 [29], and with his fundamental research, published in 1902 [26], he finalized the theory as a general approach to unite atomistic statistical mechanics with thermodynamics, establishing methods to study properties of all mechanical systems, both macroscopic and microscopic [17–19, 22, 26]. In the 1920s further additions to the microscopic description of many-particle systems were provided by the newly developed quantum mechanics [17–19], but Gibbs' groundwork is still the key ingredient of statistical mechanics up to this day. So far, most studies considered fluids as more or less homogeneous materials. For example, not much attention was paid to the omnipresent boundaries and surfaces of a fluid. As part of Gibbs' work on the second law of thermodynamics and its validity, he also, as one of the first, considered heterogeneous systems, when he assumed the possible coexistence of two bulk phases [30]. In his derivations, however, the phases were merely separated

by two-dimensional mathematical entities, although he did acknowledge the occurrence of density heterogeneities near the interfaces [28, 31]. Although this treatment of an interface coincides with our everyday experience, where macroscopically large volumes of material are separated from each other by negligibly small borders, the microscopic situation couldn't be more different. However, the first microscopic treatment of a liquid-vapour interface was not introduced until 1894 by Johannes Diderik van der Waals, whose result reproduced a study from Lord Rayleigh, although he used a completely different approach [32, 33]. He found, that the interface is by no means a sharp entity, but it has a finite size and its structure is not straightforward. Later Smoluchowski also found interfaces to not be sharp and uniform, as spontaneous densification and rarefaction can occur in fluids [34]. With this very simple approach by van der Waals, in which he introduced variational techniques into thermodynamics, he in essence performed the very first study using what later became known as *density functional theory* (DFT) [28, 35, 36]. It is this technique, which is the key ingredient to the research presented in this thesis. Therefore, I want to highlight the development of density functional theory in the following.

With the discovery and advancement of quantum mechanics in the early 20th century, many models and equations were developed to describe quantum mechanical systems and their properties, the most famous of them being Schrödinger's equation, which Erwin Schrödinger postulated in 1926 [37]. Shortly after the publication of Schrödinger's theory, Llewellyn Thomas and Enrico Fermi developed their model, known as Thomas-Fermi model [38, 39]. In comparison to Schrödinger's theory, which is based on the wave function as the fundamental component, the Thomas-Fermi model is entirely based on the electron density. It was originally introduced to calculate the electron distribution moving in the potential of atoms, but it also proved to be useful for addressing many particle problems [40]. In particular, Thomas and Fermi showed that, using their model, the energy of the ground state can also be calculated via the electron density distribution [36, 38–40]. The variational principles introduced by van der Waals were extensively used in the following decades, e.g. by Cahn and Hilliard [28, 41]. The Thomas-Fermi model was also improved several times, e.g. by Dirac in 1930 [42] and Lewis in 1958 [43], to deliver more precise results.

However, the breakthrough in terms of the theoretical foundations came only in the early 1960s, when the Thomas-Fermi theory was revisited and refined by Pierre Hohenberg, Walter Kohn and Lu Jeu Sham in two landmark papers [44, 45]. In the first paper Hohenberg and Kohn showed, that the electron distribution of the ground state minimizes a unique functional of the electron density distribution. In the second paper Kohn and Sham postulated, that in a system of many particles this ground state energy can be divided into contributions from a noninteracting reference system, where all particles only

experience the potentials of the nuclei, a second contribution accounting for their Coulombic repulsion, and a third contribution arising from exchange and correlation effects [28, 46]. With this they laid the theoretical foundations for all later DFT studies. Because of the outstanding success of this technique and its potentially far-reaching applications, Kohn was awarded the Nobel Prize in Chemistry in 1998 [47]. Soon after, Mermin succeeded in expanding Hohenberg's and Kohn's studies to nonvanishing temperatures [48], using the grand potential instead of the free energy. In the meantime, that is in the first half of the 20th century until the early 60s, progress was made in the study and formalism of inhomogeneous fluids [46]. Montroll and Mayer [49], for example, provided the solution to problems formulated by Ursell [50] and Mayer [51] to derive formal expressions for thermodynamic properties of imperfect gases and condensing systems within the limits of low temperatures. In this spirit, Morita and Hiroike also derived expressions for density distributions in dependence of integral equations over the underlying potentials [52, 53]. In the 1950s, Percus derived thermodynamic properties in terms of correlation functions via variational methods applied to the free energy and also presented methods to derive these correlation functions [54, 55]. De Dominicis followed up on this shortly afterwards, deriving several thermodynamic functions expressed via one- and two-particle densities and a correlation matrix [56]; he also expressed the grand partition function as a stationary equation in terms of these particle densities. In the early 1970s Bongiorno and Davis [57, 58] as well as Toxvaerd [59, 60] also used perturbation approaches to revisit the planar liquid gas interface, where the focus was primarily on triple point studies [57].

Another major step forward in the development of DFT came in 1976, when Charles Ebner, William Saam and David Stroud recognized the link between the quantum mechanical theory of Kohn et al. and statistical mechanical problems in the context of classical fluids [28, 46, 61, 62]. One year later, Saam and Ebner even further expanded this theory, thereby establishing DFT for classical liquids, which is since then a widely and frequently used method in a whole range of different applications [36, 63]. Formally, the approach is exact. However, for most cases, the excess functional, being the part on top of the exactly calculable ideal gas part, and the interaction potentials are not exactly known, making the DFT treatment dependent on the quality of the approximations used. Thus, in the years since its development, many different approximations have been introduced [46, 64]. Let me close this review of the history of fluid mechanics and the development of the framework of density functional theory by presenting some of the most successful approximations, highlighting the ones used in this thesis.

A basic idea to facilitate the calculations is the independent study of subsystems by splitting of the interactions, which, especially in the case of ionic contributions, is a straightforward consideration [46]. Along these lines I want first to focus on the approxim-

ations typically used to model the nonelectrostatic interactions and turn to electrostatics later. The best-known approximation is probably the so-called *square-gradient approximation* (SGA) [46]. In first order, or for homogeneous fluids, it basically reproduces the approach of van der Waals from one hundred years ago, which is usually referred to as *local density approximation* (LDA). Although the square gradient approach is justified only for slowly varying densities, it still proves extremely valuable for a variety of problems [36, 46], which is why it is used as a starting point for the first part of this thesis (see Chap. 3). It will be obvious in Chap. 3, that its generalization to fluid mixtures is straightforward [46]. Other types of approximations can be regarded as expansions of the integral-equation theories used before the establishment of DFT. In these approximations, the Ornstein-Zernike-Equation, combining the pair distribution function, the pair correlation function and the direct correlation function (see Chap. 2), as well as another so-called *closure relation* is used [46]. These approximations are closely related to expansions of the excess functional around known reference densities and their corresponding grand potentials, referred to as *density or virial expansions* [46, 65].

In the 1980s, motivated by coarse graining treatments, another type of approximations was developed [46]. Maybe the first of these approaches was the one by Nordholm and collaborators [66, 67]. As heavily oscillating density profiles, which can occur, e.g., close to interfaces and surfaces, are not well suited for a treatment within the SGA, Nordholm et al. used a so-called *weighted density*, thereby introducing the family of weighted density approximations (WDA) [46]. In this family, weight functions are used to "average" the actual density distribution, which in turn are used to determine the excess functional. Approximations of this family mainly vary in the choice of the weights, with two of the most prominent representatives being the Tarazona Mark I [68] and the Tarazona Mark II [69] approaches [36, 46, 64]. The standard test of such approximations are hard spheres, since their excluded volume provides a natural order of magnitude for the weights, and the only relevant parameter in those systems is the particle density [36, 46, 64]. Again, these approaches can be readily expanded to describe mixtures. The aforementioned approximations all have in common, that they take a certain approximated correlation function as an input and derive the grand potential from it [36]. A different approach was taken by Yaakov Rosenfeld in 1989 [70], who was the first to use multiple weight functions and based all of them only on geometrical considerations [36, 46]. His model is nowadays known as *fundamental measure theory* (FMT), and it already included the treatment of fluid mixtures in the definition of the weights [46]. The form of the weights used in Rosenfeld's theory have been improved and refined by Rosenfeld himself [71] as well as by Kierlik and Rosinberg [72] in the subsequent years. This original FMT, being a significant improvement over other WDAs, was frequently and very successfully used in

the last decades [36, 46, 73] and has also been successfully adapted to many other scenarios such as soft interacting systems or polymers [36]. However, it has its shortcomings, e.g., in failing to describe a stable crystalline phase [46, 73]. To address this, Roland Roth, Robert Evans and coworkers introduced an improved approach of Rosenfeld's FMT [73], called the *White Bear version*, in acknowledgement of a Bristol pub, which "supported" the development of the theory (see references in [73]). The White Bear version significantly improved the original FMT by rewriting it for a different, more precise equation of state. Rosenfeld built his theory on top of the Percus-Yevick bulk equation of state, and Roth et al. used the empirical Mansoori-Carnahan-Starling-Leland (MCSL) equation of state [74], which is known to be more precise in the case of hard sphere mixtures [73]. Roth even developed a second version, White Bear II, in 2006 [75] to further improve the model by using the mixture extension of the Carnahan-Starling equation of state, keeping a similar level of complexity, but achieving a more consistent relation with scaled-particle theory [64]. Because this framework is ideally suited for tackling the questions studied in this thesis, I used this version of the DFT in Chap. 4, with the somewhat simpler approach of the original White Bear being sufficiently precise for the level of accuracy this research is aiming for. Rosenfeld's and later also Roth's methods inspired many more attempts to generalize and adapt their theories for the description of more and more complex systems, e.g., with attraction [76] or polymeric structure [77]. However, these theories are not relevant for the system studied in the present thesis, which is why I will not go into further detail here.

Aside from their microscopic structure, there are multiple possible classifications of fluids, one of them being the presence of charge carriers. There are fluids comprising only neutral constituents, and there is the exact opposite, fluids only consisting of charge carriers, so-called *ionic liquids*. Common examples for ionic liquids are molten salts; however, salts usually need extremely high temperatures to enter a liquid state, which poses new challenges for their description, but there are other ionic liquids at room temperature. The liquid state of these *room-temperature ionic liquids* is often caused by the nonspherical shape of their molecules or particles on an atomic length scale and a heterogeneous charge distribution inside these molecules [2, 78]. In between these two extremes there are also mixtures, i.e., fluids containing neutral solvent particles as well as charged ionic particles; these are commonly referred to as *electrolyte solutions*. As mentioned in the beginning, one of the most common and most important fluids is water, which intrinsically contains ionic molecules [79]. Furthermore, due to the high dielectric constant it is a good solvent and usually contains dissolved ions [79, 80]. It therefore clearly classifies as an electrolyte solution, making this type of conducting liquids an important field of study. If solids come into contact with such fluids, they tend to develop a charge on

their surface. This can occur, for example, via dissociation of ionic groups from surface molecules or via specific adsorption of ions to surface molecules. In addition, one can create surface charges by applying an external electric potential between the solid and a counterelectrode [79, 80]. In any case, these surface charges create an electrostatic field inside the fluid, which in turn attracts counterions to the surface. The resulting formation of charged layers is known as *electric double layer* (EDL) [31, 79, 81].

Studies of the structure of these layers date back as far as the 1870s, when Helmholtz studied the double layer at the interface between the wall of a vessel and a liquid [82]. His very simple model was based on the assumption, that the counterions bind directly to the surface, therefore forming a structure similar to the one found in plate capacitors. This model, nowadays known as Helmholtz-model, was capable of explaining some basic features of the electric double layer, but failed in, for example, describing the phenomenon of a voltage-dependent capacitance, which in Helmholtz's approach was simply dependent on the distance of the two layers [83, 84].

Based on the work of Boltzmann, Louis Gouy and David Chapman early in the 20th century revisited the problem of the structure of the EDL and included thermal motion of the ions into their approach. They concluded that the counterions form a diffuse layer, rather than a sharp one as postulated by Helmholtz [85–87]. In their theory, Gouy and Chapman combined the conditions of Siméon Denis Poisson and Boltzmann using the Poisson-Boltzmann equation (PB) to describe the charge as spatially extended, and successfully applied it to the case of a planar surface. Several years later, Peter Debye and Erich Hückel extended the Gouy-Chapman theory to spherical surfaces [79, 88]. Albeit being also a very simplistic approach, their theory, to this day, is successfully applied in describing monovalent ions, small ionic strengths and small surface charges. This longevity can be attributed to the successful experimental verification of the predicted differential capacitance [79].

In 1924 another improvement over the existing models was introduced. Otto Stern pointed out several limitations of the Gouy-Chapman approach, such as the possibility of large charge accumulations close to the charged surface [89]. He proposed combining the two previous models, such that the charge in the fluid is partly accumulated at a distance of about one ionic radius away from the surface, thereby forming a so-called *Helmholtz plane*. The surplus charge is then forming a diffuse layer as suggested by Gouy-Chapman [80].

This model of a closely adsorbed layer of charge combined with a diffuse layer at a larger distance from the wall was extended even further about thirty years later by Grahame. He improved and refined the concept of Stern layers by assuming the existence of multiple Helmholtz layers [84]. The innermost of them is formed by adsorbed ions

which are tightly bound to the surface either via covalent or van-der-Waals bonds. He argued, that these specifically adsorbed ions, due to their lack of a hydration shell, can approach the charged electrode even more closely than dissolved ions. This layer is called the inner Helmholtz plane. Next to this plane there is a layer formed by the hydrated and electrostatically attracted counterions, much like the original Helmholtz layer; it is nowadays referred to as outer Helmholtz plane [79]. Following these layers there is again the diffuse layer of spatially distributed charges satisfying the Poisson-Boltzmann equation.

In parallel with the models discussed above, an increasingly sophisticated understanding of the structure of the EDL was developed. It became progressively clear, that the nonvanishing size of the ions accounted for by the Helmholtz layers is important for the properties of electric double layers. Among other effects, studies have demonstrated that finite size effects of charges can lead to a nonmonotonous decay of the electrostatic potential [81, 90]. In its original form, however, the Poisson-Boltzmann theory, which is used to describe the diffuse layer in all the models above, considers the ions as point-like particles, i.e., all the theories above neglect the finite size of the ions for distances larger than a couple of particle radii. In the last decades, different, more precise, models were introduced. The first one is the *primitive model* (PM) which regards the ions as charged hard spheres, therefore adding a hard sphere repulsion on top of the PB theory [65]. The solvent is still treated only as a background, implicitly entering the equations solely via the permittivity. Extending the model to additionally describe the solvent particles as uncharged hard spheres leads to a model called *solvent primitive model* or *molecular solvent model*. An even more detailed description of the solvent molecules is achieved within the *civilized model*, in which an embedded electric dipole is also considered. For all these models, there is also a so-called *restricted* version, in which all the hard sphere radii are considered to be equal.

To study systems within the previously described models, there are various tools available. On the one hand there are simulation methods, such as Monte Carlo simulations or molecular dynamics simulations, which have, for example, been used to survey bulk structure [91–93] and structure within an EDL [94–97]. On the other hand, there are also theoretical approaches such as adapted Poisson-Boltzmann equations [98, 99] called modified Poisson-Boltzmann theories [100, 101]; Bhuiyan and Outhwaite proposed a number of such approaches [102–104]. Furthermore, the already discussed integral equation methods using the Ornstein-Zernike equation have been used to investigate the properties of EDLs, e.g., within the *hypernetted chain equations* (HNC) or the *mean spherical approximation* (MSA) [80, 105, 106]. A third method to investigate the molecular models mentioned above is via the DFT, which is what was used in this thesis.

To sum up, the study of fluids in heterogeneous systems offers a variety of interesting areas of research to explore. Additionally, the fact, that charges are ubiquitous in real fluids, provides even more complexity and even richer phenomena to investigate. Numerous previous studies performed in this field, however, are subjected to certain restrictions or simplifications. Among other simplifications, a commonly made approximation is modeling the interaction between a surface and a fluid as laterally homogeneous. The reason for this approximation is the significant simplification of the calculations as well as a lack of actual experimental data concerning the local structure of the surface. In the absence of electrically charged components this simplification is well-grounded, since the length scale on which the influence of surface heterogeneities decays is set by the bulk correlation length, if one neglects wetting transitions [107]. Far away from critical points this bulk correlation length is of the order of a few molecular diameters, with the result that heterogeneities are of negligible importance. However, in the case of electrically charged components, e.g., surfaces and fluid particles, the scale of the decay of the relevant (charge-charge) correlation function is given by the Debye length. Especially in the case of electrolyte solutions, this length scale is typically much larger than any fluid components. On top of that, distances between surface charge heterogeneities are typically also of the order of the Debye length, which argues strongly against the simplification of homogeneous interaction distributions mentioned above [108–110]. Fittingly, heterogeneous surface charge distributions are under suspicion to cause a number of "anomalies" in the context of colloidal forces (see, e.g., [111, 112]). In Ref. [113], for example, a change in the sign of the interaction between two surfaces across an aqueous solution was found, crossing over from repulsive to attractive interactions, when changing the surface charge distribution towards random heterogeneities or when increasing the separation of the surfaces [114]. Furthermore, studies have found the assembly of heterogeneously charged colloids close to a patterned substrate to be sensitive to the shape of the surface charge pattern [115]. Further frequently used simplifications are, e.g., the analysis of only net-neutral surfaces [116, 117] or the neglect of the solvent particles, accounting for the solvent only implicitly via the permittivity. However, known coupling effects due to the competition between solvation and electrostatic interactions cannot be captured by such approaches [118–120]. The plethora of expected phenomena sketched above, combined with the lack of more precise theoretical treatments motivated me to study the structure of EDLs adjacent to heterogeneously charged substrates (see Chaps. 3 and 4). The use of density functional theory to investigate such systems was motivated on the one hand by the relatively fast convergence of numeric DFT implementations, allowing the study of a multitude of parameters and even a fully three-dimensional system, and on the other hand by the significant success of previous research in describing electrolyte solutions and

hard spheres.

The following chapters describe the research performed and the knowledge gained in the course of my doctoral studies. Chaps. 3 and 4 discuss different approaches and different levels of precision in describing the features of an electrolyte solution in contact with a nonuniformly charged substrate, with each chapter including a theoretical background section and a description of the results. Additionally, each chapter has a separate thematic introduction and short summary.

Preceding these chapters, Chap. 2 presents the density functional theoretical framework the research is based on. A short introduction of the fundamental DFT terminology alongside a mathematical derivation of the essential equations and approximations necessary for an understanding of this thesis are provided.

In Chap. 3, a first approach to the study of the structure of an electrolyte solution next to a heterogeneously charged substrate is presented. In this first analysis, the solvent particles are explicitly taken into account. However, all finite size effects are neglected. Focusing on length scales larger than the size of typical fluid particles and weak interaction strengths, a Cahn-Hilliard-like SGA is used. This simplistic approach allows for the calculation of closed-form analytical expressions describing chemically or electrically nonuniform substrates. Various examples of such surfaces are then explored in terms of particle number density profiles in lateral and normal direction with respect to the substrate.

Building upon Chap. 3, Chap. 4 expands the first approach to include finite size effects. Again, all three particle types, two types of solute ions and the solvent particles, are taken explicitly into account, which qualifies the model as a *molecular solvent model*. Albeit not required in terms of the implementation, this chapter restricts itself to the treatment of equal particle sizes. This makes the model used here a *restricted molecular solvent model*. To account for the finite size of the particles studied, the DFT is expanded via the FMT method of Roth et al. [73]. Again, the resulting framework is used to investigate a number of surface charge distributions in terms of particle number density profiles, charge density and the structure of the electrostatic potential. The results are also used to test the validity of the somewhat simpler model used in Chap. 3.

Conclusions and summary of the research presented in the dissertation are provided in Chap. 5. In a preview, future research to be built on this thesis is proposed.

Chapter 2

Principles of density functional theory

The basic result, on which DFT is based on, is the fact, that for a given interatomic, or -molecular, potential, there exists a unique functional, the free energy, which is minimized by the equilibrium density distribution in the system [46, 65]. Given this minimum, all relevant thermodynamic functions can be calculated from that [57]. It has proven to be a powerful tool, since the theory is able to describe both the macroscopic properties and the microscopic structure of a fluid solely using intermolecular forces as input [28]. In the following I want to introduce and establish the formulations and equations of the density functional theory, which form the basis of the research presented in the thesis at hand. The derivation is similar to the ones in [46, 57, 121]. As is so often the case in theoretical physics, let us first consider the Hamiltonian of a fluid of N atoms, each with mass m,

$$\begin{aligned} H_N &= \sum_{i=1}^{N} \frac{\boldsymbol{p}_i^2}{2m} &+ \Phi(\boldsymbol{r}_1, ..., \boldsymbol{r}_N) &+ \sum_{i=1}^{N} V(\boldsymbol{r}_i) \\ &= k.e. &+ \Phi &+ V, \end{aligned} \tag{2.1}$$

where $\boldsymbol{p}_i$ is the momentum of particle i, Φ is the interatomic potential and V is the one-body external potential. The external potential will be given by the system under consideration. Based on these foundations it follows, that the system is best described within the grand canonical ensemble. In this ensemble the ensemble average of any quantity $A(\{\boldsymbol{r}_i\}, \{\boldsymbol{p}_i\})$ can be expressed as

$$\langle A \rangle = \mathrm{Tr}[f_0 A], \tag{2.2}$$

with the classical trace Tr used here together with f_0, the equilibrium probability density. It is defined by

$$f_0 = \frac{1}{\Xi} \exp(-\beta(H_N - \mu N)), \tag{2.3}$$

where $\beta = (k_\mathrm{B}T)^{-1}$, with the Boltzmann constant k_B and the temperature T, μ being the chemical potential, and the normalization factor Ξ being the so-called *grand partition function*

$$\Xi = \mathrm{Tr}[\exp(-\beta(H_N - \mu N))]. \tag{2.4}$$

Probably the most important example of such an ensemble average is the one-body density

$$\varrho(\boldsymbol{r}) = \langle \widehat{\varrho}(\boldsymbol{r}) \rangle, \tag{2.5}$$

with $\widehat{\varrho}(\boldsymbol{r}) = \sum_{i=1}^{N} \delta(\boldsymbol{r} - \boldsymbol{r}_i)$ being the so-called one-body density observable. The grand potential

$$\Omega = -k_\mathrm{B}T \ln \Xi \tag{2.6}$$

is therefore a functional of V and with this also a functional of the combination

$$u(\boldsymbol{r}) \equiv \mu - V(\boldsymbol{r}). \tag{2.7}$$

With this, a sequence of correlation functions can be established by functional derivatives of Ω with respect to $u(\boldsymbol{r})$, where it is straightforward to show that the first derivate is equivalent to the one body density profile,

$$\varrho(\boldsymbol{r}) = -\frac{\partial \Omega}{\partial u(\boldsymbol{r})}. \tag{2.8}$$

Another frequently used function is the density-density correlation function

$$\begin{aligned} \mathcal{G}(\boldsymbol{r}_1, \boldsymbol{r}_2) &\equiv \langle (\widehat{\varrho}(\boldsymbol{r}_1) - \langle \widehat{\varrho}(\boldsymbol{r}_1) \rangle)(\widehat{\varrho}(\boldsymbol{r}_2) - \langle \widehat{\varrho}(\boldsymbol{r}_2) \rangle) \rangle \\ &= -\beta^{-1} \frac{\partial^2 \Omega}{\partial u(\boldsymbol{r}_2)\, \partial u(\boldsymbol{r}_1)} \\ &= \beta^{-1} \frac{\partial \varrho(\boldsymbol{r}_1)}{\partial u(\boldsymbol{r}_2)}, \end{aligned} \tag{2.9}$$

which can obviously be calculated using the second derivative of Ω with respect to $u(\boldsymbol{r})$. This density-density correlation function is in turn closely related to the two-body distribution function

$$\varrho^{(2)}(\boldsymbol{r}_1, \boldsymbol{r}_2) = \mathcal{G}(\boldsymbol{r}_1, \boldsymbol{r}_2) + \varrho(\boldsymbol{r}_1)\varrho(\boldsymbol{r}_2) - \varrho(\boldsymbol{r}_1)\delta(\boldsymbol{r}_1 - \boldsymbol{r}_2). \tag{2.10}$$

Continuing this scheme, further derivatives of Ω lead to the three-body, four-body etc. correlation functions. Another sequence of correlation functions is generated via the differentiation with respect to the one-body density $\varrho(\boldsymbol{r})$ instead of $u(\boldsymbol{r})$. Despite $\varrho(\boldsymbol{r})$ clearly being a functional of $u(\boldsymbol{r})$, one can show that for fixed Φ, T and μ (see Eq. (2.1)), only one specific external potential $V(\boldsymbol{r})$ can determine a unique equilibrium one-body density $\varrho(\boldsymbol{r})$ [48, 57]. With this follows that the probability density f_0 is uniquely determined by $\varrho(\boldsymbol{r})$ and therefore also the functional

$$\mathcal{F}[\varrho] = \mathrm{Tr}[f_0(k.e. + \Phi + \beta^{-1} \ln f_0)] \tag{2.11}$$

is a unique functional of the density. Legendre transforming $\mathcal{F}$ leads to the functional

$$\Omega_V[\tilde{\varrho}] = \mathcal{F}[\tilde{\varrho}] - \int \mathrm{d}\boldsymbol{r} \;\; u(\boldsymbol{r})\tilde{\varrho}(\boldsymbol{r}). \tag{2.12}$$

This functional reduces to the grand potential Ω (see Eq. (2.6)) for the equilibrium density $\tilde{\varrho} = \varrho$ [57, 121]. Additionally, it can be shown that the grand potential Ω is equal to the minimum value of the functional $\Omega_V[\tilde{\varrho}]$ [57]. This means that $\Omega_V[\tilde{\varrho}]$ together with ϱ provide a variational principle

$$\left.\frac{\partial \Omega_V[\tilde{\varrho}]}{\partial \tilde{\varrho}}\right|_{\varrho} = 0, \qquad \Omega_V[\varrho] = \Omega, \tag{2.13}$$

for calculating the equilibrium density of a fluid in a given external potential V. This variational principle combined with Eq. (2.12) forms the starting point of *density functional theory* (DFT). The main task in applications of this theory is deriving an appropriate expression for $\mathcal{F}$. Since the total Helmholtz free energy is

$$\begin{aligned} F &= \Omega + \mu \int \mathrm{d}\boldsymbol{r} \;\; \varrho(\boldsymbol{r}) \\ &= \mathcal{F}[\varrho] + \int \mathrm{d}\boldsymbol{r} \;\; \varrho(\boldsymbol{r}) V(\boldsymbol{r}), \end{aligned} \tag{2.14}$$

$\mathcal{F}$ is often referred to as *intrinsic Helmholtz free energy*. This functional contains both an ideal gas contribution, that is a noninteraction contribution

$$\beta \mathcal{F}_{\mathrm{id}}[\varrho] = \int \mathrm{d}\boldsymbol{r} \;\; \varrho(\boldsymbol{r})[\ln(\Lambda^3 \varrho(\boldsymbol{r})) - 1], \tag{2.15}$$

and contributions stemming from atom-atom forces in the fluid. This excess contribution $\mathcal{F}_{\mathrm{ex}} = \mathcal{F} - \mathcal{F}_{\mathrm{id}}$ can again be used to create a hierarchy of *direct correlation functions*

$$c^{(1)}(\boldsymbol{r}) = -\frac{\beta \mathcal{F}_{\mathrm{ex}}[\varrho]}{\partial \varrho(\boldsymbol{r})}, \tag{2.16}$$

$$\begin{aligned} c^{(2)}(\boldsymbol{r}_1, \boldsymbol{r}_2) &= \frac{c^{(1)}(\boldsymbol{r}_1)}{\partial \varrho(\boldsymbol{r}_2)} \\ &= -\frac{\partial^2 (\beta \mathcal{F}_{\mathrm{ex}}[\varrho])}{\partial \varrho(\boldsymbol{r}_1)\, \partial \varrho(\boldsymbol{r}_2)}, \end{aligned} \tag{2.17}$$

and so on. The two particle direct correlation function $c^{(2)}(\boldsymbol{r}_1, \boldsymbol{r}_2)$ can also be expressed via

$$c^{(2)}(\boldsymbol{r}_1, \boldsymbol{r}_2) = \frac{\delta(\boldsymbol{r}_1 - \boldsymbol{r}_2)}{\varrho(\boldsymbol{r}_1)} - \beta \frac{\partial u(\boldsymbol{r}_1)}{\partial \varrho(\boldsymbol{r}_2)}, \tag{2.18}$$

which shows that $c^{(2)}$ is, in principle, the inverse of the density-density correlation function $\mathcal{G}$. Combining Eqs. (2.9) and (2.18), one finds the integral equation

$$h(\boldsymbol{r}_1, \boldsymbol{r}_2) = c^{(2)}(\boldsymbol{r}_1, \boldsymbol{r}_2) + \int \mathrm{d}\boldsymbol{r}_3 \;\; h(\boldsymbol{r}_1, \boldsymbol{r}_3) \varrho(\boldsymbol{r}_3) c^{(2)}(\boldsymbol{r}_2, \boldsymbol{r}_3), \tag{2.19}$$

which combines the two-body correlation function $c^{(2)}$ and the *total* correlation function h, which is defined as

$$\varrho(\boldsymbol{r}_1)\varrho(\boldsymbol{r}_2) h(\boldsymbol{r}_1, \boldsymbol{r}_2) \equiv \varrho^{(2)}(\boldsymbol{r}_1, \boldsymbol{r}_2) - \varrho(\boldsymbol{r}_1)\varrho(\boldsymbol{r}_2). \tag{2.20}$$

Eq. (2.19) is the *Ornstein-Zernike equation*. The above equations together form the mathematical foundation of the so-called *density functional theory*, which is the main ingredient to the calculations done in the context of this study. For ideal gases, the density profile $\varrho(\boldsymbol{r})$ can exactly be determined to reproduce the well-known barometric law for any external potential V. However, there is no other case, for which $\mathcal{F}[\varrho]$ is known exactly in three dimensions [46]. The above theory is therefore always used by making approximations about the exact form of the excess functional $\mathcal{F}_{\mathrm{ex}}$. The problem formulation in this theory is then to find suitable approximations either directly for $\mathcal{F}_{\mathrm{ex}}$ and thus for Ω_V (see Eq. (2.12)) or via further differentiation of the excess functional and usage of the two particle direct correlation function $c^{(2)}$ and the Ornstein-Zernike equation (2.19) with subsequent inversion to calculate h [121]. These approximations have to be on the one hand sufficiently accurate for a possibly wide range of systems, i.e., external potentials $V(\boldsymbol{r})$, and on the other hand computationally manageable [46, 65]. In the past decades a multitude of approximations has been proposed for usage in a variety

of different applications. In the research presented here and discussed in the following Chaps. 3 and 4 the first method was used, that is direct approximations for $\mathcal{F}_{\mathrm{ex}}$ have been made, which are separately discussed in the introductory sections of the respective chapters.

Chapter 3

Analytically solvable square-gradient approach

The following Chap. 3, apart from subtle modifications, corresponds to the study published in Ref. [6]. Therein, a first step towards studying the influence of a heterogeneous distribution of chemical or electrical interaction sites at a flat substrate onto the number density profiles of a nearby fluid is taken. Here all three particle types — the solvent and both types of dissolved ions — are taken into account explicitly. However, a very simple way of describing the fluid is chosen, mainly describing the fluid components as point-like particles. This approach allows for the derivation of closed-form analytic expressions describing the influence of nonuniform walls, which can be used as basis for further studies, as performed in Chap. 4. Here, the analysis of isolated δ-like interactions, isolated interaction patches, and hexagonal periodic distributions of interactions sites reveals a sensitive dependence of the fluid density profiles on the type of the interaction, as well as on the size and lateral structure and distribution of interaction sites.

3.1 Introduction

Detailed knowledge of the structure of electrolyte solutions close to solid substrates is of great importance to numerous research areas and fields of application, ranging from electrochemistry [122, 123] and wetting phenomena [124, 125] via coating [126] and surface patterning [5, 127] to colloid science [128, 129] and microfluidics [130, 131]. The vast majority of models describing fluids in contact with substrates consider the latter as uniform with respect to the wall-fluid interaction. This approximation is commonly made partly due to a lack of experimental data on the actual local properties of the substrate under consideration and partly for the sake of simplicity. For fluids comprising

only *electrically neutral* constituents and *uncharged* walls, assuming uniform substrates is typically an acceptable approximation because, in the absence of wetting transitions, heterogeneous substrate properties influence the fluid only on length scales of the order of the bulk correlation length [107], which, not too close to critical points, is of the order of a few molecular diameters. In contrast, nonuniformities of the *surface charge* density of charged substrates in contact with dilute electrolyte solutions influence the fluid on the scale of the Debye length, which is much larger than the size of the molecules. Furthermore, the charged sites of substrates, such as mineral surfaces and polyelectrolytes, are lateral distances apart which are typically comparable with the Debye length of the surrounding fluid medium [108–110]. Hence, the assumption, that substrates in contact with electrolyte solutions carry a uniform surface charge density, is, in general, untenable.

In recent years considerable theoretical interest has emerged in the effective interaction between two heterogeneously charged walls (which typically are the surfaces of colloidal particles) mediated by an electrolyte solution [111, 113, 114, 116, 117, 132–137]. In contrast to uniform substrates, this effective interaction can lead to lateral forces, in addition to the common ones in normal direction. However, all the studies cited above model the solvent of the electrolyte solution as a structureless dielectric continuum. This approach precludes coupling effects due to a competition between the solvation and the electrostatic interaction, which are known to occur in bulk electrolyte solutions [118–120]. In particular, in the presence of ion-solvent coupling and far away from critical points, correlations of the solvent number densities in a dilute electrolyte solution decay asymptotically on the scale of the Debye length. Consequently, under such conditions, nonuniformities of the nonelectrostatic solvent-wall interaction can influence the structure of an electrolyte solution close to a wall and hence the strength and range of the effective interaction between two parallel plates immersed in an electrolyte medium on a length scale much larger than the molecular size. This mechanism differs from the one studied in Refs. [111, 116, 117, 132], in which the walls are locally charged but overall charge neutral.

In the present analysis a first step is taken towards a description of the structure of electrolyte solutions close to chemically and electrically nonuniform walls in terms of all fluid components. The natural framework for obtaining the fluid structure in terms of number density profiles of solvent and ion species is classical density functional theory [46, 57, 121]. Here, the simplest case of an electrolyte solution, composed of a single solvent species and a single univalent salt component, is considered far away from bulk or wetting phase transitions. Moreover, the spatial distribution of nonuniformities of the chemical and electrostatic wall-fluid interactions can be arbitrary but their strengths are assumed to be sufficiently weak such that a linear response of the number density deviations from

the bulk values is justified. This setup allows for closed-form analytic expressions which are used to obtain a first overview of the influence of ion-solvent coupling on the structure of electrolyte solutions in contact with chemically or electrically nonuniform walls. This insight will guide future investigations of more general setups within more sophisticated models, as performed in Chap. 4.

After introducing the formalism in Sec. 3.2, selected cases of heterogeneous walls are discussed in Sec. 3.3. Due to the linear relationship between the wall nonuniformities and the corresponding number density deviations from the bulk values, the latter are given by linear combinations of elementary response features, which are discussed first. Next, two main cases are studied: wall heterogeneities, which are laterally isotropic around a certain center and wall heterogeneities, which possess the symmetry of a two-dimensional lattice; the study of randomly distributed nonuniformities [111, 114, 132–134] is left to future research. For both cases various length scale regimes are discussed, which are provided by the bulk correlation length of the pure solvent, the Debye length, and a characteristic length scale associated with the wall nonuniformities. Conclusions and a summary for this chapter are given in Sec. 3.4.

3.2 Theoretical foundations

3.2.1 Setup

Here, the influence of a chemically and electrically nonuniform wall on the fluid density is studied. In spatial dimension $d = 3$ the system consists of an impenetrable planar wall for $z < 0$ and a fluid for $z > 0$, both parts being macroscopically large. In the following, the space occupied by the fluid is denoted by $\mathcal{V} := \{\boldsymbol{r} = (x, y, z) \in \mathcal{A} \times \mathcal{L}\}$; the positions $\boldsymbol{r} = (x, y, z) = (\boldsymbol{r}_\parallel, z)$ are uniquely decomposed into the lateral components $\boldsymbol{r}_\parallel = (x, y) \in \mathcal{A} \subset \mathbb{R}^2$ and the normal component $z \in \mathcal{L} = [0, L]$ relative to the wall surface at $z = 0$. The size $|\mathcal{A}|$ of the wall and the extent L of the system in normal direction are both assumed to be macroscopically large. The fluid is an electrolyte solution composed of an uncharged solvent (index “1”), univalent cations (index “2”), and univalent anions (index “3”). Two types of interactions between the fluid and the wall are considered: (i) electric monopoles at the wall surface ($z = 0$) and the fluid ions, giving rise to an electrostatic interaction, (ii) all other contributions, in particular those due to nearest-neighbor-like chemical bonds, referred to as nonelectrostatic interactions.

3.2.2 Density functional theory

In this study, I use density functional theory [46, 57, 121] in order to determine the equilibrium number density profiles $\boldsymbol{\varrho} = (\varrho_1, \varrho_2, \varrho_3)$ of the three fluid species. Since the focus is on length scales larger than the sizes of the fluid particles and on weak wall-fluid interactions, the following dimensionless density functional within a Cahn-Hilliard-like square-gradient approximation [41] is considered:

$$\begin{aligned}\beta\Omega[\boldsymbol{\varrho}] = & \int_{\mathcal{V}} \mathrm{d}^3 r \, \Big[\beta\omega(\boldsymbol{\varrho}(\boldsymbol{r}), \boldsymbol{\mu}) + \frac{b}{2}\sum_{j=1}^{3}\big(\nabla\varrho_j(\boldsymbol{r})\big)^2 \\ & + \beta\frac{\varepsilon_0\varepsilon_r}{2}\big(\nabla\Psi(\boldsymbol{r}, [\boldsymbol{\varrho}])\big)^2\Big] \\ & - \int_{\mathcal{A}} \mathrm{d}^2 r_{\parallel} \, \boldsymbol{h}(\boldsymbol{r}_{\parallel}) \cdot \boldsymbol{\varrho}(\boldsymbol{r}_{\parallel}, z = 0),\end{aligned} \tag{3.1}$$

where $\beta = 1/(k_{\mathrm{B}}T)$ is the inverse thermal energy, and $\boldsymbol{\mu} = (\mu_1, \mu_2, \mu_3)$ are the chemical potentials of the three species. Furthermore, $b > 0$ is a phenomenological parameter with dimension $[b] = (\text{length})^5$, which can be inferred from microscopic models (see Sec. 3.3.1), $\varepsilon_0 \approx 8.854 \times 10^{-12}\,\mathrm{As/(Vm)}$ is the vacuum permittivity [138], ε_r is the relative dielectric constant of the fluid, $\Psi(\boldsymbol{r}, [\boldsymbol{\varrho}])$ is the electrostatic potential at $\boldsymbol{r} \in \mathcal{V}$, and $\boldsymbol{h}(\boldsymbol{r}_{\parallel}) = (h_1(\boldsymbol{r}_{\parallel}), h_2(\boldsymbol{r}_{\parallel}), h_3(\boldsymbol{r}_{\parallel}))$ describes the strengths of the nonelectrostatic wall-fluid interactions at $\boldsymbol{r} = (\boldsymbol{r}_{\parallel}, 0)$ for the three species. Note that for the sake of simplicity, the coupling of number density gradients of different particle types is neglected in Eq. (3.1) (see Sec. 3.3.1). In the present study the bulk state $\boldsymbol{\varrho}_b = (\varrho_{1,b}, \varrho_{2,b}, \varrho_{3,b})$ is considered to be thermodynamically far away from any phase transition so that the local contribution $\beta\omega(\boldsymbol{\varrho})$ of the density functional in Eq. (3.1) can be safely expanded around $\boldsymbol{\varrho}_b$ up to quadratic order in $\delta\boldsymbol{\varrho} := \boldsymbol{\varrho} - \boldsymbol{\varrho}_b$:

$$\beta\omega(\boldsymbol{\varrho}, \boldsymbol{\mu}) = \beta\omega(\boldsymbol{\varrho}_b, \boldsymbol{\mu}) + \frac{1}{2}\delta\boldsymbol{\varrho} \cdot \underline{\underline{\boldsymbol{M}}}\delta\boldsymbol{\varrho}, \tag{3.2}$$

where the local part of the interactions between different types of particles is captured by the real-valued, symmetric, and positively definite 3×3-matrix $\underline{\underline{\boldsymbol{M}}}$ (see Eq. (3.30)). Furthermore, $\omega(\boldsymbol{\varrho}_b, \boldsymbol{\mu}) = -p$ specifies the grand potential density, evaluated for the equilibrium bulk densities $\boldsymbol{\varrho}_b$, which equals minus the bulk pressure p; in the following its value is of no importance. For a given equation of state $p(\boldsymbol{\varrho}_b, T)$ the bulk densities $\boldsymbol{\varrho}_b = (\varrho_{1,b}, \varrho_{2,b}, \varrho_{3,b})$ are free parameters of the model. Finally, the electrostatic potential $\Psi(\boldsymbol{r}, [\boldsymbol{\varrho}])$, which enters into Eq. (3.1) on a mean-field level via the electric field energy

density, fulfills the Poisson equation

$$-\varepsilon_0\varepsilon_r\nabla^2\Psi(\boldsymbol{r},[\boldsymbol{\varrho}]) = e\boldsymbol{Z}\cdot\boldsymbol{\varrho}(\boldsymbol{r}) \tag{3.3}$$

for $\boldsymbol{r}\in\mathcal{V}$ with the boundary conditions

$$\frac{\partial}{\partial z}\Psi(\boldsymbol{r}_\parallel,z,[\boldsymbol{\varrho}])\bigg|_{z=0} = -\frac{1}{\varepsilon_0\varepsilon_r}\sigma(\boldsymbol{r}_\parallel), \quad \Psi(\boldsymbol{r}_\parallel,\infty)=0, \tag{3.4}$$

for $\boldsymbol{r}_\parallel\in\mathcal{A}$, where $\sigma(\boldsymbol{r}_\parallel)$ is the surface charge density at the point $\boldsymbol{r}=(\boldsymbol{r}_\parallel,0)$ on the wall surface ($z=0$), and $\boldsymbol{Z}=(Z_1,Z_2,Z_3)=(0,1,-1)$ denotes the valences of the fluid species.

The Euler-Lagrange equations, corresponding to the minimum of the density functional specified in Eqs. (3.1)–(3.4), can be written as

$$b\nabla^2\delta\boldsymbol{\varrho}(\boldsymbol{r}) = \underline{\underline{\boldsymbol{M}}}\delta\boldsymbol{\varrho}(\boldsymbol{r}) + \beta e\boldsymbol{Z}\Psi(\boldsymbol{r}) \tag{3.5}$$

and

$$-\frac{1}{4\pi l_B}\nabla^2\beta e\Psi(\boldsymbol{r}) = \boldsymbol{Z}\cdot\delta\boldsymbol{\varrho}(\boldsymbol{r}) \tag{3.6}$$

for $\boldsymbol{r}\in\mathcal{V}$ with the boundary conditions given by Eq. (3.4) and by

$$\frac{\partial}{\partial z}\delta\boldsymbol{\varrho}(\boldsymbol{r}_\parallel,0) = -\frac{1}{b}\boldsymbol{h}(\boldsymbol{r}_\parallel), \quad \delta\boldsymbol{\varrho}(\boldsymbol{r}_\parallel,\infty)=0 \tag{3.7}$$

for $\boldsymbol{r}_\parallel\in\mathcal{A}$, where $l_B=\beta e^2/(4\pi\varepsilon_0\varepsilon_r)$ is the Bjerrum length of the fluid.

The linear nature of the Euler-Lagrange equations (3.5) and (3.6) tells that the quadratic (Gaussian) approximation of the underlying density functional in Eqs. (3.1) and (3.2) corresponds to a linear response approach. It is widely assumed and in some cases it can be even quantified (see, e.g., the quantitative agreement between the full and the linearized Poisson-Boltzmann theory in the case that the surface charges are smaller than the saturation value [128, 139]) that for sufficiently weak wall-fluid interactions linear response theory provides quantitatively reliable results.

3.2.3 Solution of the Euler-Lagrange equations

Instead of solving the Euler-Lagrange equations in Eqs. (3.5) and (3.6) as differential equations for the profiles $\delta\boldsymbol{\varrho}$ and Ψ as functions of $\boldsymbol{r}=(\boldsymbol{r}_\parallel,z)$, it is convenient first to perform Fourier transformations with respect to the lateral coordinates $\boldsymbol{r}_\parallel$. The resulting

transformed profiles

$$\delta\widehat{\boldsymbol{\varrho}}(\boldsymbol{q}_\parallel, z) = \int_{\mathcal{A}} \mathrm{d}^2\boldsymbol{r}_\parallel \delta\boldsymbol{\varrho}(\boldsymbol{r}_\parallel, z) \exp(-i\boldsymbol{q}_\parallel \cdot \boldsymbol{r}_\parallel) \tag{3.8}$$

and $\widehat{\Psi}$ as functions of $\boldsymbol{q}_\parallel = (q_x, q_y) \in \mathbb{R}^2$ and $z \in \mathbb{R}$ can be combined in the four-component quantity $\boldsymbol{v}(\boldsymbol{q}_\parallel, z) = (\delta\widehat{\boldsymbol{\varrho}}(\boldsymbol{q}_\parallel, z), \beta e\widehat{\Psi}(\boldsymbol{q}_\parallel, z))$ so that Eqs. (3.5) and (3.6) can be written as

$$\underbrace{\begin{pmatrix} b & 0 & 0 & 0 \\ 0 & b & 0 & 0 \\ 0 & 0 & b & 0 \\ 0 & 0 & 0 & -\frac{1}{4\pi l_B} \end{pmatrix}}_{=: \underline{\underline{\boldsymbol{D}}}} \boldsymbol{v}'' = \underbrace{\begin{pmatrix} \boxed{\underline{\underline{\boldsymbol{M}}} + bk^2\underline{\underline{\mathbb{1}}}} & \begin{matrix} Z_1 \\ Z_2 \\ Z_3 \end{matrix} \\ \begin{matrix} Z_1 & Z_2 & Z_3 \end{matrix} & -\frac{k^2}{4\pi l_B} \end{pmatrix}}_{=: \underline{\underline{\boldsymbol{N}}}(k)} \boldsymbol{v}, \tag{3.9}$$

where $k := |\boldsymbol{q}_\parallel| = \sqrt{q_x^2 + q_y^2}$ and $\boldsymbol{v}''(\boldsymbol{q}_\parallel, z)$ is the second derivative of $\boldsymbol{v}(\boldsymbol{q}_\parallel, z)$ with respect to the coordinate z normal to the wall. Note that the components of $\boldsymbol{v}$ are quantities of different dimensions: $[v_1] = [v_2] = [v_3] = 1/\text{length}$ and $[v_4] = (\text{length})^2$. This does not allow for the formation of a scalar product of two vectors of the type $\boldsymbol{v} = (\delta\widehat{\boldsymbol{\varrho}}, \beta e\widehat{\Psi})$; however, in the following scalar products will not occur. Writing $\underline{\underline{\boldsymbol{D}}} = \underline{\underline{\boldsymbol{T}}}\,\underline{\underline{\boldsymbol{T}}}$ with $\underline{\underline{\boldsymbol{T}}} := \mathrm{diag}(\sqrt{b}, \sqrt{b}, \sqrt{b}, i\sqrt{1/(4\pi l_B)})$ (i.e., $\underline{\underline{\boldsymbol{T}}}$ is a diagonal matrix with these entries), one obtains

$$\underline{\underline{\boldsymbol{T}}}\boldsymbol{v}''(\boldsymbol{q}_\parallel, z) = \underbrace{\underline{\underline{\boldsymbol{T}}}^{-1}\underline{\underline{\boldsymbol{N}}}(k)\underline{\underline{\boldsymbol{T}}}^{-1}}_{=: \underline{\underline{\boldsymbol{H}}}(k)} \underline{\underline{\boldsymbol{T}}}\boldsymbol{v}(\boldsymbol{q}_\parallel, z). \tag{3.10}$$

The 4×4-matrix $\underline{\underline{\boldsymbol{H}}}(k)$ is independent of z and it is symmetric but not real-valued, because the bottom entry of $\underline{\underline{\boldsymbol{T}}}$ is imaginary. $\underline{\underline{\boldsymbol{H}}}(k)$ is not a normal matrix, i.e., it does not commute with its adjoint matrix $\underline{\underline{\boldsymbol{H}}}(k)^\dagger$, and hence it does not possess an *orthogonal* basis composed of eigenvectors. However, the actual structures of the matrix $\underline{\underline{\boldsymbol{M}}}$ and of the vector $\boldsymbol{Z}$ used below guarantee the existence of a *nonorthogonal* basis $\{\boldsymbol{\Lambda}_1(k), \ldots, \boldsymbol{\Lambda}_4(k)\}$ of eigenvectors of the matrix $\underline{\underline{\boldsymbol{H}}}(k)$ with respective positive (real-valued) eigenvalues $\lambda_1(k), \ldots, \lambda_4(k) \in (0, \infty)$ (see Sec. 3.A). Expanding the vector $\underline{\underline{\boldsymbol{T}}}\boldsymbol{v}(\boldsymbol{q}_\parallel, z)$ in this basis $\{\boldsymbol{\Lambda}_1(k), \ldots, \boldsymbol{\Lambda}_4(k)\}$,

$$\underline{\underline{\boldsymbol{T}}}\boldsymbol{v}(\boldsymbol{q}_\parallel, z) = \sum_{\alpha=1}^{4} A_\alpha(\boldsymbol{q}_\parallel, z)\ \boldsymbol{\Lambda}_\alpha(k), \tag{3.11}$$

leads to Eq. (3.10) in the form

$$A_\alpha''(\boldsymbol{q}_\parallel, z) = \lambda_\alpha(k) A_\alpha(\boldsymbol{q}_\parallel, z) \tag{3.12}$$

with the solution

$$A_\alpha(\boldsymbol{q}_\parallel, z) = g_\alpha(\boldsymbol{q}_\parallel)\ \exp(-\sqrt{\lambda_\alpha(k)}z), \tag{3.13}$$

where the second boundary conditions in Eqs. (3.4) and (3.7) have been used. Therefore, the solution of Eq. (3.10) can be expressed as

$$\boldsymbol{v}(\boldsymbol{q}_\parallel, z) = \sum_{\alpha=1}^{4} g_\alpha(\boldsymbol{q}_\parallel)\ \exp(-\sqrt{\lambda_\alpha(k)}z)\ \underline{\underline{\boldsymbol{T}}}^{-1}\boldsymbol{\Lambda}_\alpha(k). \tag{3.14}$$

Finally, the first boundary conditions in Eqs. (3.4) and (3.7) can be expressed as

$$\boldsymbol{v}'(\boldsymbol{q}_\parallel, 0) = \left(-\frac{1}{b}\widehat{\boldsymbol{h}}(\boldsymbol{q}_\parallel), -\frac{\beta e}{\varepsilon_0\varepsilon_r}\widehat{\sigma}(\boldsymbol{q}_\parallel)\right), \tag{3.15}$$

with

$$\widehat{\boldsymbol{h}}(\boldsymbol{q}_\parallel) = \int_{\mathcal{A}} \mathrm{d}^2 r_\parallel \exp(-i\boldsymbol{q}_\parallel \cdot \boldsymbol{r}_\parallel)\boldsymbol{h}(\boldsymbol{r}_\parallel) \tag{3.16}$$

as the Fourier transform of $\boldsymbol{h}(\boldsymbol{r}_\parallel)$ with respect to the lateral coordinates $\boldsymbol{r}_\parallel$ and $\widehat{\sigma}(\boldsymbol{q}_\parallel)$ as the Fourier transform of $\sigma(\boldsymbol{r}_\parallel)$. Note that, as for $\boldsymbol{v}$, the components of $\boldsymbol{v'}$ are quantities of different dimensions: $[v_1'] = [v_2'] = [v_3'] = 1/(\text{length})^2$ and $[v_4] = \text{length}$. From Eqs. (3.14) and (3.15) the coefficients $g_1(\boldsymbol{q}_\parallel), \ldots, g_4(\boldsymbol{q}_\parallel)$ can be determined. Note that according to Eqs. (3.14) and (3.15) the coefficients $g_1(\boldsymbol{q}_\parallel), \ldots, g_4(\boldsymbol{q}_\parallel)$ and hence the profiles $\widehat{\boldsymbol{\varrho}}$ and $\widehat{\Psi}$ depend linearly on the nonelectrostatic wall-fluid interactions $\widehat{\boldsymbol{h}}(\boldsymbol{q}_\parallel)$ and the surface charge density $\widehat{\sigma}(\boldsymbol{q}_\parallel)$. Such a linear response of the number density profiles inside the fluid to the wall properties requires weak wall-fluid interactions, which is assumed in the present study and which is consistent with the quadratic form of the density functional in Eqs. (3.1)–(3.4).

3.3 Results and Discussion

3.3.1 Choice of parameters

The present study discusses the influence of the wall-fluid interactions, represented by the nonelectrostatic wall-fluid interactions $\widehat{\boldsymbol{h}}(\boldsymbol{q}_\parallel)$ and the surface charge density $\widehat{\sigma}(\boldsymbol{q}_\parallel)$, onto the number density profiles $\boldsymbol{\varrho}$ in the adjacent fluid. Applying density functional theory as described in Sec. 3.2 requires knowledge of the bulk number densities $\boldsymbol{\varrho}_b$, the parameter b, and the coupling matrix $\underline{\underline{\boldsymbol{M}}}$ all of which are bulk quantities or characterize them.

In the bulk local charge neutrality holds, i.e., $\boldsymbol{Z} \cdot \boldsymbol{\varrho}_b = 0$. Hence, the equilibrium bulk

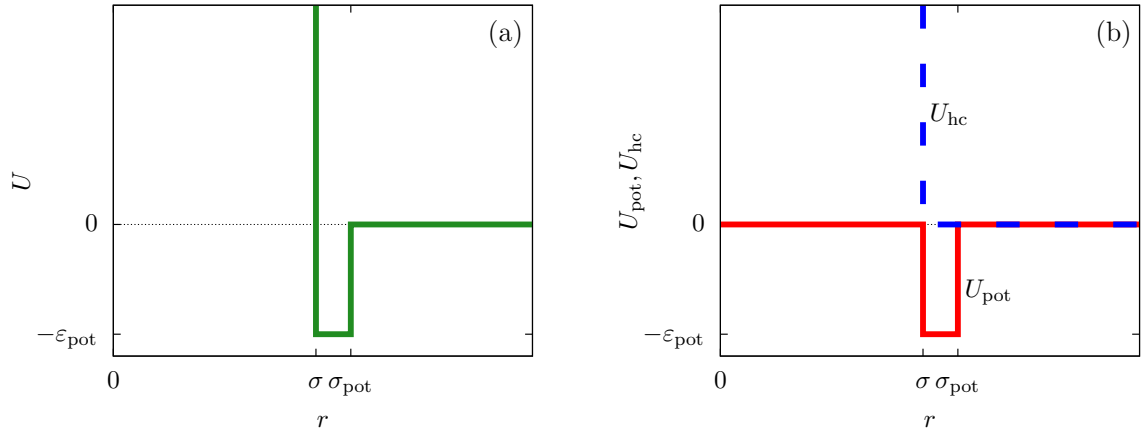

Figure 3.1: The nonelectrostatic interaction between fluid particles is modeled by a square-well pair potential $U(r)$ displayed in panel (a), where r denotes the distance between the centers of two spherical particles. For $r < \sigma$ a hard core repulsion prevents the overlap of two particles. For $r \in (\sigma, \sigma_{\rm pot})$ two particles attract each other with a constant interaction energy $-\varepsilon_{\rm pot} < 0$. At distances $r > \sigma_{\rm pot}$ there is no nonelectrostatic interaction. Panel (b) sketches the decomposition $U = U_{\rm hc} + U_{\rm pot}$ of the nonelectrostatic interaction potential U according to the scheme due to Barker and Henderson into the hard core repulsion $U_{\rm hc}$ and the attractive well $U_{\rm pot}$, which is used in Sec. 3.3.1 in order to obtain the parameters entering the Cahn-Hilliard square-gradient density functional in Eq. (3.1).

state is determined by the temperature T, the number density $\varrho_{1,b}$ of the solvent, and the bulk ionic strength $I = \varrho_{2,b} = \varrho_{3,b}$.

In order to obtain expressions for the parameter b and for the coupling matrix $\underline{\underline{\boldsymbol{M}}}$ in terms of experimentally accessible quantities, in a first step the pure, ion-free solvent is considered, the particles of which interact only nonelectrostatically. Here this nonelectrostatic interaction between solvent particles at a distance r is modeled by a square-well pair potential $U(r)$ as displayed in Fig. 3.1 (a). At small distances $r < \sigma$ a hard core repulsion prevents the overlap of two particles. At intermediate distances $r \in (\sigma, \sigma_{\rm pot})$ two particles attract each other with an interaction energy $-\varepsilon_{\rm pot}$, and at distances $r > \sigma_{\rm pot}$ the nonelectrostatic interaction vanishes. According to the scheme due to Barker and Henderson [65], the interaction potential U can be decomposed as $U = U_{\rm hc} + U_{\rm pot}$ into the hard core repulsion $U_{\rm hc}$ and the attractive well $U_{\rm pot}$ (see Fig. 3.1 (b)). The microscopic density functional $\Omega_1^{\rm mic}[\varrho_1]$ for the pure solvent (species 1) in the bulk can be approximated by the expression

$$\beta\Omega_1^{\rm mic}[\varrho_1] = \beta\Omega_1^{\rm hc}[\varrho_1] + \beta F^{\rm ex,pot}[\varrho_1]. \tag{3.17}$$

The contribution Ω_1^{mic} (here within local density approximation (LDA)) is due to the reference system governed solely by the hard core interaction U_{hc}:

$$\beta\Omega_1^{\mathrm{hc}}[\varrho_1] = \int_{\mathcal{V}} \mathrm{d}^3r \ \left[\varrho_1(\boldsymbol{r})\left(\ln(\varrho_1(\boldsymbol{r})\Lambda_1^3) - 1 - \beta\mu_1\right) + \beta f^{\mathrm{ex,hc}}(\varrho_1(\boldsymbol{r}))\right]. \tag{3.18}$$

Here, contributions of external potentials are neglected, because they do not contribute to the bulk parameters b and $\underline{\underline{\boldsymbol{M}}}$. The second term on the right-hand side of Eq. (3.17) is (within *random phase approximation* (RPA) [57]) the excess free energy functional due to the square-well attractive interaction U_{pot}:

$$\beta F^{\mathrm{ex,pot}}[\varrho_1] = \frac{1}{2}\int_{\mathcal{V}} \mathrm{d}^3r \int_{\mathcal{V}} \mathrm{d}^3r' \ \beta U_{\mathrm{pot}}(\boldsymbol{r}-\boldsymbol{r'})\varrho_1(\boldsymbol{r})\varrho_1(\boldsymbol{r'}). \tag{3.19}$$

In Eq. (3.18) Λ_1 is the thermal de Broglie wavelength, μ_1 denotes the chemical potential of species 1, and $f^{\mathrm{ex,hc}}(\varrho_1)$ is the excess free energy per volume of the reference system governed by the hard core interaction U_{hc}.

Following Cahn and Hilliard [41], Eq. (3.19) can be approximated by a gradient expansion:

$$\beta F^{\mathrm{ex,pot}}[\varrho_1] \simeq \int_{\mathcal{V}} \mathrm{d}^3r \ \left[\frac{K_0}{2}\left(\varrho_1(\boldsymbol{r})\right)^2 - \frac{K_2}{12}\left(\nabla\varrho_1(\boldsymbol{r})\right)^2\right] \tag{3.20}$$

with the m-th moment of the pair potential U_{pot} in units of $k_{\mathrm{B}}T$,

$$K_m = \int_{\mathbb{R}^3} \mathrm{d}^3r \ |\boldsymbol{r}|^m \beta U_{\mathrm{pot}}(|\boldsymbol{r}|), \tag{3.21}$$

which, for the present form of U_{pot}, leads to

$$\begin{aligned} K_0 &= -\frac{4\pi}{3}\beta\varepsilon_{\mathrm{pot}}\left(\sigma_{\mathrm{pot}}^3 - \sigma^3\right) < 0, \\ K_2 &= -\frac{4\pi}{5}\beta\varepsilon_{\mathrm{pot}}\left(\sigma_{\mathrm{pot}}^5 - \sigma^5\right) < 0. \end{aligned} \tag{3.22}$$

From Eq. (3.20) one obtains the gradient expansion of $\beta\Omega_1^{\mathrm{mic}}[\varrho_1]$ in Eq. (3.17):

$$\beta\Omega_1^{\mathrm{mic}}[\varrho_1] \simeq \int_{\mathcal{V}} \mathrm{d}^3r \ \left[\beta\omega_1^{\mathrm{loc}}(\varrho_1(\boldsymbol{r}),\mu_1) - \frac{K_2}{12}\left(\nabla\varrho_1(\boldsymbol{r})\right)^2\right] \tag{3.23}$$

with the local contribution

$$\begin{aligned}\beta\omega_1^{\mathrm{loc}}(\varrho_1,\mu_1) =& \varrho_1\left(\ln(\varrho_1\Lambda_1^3)-1-\beta\mu_1\right)\\ &+\beta f^{\mathrm{ex,hc}}(\varrho_1)+\frac{K_0}{2}\varrho_1^2.\end{aligned} \tag{3.24}$$

The comparison of Eq. (3.23) with Eq. (3.1) renders an expression for the parameter b in terms of parameters of the interaction potential U (see Fig. 3.1):

$$b=-\frac{K_2}{6}=\frac{2\pi}{15}\beta\varepsilon_{\mathrm{pot}}\left(\sigma_{\mathrm{pot}}^5-\sigma^5\right). \tag{3.25}$$

By expanding $\beta\omega_1^{\mathrm{loc}}(\varrho_1,\mu_1)$ up to quadratic order in the density deviation $\delta\varrho_1=\varrho_1-\varrho_{1,b}$ from the equilibrium bulk density $\varrho_{1,b}$, which is a solution of the Euler-Lagrange equation

$$0=\frac{\partial\ (\beta\omega_1^{\mathrm{loc}})}{\partial\varrho_1}(\varrho_{1,b},\mu_1), \tag{3.26}$$

one obtains

$$\begin{aligned}\beta\omega_1^{\mathrm{loc}}(\varrho_1,\mu_1) &\simeq \beta\omega_1^{\mathrm{loc}}(\varrho_{1,b},\mu_1)+\frac{1}{2}\frac{\partial^2\ (\beta\omega_1^{\mathrm{loc}})}{(\partial\varrho_1)^2}(\varrho_{1,b},\mu_1)(\delta\varrho_1)^2\\ &=\beta\omega_1^{\mathrm{loc}}(\varrho_{1,b},\mu_1)+\frac{1}{2}\left(\frac{1}{\varrho_{1,b}}+\frac{\mathrm{d}^2\ (\beta f^{\mathrm{ex,hc}}(\varrho_{1,b}))}{(\mathrm{d}\varrho_{1,b})^2}+K_0\right)(\delta\varrho_1)^2.\end{aligned} \tag{3.27}$$

The comparison with Eq. (3.2) leads to the matrix element

$$M_{11}=\frac{1}{\varrho_{1,b}}+\frac{\mathrm{d}^2\ (\beta f^{\mathrm{ex,hc}}(\varrho_{1,b}))}{(\mathrm{d}\varrho_{1,b})^2}+K_0 \tag{3.28}$$

of the matrix $\underline{\underline{\boldsymbol{M}}}$, where the first term on the rhs stems from the ideal gas contribution of the solvent particles. The argument $\varrho_{1,b}$ of the second term, which is due to the hard core interaction U_{hc}, is a measure of the packing fraction $\eta=\pi\varrho_{1,b}\sigma^3/6$.

The analogue of Eq. (3.23) for the nonelectrostatic contribution of all *three* particle species is given by the first line of Eq. (3.1) with the local contribution (compare Eq. (3.24))

$$\begin{aligned}\beta\omega^{\mathrm{loc}}(\boldsymbol{\varrho},\boldsymbol{\mu}) =& \sum_{i=1}^{3}\varrho_i\left(\ln(\varrho_i\Lambda_i^3)-1-\beta\mu_i\right)\\ &+\beta f^{\mathrm{ex,hc}}(\varrho^{\mathrm{tot}})+\sum_{i,j=1}^{3}\frac{K_0}{2}\varrho_i\varrho_j,\end{aligned} \tag{3.29}$$

where $\varrho^{\mathrm{tot}} = \varrho_1 + \varrho_2 + \varrho_3$ denotes the total number density. Note that Eq. (3.29) assumes, that all interactions among the species are the same (see Eq. (3.21)). This implies that the last term in Eq. (3.29) takes the form $\frac{K_0}{2}(\varrho^{\mathrm{tot}})^2$. By expanding $\beta\omega^{\mathrm{loc}}(\boldsymbol{\varrho}, \boldsymbol{\mu})$ up to quadratic order in the density deviations $\delta\boldsymbol{\varrho} = \boldsymbol{\varrho} - \boldsymbol{\varrho}_b$ from the equilibrium bulk densities $\boldsymbol{\varrho}_b$ one finally finds (see the steps leading to Eq. (3.28))

$$\begin{aligned} M_{ij} &= \frac{\delta_{ij}}{\varrho_{i,b}} + \frac{\mathrm{d}^2\ (\beta f^{\mathrm{ex,hc}}(\varrho_b^{\mathrm{tot}}))}{(\mathrm{d}\varrho_b^{\mathrm{tot}})^2} + K_0 \\ &= \frac{\delta_{ij}}{\varrho_{i,b}} + \frac{\mathrm{d}^2\ (\beta f^{\mathrm{ex,hc}}(\varrho_b^{\mathrm{tot}}))}{(\mathrm{d}\varrho_b^{\mathrm{tot}})^2} - \frac{4\pi}{3}\beta\varepsilon_{\mathrm{pot}}\left(\sigma_{\mathrm{pot}}^3 - \sigma^3\right), \\ & i \in \{1,2,3\}, \end{aligned} \tag{3.30}$$

where $\varrho_b^{\mathrm{tot}} = \varrho_{1,b} + \varrho_{2,b} + \varrho_{3,b} = \varrho_{1,b} + 2I$ denotes the total number density in the bulk. In the present study the hard core excess free energy per volume $f^{\mathrm{ex,hc}}(\varrho_b)$ is chosen as the one corresponding to the Carnahan-Starling equation of state [65]:

$$\beta f^{\mathrm{ex,hc}}(\varrho_b^{\mathrm{tot}}) = \varrho_b^{\mathrm{tot}} \frac{\eta(4-3\eta)}{(1-\eta)^2} \tag{3.31}$$

here with the packing fraction $\eta = \pi\varrho_b^{\mathrm{tot}}\sigma^3/6$.

Accordingly, from Eq. (3.24) one obtains the following equation of state of the *pure* solvent:

$$\beta p(\varrho_{1,b}) = \varrho_{1,b}\frac{1+\eta+\eta^2-\eta^3}{(1-\eta)^3} + \frac{K_0}{2}(\varrho_{1,b})^2. \tag{3.32}$$

Its derivative with respect to the number density $\varrho_{1,b}$, using the relation $\partial p/\partial\varrho_{1,b} = 1/(\kappa_T\varrho_{1,b})$ with the isothermal compressibility κ_T, yields

$$\frac{\beta}{\kappa_T\varrho_{1,b}} = \frac{1+4\eta+4\eta^2-4\eta^3-\eta^4}{(1-\eta)^4} + K_0\varrho_{1,b}. \tag{3.33}$$

As an exemplary fluid I consider water at room temperature $T = 300\,\mathrm{K}$ and ambient pressure $p = 1\,\mathrm{bar}$ (which corresponds to the number density $\varrho_{1,b} = 55.5\,\mathrm{M} \approx 33.3\,\mathrm{nm}^{-3}$ and the isothermal compressibility $\kappa_T = 4.5 \times 10^{-10}\,\mathrm{Pa}^{-1}$ [138]) with relative dielectric constant $\varepsilon_r = 80$, i.e., with Bjerrum length $l_B = 0.7\,\mathrm{nm}$, and with a univalent salt of ionic strength $I = 1\,\mathrm{mM} \approx 6 \times 10^{-4}\,\mathrm{nm}^{-3}$. The strength of hydrogen bonds, which generate the dominant attractive interaction contribution, is of the order of $\varepsilon_{\mathrm{pot}} \approx 20\,\mathrm{kJ\,mol}^{-1} \approx 8\,k_{\mathrm{B}}T$ [138, 140]. Using these data, one obtains from Eqs. (3.32) and (3.33) the bulk packing

fraction $\eta \approx 0.44$ as well as $\sigma = 2.9\,\text{Å}$ and $\sigma_{\text{pot}} = 3.4\,\text{Å}$. In the following the Debye length

$$\frac{1}{\kappa} = \sqrt{\frac{1}{8\pi l_B I}} \tag{3.34}$$

is used as length scale, which, for the present choice of parameters, is $1/\kappa \approx 10\,\text{nm}$.

In the case of a pure solvent ($\delta\varrho_2 = \delta\varrho_3 = \Psi = 0$), in the bulk the density two-point correlation function $G(\boldsymbol{r}_1, \boldsymbol{r}_2) = \bar{G}(\boldsymbol{r}_1 - \boldsymbol{r}_2)$ fulfills an equation similar to Eq. (3.5):

$$b\nabla^2 \bar{G}(\boldsymbol{r}) = M_{11}\bar{G}(\boldsymbol{r}). \tag{3.35}$$

Note that the similarity between Eqs. (3.5) and (3.35) is due to the asymptotic proportionality between density deviations and two-point correlation functions (Yvon equation) [65]. From Eq. (3.35), one can readily infer the relation

$$\xi = \sqrt{\frac{b}{M_{11}}} \tag{3.36}$$

for the solvent bulk correlation length, which characterizes the exponential decay of $\bar{G}(\boldsymbol{r})$. For the present choice of parameters, one has $\xi \approx 1.3\,\text{Å}$ so that $\kappa\xi \approx 0.013$.

3.3.2 X-ray scattering

In the following subsections the Fourier transforms $\delta\widehat{\boldsymbol{\varrho}} = (\delta\widehat{\varrho}_1, \delta\widehat{\varrho}_2, \delta\widehat{\varrho}_3)$ of the profiles of the density deviations as functions of the lateral wave vector $\boldsymbol{q}_\parallel$ and of the normal distance z from the wall are discussed in detail. However, from the experimental point of view, it is challenging to directly obtain the z-dependence of the density profiles. One of such direct methods is *total internal reflection microscopy* (TIRM) [141] in the context of the structure of colloidal suspensions close to (optically transparent) substrates. In contrast, for molecular fluids, as the ones considered here, such direct methods are not available and one has to resort to, e.g., X-ray scattering techniques [142, 143]. As X-rays are predominantly scattered by the electrons of the fluid molecules one has to consider the electron number density

$$\varrho^e(\boldsymbol{r}_\parallel, z) = \sum_{j=1}^{3} N_j \varrho_j(\boldsymbol{r}_\parallel, z) = \begin{cases} \varrho_b^e + \delta\varrho^e(\boldsymbol{r}_\parallel, z) & , z > 0 \\ 0 & , z < 0 \end{cases} \tag{3.37}$$

for $\boldsymbol{r}_\parallel \in \mathcal{A}$ with the number N_j of electrons per molecule of particle species $j \in \{1, 2, 3\}$, the bulk electron density $\varrho_b^e = \sum_{j=1}^{3} N_j \varrho_{j,b}$, and the deviation $\delta\varrho^e = \varrho^e - \varrho_b^e = \sum_{j=1}^{3} N_j \delta\varrho_j$ of the electron number density from its bulk value. The X-ray scattering signal for scat-

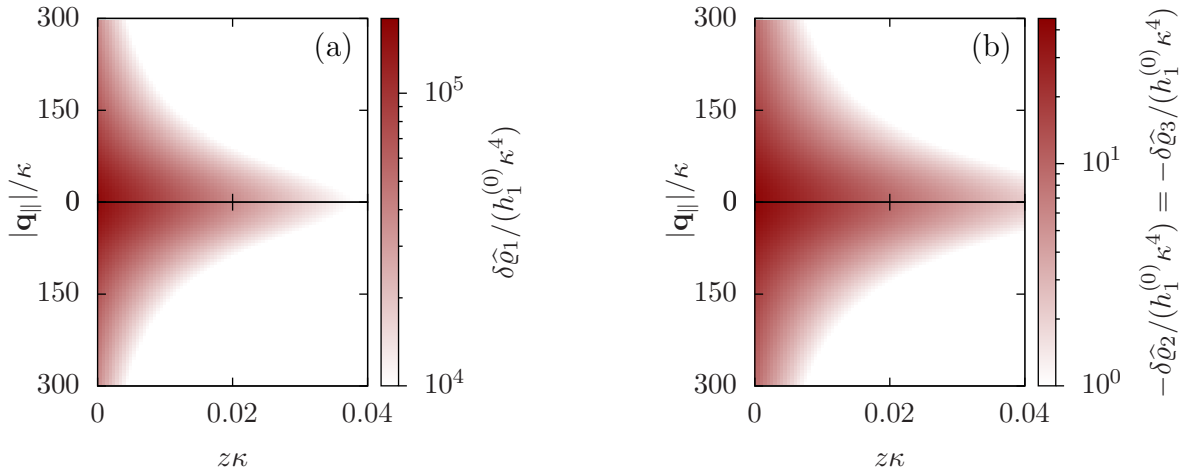

Figure 3.2: Density distribution $\delta\widehat{\varrho}_1(\boldsymbol{q}_\parallel, z)$ of the solvent (panel (a)) and of the ions $\delta\widehat{\varrho}_2(\boldsymbol{q}_\parallel, z) = \delta\widehat{\varrho}_3(\boldsymbol{q}_\parallel, z)$ (panel (b)) as function of the distance z from the wall and of the absolute value of the lateral Fourier wave vector $\boldsymbol{q}_\parallel$ in units of the inverse Debye length κ (see Eq. (3.34)). The plane $z = 0$ is given by the positions of the fluid particle centers when the surface-to-surface distance between the hard wall and the hard particles vanishes. The data correspond to the boundary condition $\boldsymbol{v}' = -\frac{h_1^{(0)}}{b}(1, 0, 0, 0)$ (see Eqs. (3.15) and (3.40)). The physical situation corresponding to this boundary condition is an attraction $h_1(\boldsymbol{r}_\parallel) = h_1^{(0)}\delta(\boldsymbol{r}_\parallel)$ (see Eq. (3.42)) of the solvent particles by the wall located at the origin of the wall. Concerning the remaining relevant parameters see Sec. 3.3.1.

tering vector $\boldsymbol{q} = (\boldsymbol{q}_\parallel, q_z)$ is proportional to $\left|\widehat{\widehat{\varrho^e}}(\boldsymbol{q}_\parallel, q_z)\right|^2$ with the double Fourier transform $\widehat{\widehat{\varrho^e}}$ of the electron number density profile ϱ^e in both the lateral and the normal direction [65].

For common specular X-ray reflectivity measurements, i.e., for $\boldsymbol{q}_\parallel = 0$, the normalized intensity reflected as function of the normal wave number q_z is given by [142, 143]

$$\frac{R(q_z)}{R^{\mathrm{F}}(q_z)} = \left|1 + \frac{iq_z\delta\widehat{\widehat{\varrho^e}}(\boldsymbol{q}_\parallel = 0, q_z)}{|\mathcal{A}|\varrho_b^e}\right|^2, \tag{3.38}$$

where $R^{\mathrm{F}}(q_z)$ denotes the Fresnel reflectivity of an ideal, step-like planar interface [144], and where the notation $\delta\widehat{\widehat{\varrho^e}} := \sum_{j=1}^{3} N_j\delta\widehat{\widehat{\varrho}}_j$ with

$$\delta\widehat{\widehat{\varrho}}_j(\boldsymbol{q}_\parallel, q_z) = \int_0^\infty \mathrm{d}z\ \delta\widehat{\varrho}(\boldsymbol{q}_\parallel, z)\exp(-iq_z z) \tag{3.39}$$

has been used. Moreover, off-specular diffuse X-ray scattering ($\boldsymbol{q}_\parallel \neq 0$) at grazing

incidence (GIXD, Im $q_z \neq 0$) yields scattering intensities which are proportional to $\left|\delta\widehat{\varrho^e}(\boldsymbol{q}_\parallel, q_z)\right|^2$ [143]. Hence, as the double Fourier transforms $\delta\widehat{\widehat{\varrho}}_j$ in Eq. (3.39) of the density deviation profiles $\delta\varrho_j$ are of direct experimental relevance, they will be discussed in the following in parallel to the single Fourier transforms $\delta\widehat{\varrho}_j$. Note that due to $\delta\widehat{\widehat{\varrho}}_i \in \mathbb{C}$, in Figs. 3.3 and 3.5 its absolute value is shown.

3.3.3 Basis vectors of boundary conditions

As mentioned above, the linear nature of the relationship between wall nonuniformities and the resulting number density deviations leads to the possibility of describing the latter in terms of linear combinations of elementary response patterns. These elementary response patterns correspond to four basis vectors, e.g., $(1,0,0,0), (0,1,0,0), (0,0,1,0)$, and $(0,0,0,1)$, which span the four-dimensional space of boundary conditions $\boldsymbol{v}'(\boldsymbol{q}_\parallel, 0)$ in Eq. (3.15). Therefore, as a first step to study the influence of wall inhomogeneities onto the fluid, these four distinct boundary condition vectors $\boldsymbol{v}'(\boldsymbol{q}_\parallel, 0)$ are studied. The first one of these vectors is given by

$$\boldsymbol{v}'(\boldsymbol{q}_\parallel, 0) = -\frac{h_1^{(0)}}{b}(1,0,0,0), \tag{3.40}$$

which requires (see Eq. (3.15))

$$\begin{aligned} \widehat{h_1}(\boldsymbol{q}_\parallel) &= h_1^{(0)}, \\ \widehat{h_2}(\boldsymbol{q}_\parallel) = \widehat{h_3}(\boldsymbol{q}_\parallel) &= \widehat{\sigma}(\boldsymbol{q}_\parallel) = 0, \end{aligned} \tag{3.41}$$

and which in real space corresponds to the boundary condition

$$\begin{aligned} h_1(\boldsymbol{r}_\parallel) &= h_1^{(0)}\ \delta(\boldsymbol{r}_\parallel), \\ h_2(\boldsymbol{r}_\parallel) = h_3(\boldsymbol{r}_\parallel) &= \sigma(\boldsymbol{r}_\parallel) = 0. \end{aligned} \tag{3.42}$$

This boundary condition corresponds to an attractive, δ-like interaction of the wall with the solvent located at the origin. Solving the Euler-Lagrange equations for this boundary condition, one finds the density distribution $\delta\widehat{\varrho_1}(\boldsymbol{q}_\parallel, z)$ for the solvent and $\delta\widehat{\varrho_2}(\boldsymbol{q}_\parallel, z) = \delta\widehat{\varrho_3}(\boldsymbol{q}_\parallel, z)$ for the ions, as shown in Figs. 3.2 (a) and 3.2 (b), respectively. Since the boundary condition corresponds to a constant in Fourier space, the density distribution $\boldsymbol{v}(\boldsymbol{q}_\parallel, z)$ depends on $k = |\boldsymbol{q}_\parallel|$ only. Actually, the solution $\boldsymbol{v}(\boldsymbol{q}_\parallel, z)$ for this system is proportional to the first column of the Green's function, which is a 4×4-matrix, of the differential operator corresponding to Eqs. (3.5) and (3.6).

Figure 3.2 illustrates that for fixed $|\boldsymbol{q}_\parallel|$ the density deviations from the bulk value increase for smaller normal distances from the wall and, for fixed z, also upon decreasing the absolute value of the lateral wave vector $|\boldsymbol{q}_\parallel|$. The behavior with respect to the normal distance from the wall can be anticipated, because the effect of the interaction between the wall and the fluid is expected to decrease with increasing distance from the wall. Moreover, also the behavior with respect to $|\boldsymbol{q}_\parallel|$ is as expected, because a strong attraction at the origin leads to a radially decreasing density deviation, which in Fourier space corresponds to a maximum at the origin. In order to allow for a quantitative analysis of the behavior of the density deviations, Figs. 3.3 and 3.4 show various cuts through the data of Fig. 3.2 along several lines.

Figures 3.3 (a), (c), and 3.4 (a) show the density profiles for the solvent and Figs. 3.3 (b), (d), and 3.4 (b) the ones of the positive ions, which in this case are the same as the profiles for the negative ions. This equivalence is due to the nature of the boundary conditions in this special case, which in real space lead primarily to an increased solvent density close to the origin at the wall. The ions, however, react only indirectly via the solvent, with which both ion types interact in the same way. Since the solvent particles get attracted by the wall, it is favorable to increase their density close to the wall. Due to the hard core nature of the particles, the space occupied by the solvent particles is blocked for the ions. Since the solvent is attracted by the wall and the interparticle attraction is the same for all pairs of particles, this leads to an extrusion of the ions in favor of an increased number of solvent particles. Figures 3.3 (a) and (b) show the density deviations as function of the normal distance z from the wall for three values of $|\boldsymbol{q}_\parallel|$, i.e., Figs. 3.3 (a) and (b) correspond to horizontal cuts through Figs. 3.2 (a) and (b), respectively. For fixed $|\boldsymbol{q}_\parallel|$, as in Figs. 3.2 (a) and (b), Figs. 3.3 (a) and (b) clearly show an exponential decay of the density deviation for increasing distances from the wall. In contrast, Figs. 3.3 (c) and (d) show vertical cuts through Figs. 3.2 (a) and (b), i.e., density profiles as functions of the absolute value of the lateral wave number $|\boldsymbol{q}_\parallel|$ for three normal distances z from the wall. The dependence of these profiles on the absolute value $|\boldsymbol{q}_\parallel|$ of the lateral wave vector $\boldsymbol{q}_\parallel$ implies a laterally isotropic decay of the density deviations in real space. The third pair of graphs, Figs. 3.4 (a) and (b), shows the Fourier transforms of the density profiles of Figs. 3.3 (a) and (b), being additionally Fourier-transformed with respect to the normal direction z, which leads to the Fourier transforms $\delta\widehat{\widehat{\varrho}}(\boldsymbol{q}_\parallel, q_z)$ in terms of the lateral wave vector $\boldsymbol{q}_\parallel$ and the normal wave number q_z, respectively. All curves in Figs. 3.3 (c), (d), 3.4 (a), and (b) exhibit a Lorentzian shape as functions of $|\boldsymbol{q}_\parallel|$ and q_z, respectively. These Lorentzian curves in Fourier space correspond to exponential decays in real space in lateral or normal direction. The curves in Figs. 3.3 (c) and (d) show widths of half height which decrease with increasing normal distance z, i.e., the lateral decay length in

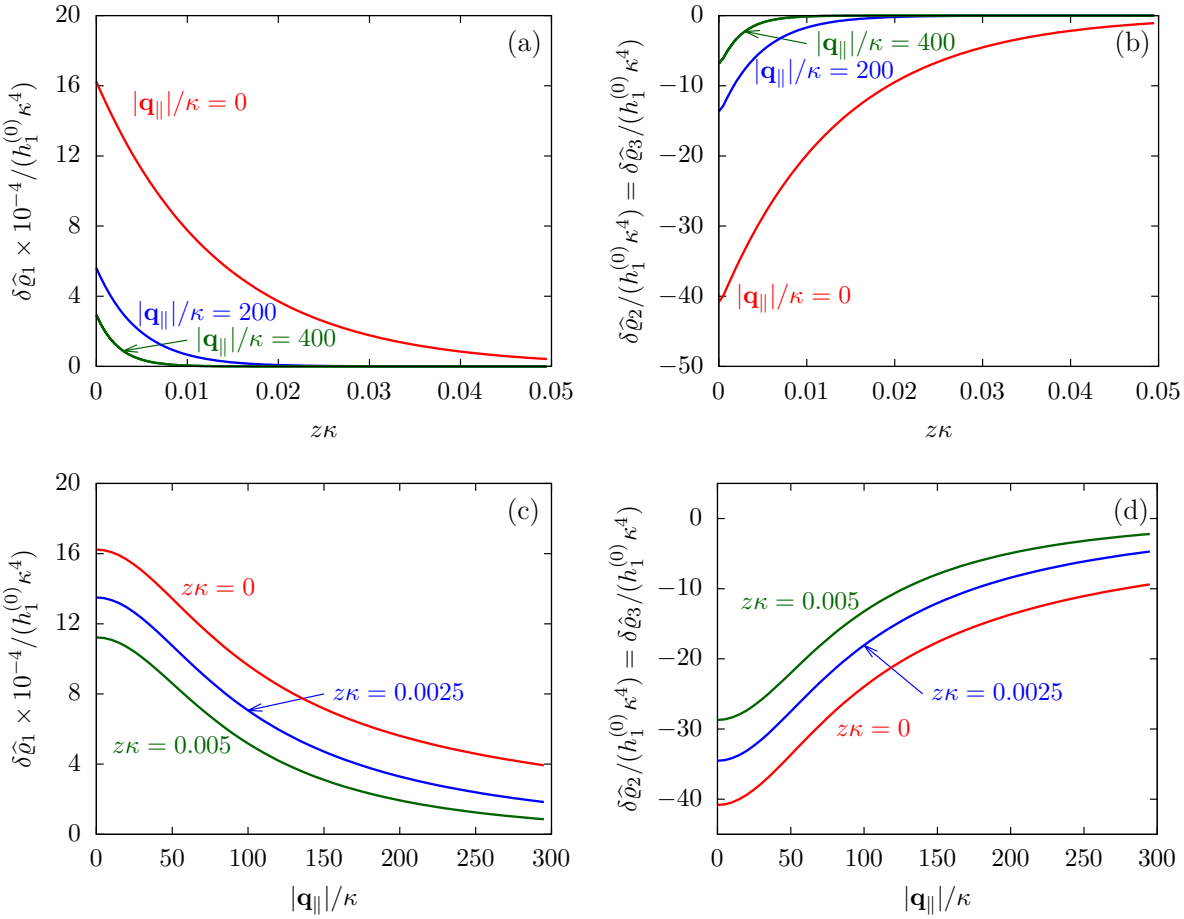

Figure 3.3: Density profiles of the solvent (left column, panels (a) and (c)) and of the ions (right column, panels (b) and (d)) as functions of the normal distance z from the wall (top row, panels (a) and (b)) and of the absolute value of the lateral wave vector $|\boldsymbol{q}_\parallel|$ (bottom row, panels (c) and (d)) in corresponding units of the Debye length $1/\kappa$ and the inverse Debye length, respectively (see Eq. (3.34)). In each graph, there are three profiles shown corresponding to three values of the other relevant variable. Therefore, the profiles correspond to cuts through Figs. 3.2 (a) and (b) at various positions and in different directions. In this case the boundary condition is $\boldsymbol{v}' = -\frac{h_1^{(0)}}{b}(1,0,0,0)$ (see Eqs. (3.15) and (3.40)), corresponding to a δ-like nonelectrostatic attraction of the solvent particles at the origin of the wall (see Fig. 3.2 and Eq. (3.42)). The graphs show, that the density deviations of the ions are proportional to the ones of the solvent, although different in sign. Since only the solvent particles are attracted by the wall, it is favorable for the system to increase their density close to the wall. However, due to the hard core nature of the particles and the equality of the interparticle attraction for all pairs of particles, the increase of solvent particles leads to an extrusion of ionic particles, leading to decreased ion densities at the wall. However, the density deviations of the ions are much weaker. For the remaining relevant parameters see Sec. 3.3.1.

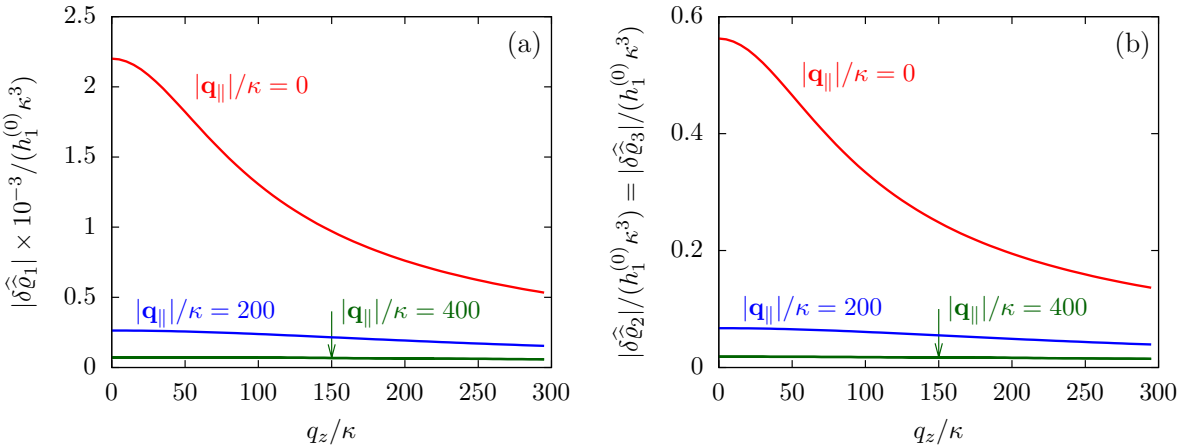

Figure 3.4: Density profiles of the solvent (panel (a)) and of the ions (panel (b)) as functions of the wave number q_z in normal direction (with $h_1^{(0)}\kappa^3$ being dimensionless) in corresponding units of the Debye length $1/\kappa$ (see Eq. (3.34)). Note that due to $\delta\widehat{\widehat{\varrho}}_i \in \mathbb{C}$, the absolute values are shown. In each graph, there are three profiles shown corresponding to three values of the other relevant variable. Therefore, the profiles correspond to cuts through Figs. 3.2 (a) and (b) at various positions and in different directions. In this case the boundary condition is $\boldsymbol{v}' = -\frac{h_1^{(0)}}{b}(1,0,0,0)$ (see Eqs. (3.15) and (3.40)), corresponding to a δ-like nonelectrostatic attraction of the solvent particles at the origin of the wall (see Fig. 3.2 and Eq. (3.42)). The graphs show, that the density deviations of the ions are proportional to the ones of the solvent. Since only the solvent particles are attracted by the wall, it is favorable for the system to increase their density close to the wall. However, due to the hard core nature of the particles and the equality of the interparticle attraction for all pairs of particles, the increase of solvent particles leads to an extrusion of ionic particles, leading to decreased ion densities at the wall. However, the density deviations of the ions are much weaker. For the remaining relevant parameters see Sec. 3.3.1.

real space increases with increasing distance from the wall. This implies that the density distribution broadens upon moving away from the source of the perturbation. The curves in Figs. 3.4 (a) and (b) exhibit widths of half height which increase with the lateral wave number $|\boldsymbol{q}_\parallel|$, i.e., the normal decay length in real space decreases with increasing lateral wave number. Consequently, the range of influence of rapidly varying modes of wall heterogeneities onto the fluid is shorter than that of slowly varying modes. This relationship can also be inferred from Figs. 3.3 (a) and (b). From the above discussions and from Figs. 3.3 and 3.4 one can conclude, that the response of all species to a simple attraction of nonelectrostatic type is the same up to a proportionality factor. This is confirmed by studying, in addition, the boundary conditions $\boldsymbol{v}' = -\frac{h_2^{(0)}}{b}(0,1,0,0)$ and $\boldsymbol{v}' = -\frac{h_3^{(0)}}{b}(0,0,1,0)$; these results are not shown here.

After having discussed the effects of the boundary condition $\widehat{\boldsymbol{h}} \neq 0$ via Figs. 3.2 and 3.3, the following second type of boundary condition is analyzed:

$$\begin{aligned} \widehat{\boldsymbol{h}}(\boldsymbol{q}_\parallel) &= \boldsymbol{0}, \\ \widehat{\sigma}(\boldsymbol{q}_\parallel) = \sigma^{(0)},\ \text{i.e.,}\ \sigma(\boldsymbol{r}_\parallel) &= \sigma^{(0)}\ \delta(\boldsymbol{r}_\parallel), \end{aligned} \tag{3.43}$$

leading to

$$\boldsymbol{v}'(\boldsymbol{q}_\parallel, 0) = -\frac{\beta e \sigma^{(0)}}{\varepsilon_0 \varepsilon_r}(0,0,0,1). \tag{3.44}$$

As before, the physical realization of this boundary condition is a δ-like interaction, with the only difference residing in the type of the basic interaction. Unlike in the previous case, here the interaction is of electrostatic character. Thus, the situation corresponds to a δ-like negative charge distribution placed at the origin of the wall. Since the two ion types respond oppositely, the ion density profiles differ only in sign:

$$\delta\widehat{\varrho}_2 = -\delta\widehat{\varrho}_3. \tag{3.45}$$

This implies that the total ion density deviations vanish $\delta\widehat{\varrho}_2 + \delta\widehat{\varrho}_3 = 0$. Accordingly, also the density deviation for the solvent vanishes, i.e., $\delta\widehat{\varrho}_1 = 0$. Figure 3.5 shows the density profiles of the positive ions, which, up to the sign, are the same as the ones for the negative ions. As stated above, for this boundary condition, there is no need to discuss the behavior of the solvent particles.

The three panels in Fig. 3.5 are obtained similarly as the ones in Figs. 3.3 and 3.4. Figure 3.5 (a) shows the density profiles $\delta\widehat{\varrho}_2(\boldsymbol{q}_\parallel, z)$ as functions of the normal distance z from the wall for three values of the lateral wave number $|\boldsymbol{q}_\parallel|$. Panel 3.5 (b) shows the same density profiles $\delta\widehat{\varrho}_2(\boldsymbol{q}_\parallel, z)$ but as functions of $|\boldsymbol{q}_\parallel|$ for three distances z from the

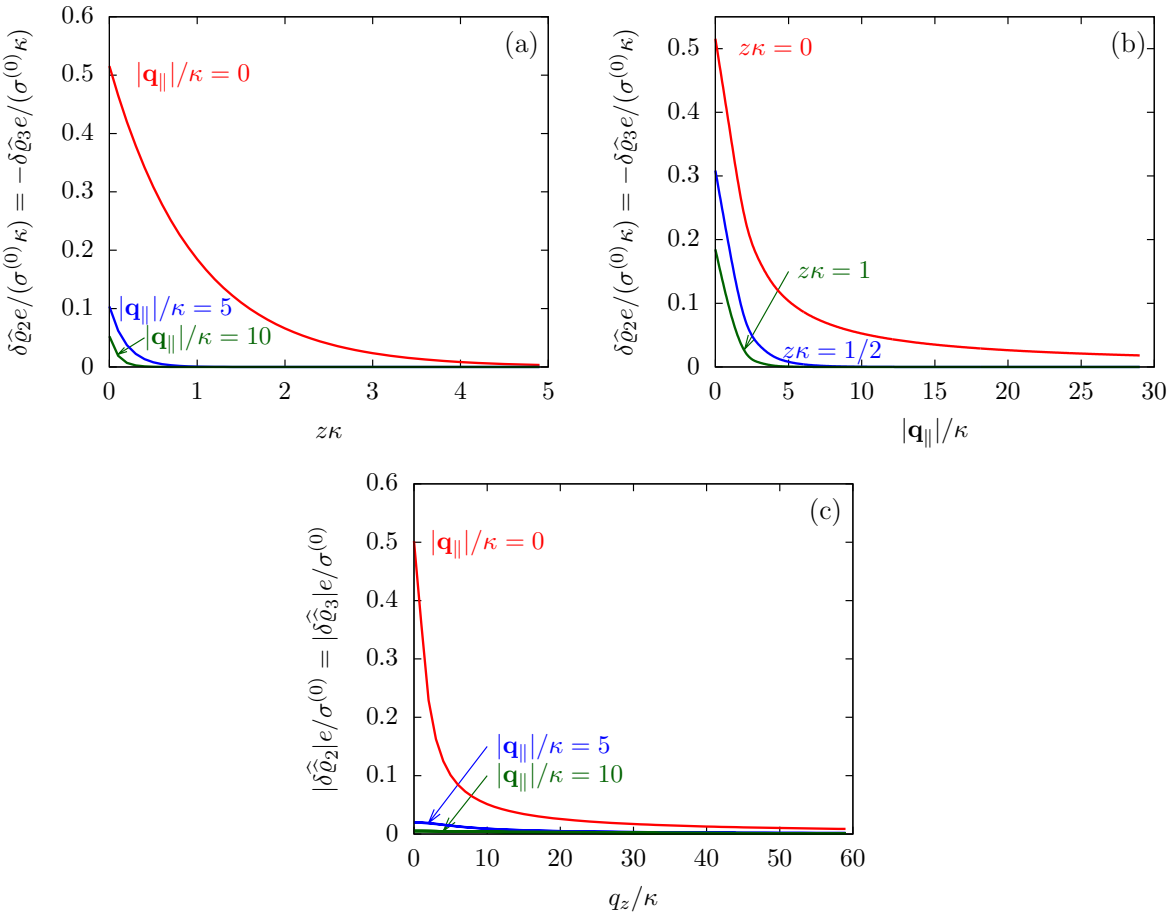

Figure 3.5: Density profiles of the ions as functions of the normal distance from the wall (a), of the absolute value of the lateral wave vector $|\boldsymbol{q}_\parallel|$ (b), and of the wave number in normal direction (c). Note that due to $\delta\widehat{\widehat{\varrho}}_i \in \mathbb{C}$, in panel (c) the absolute value is shown. Each panel shows the profiles for three values of the other relevant variable. These profiles are cuts of the corresponding data (analogous to Fig. 3.2) along various directions. Here, the boundary condition is given by $\boldsymbol{v}' = -\frac{\beta e \sigma^{(0)}}{\varepsilon_0 \varepsilon_r}(0,0,0,1)$ (see Eqs. (3.15) and (3.44)), which corresponds to a δ-like surface charge at the origin in real space (see Eq. (3.43)). The profiles for the solvent are not shown, because the deviations linked to the two types of ions cancel out, $\delta\widehat{\varrho}_2 + \delta\widehat{\varrho}_3 = 0$, leaving the density of the solvent unchanged as if there were no ions. In comparison with Fig. 3.3, the profiles in (a) decay much slower on the scale of the Debye length $1/\kappa$ (see Eq. (3.34)) instead of on the scale of the much shorter bulk correlation length ξ (see Fig. 3.3 (b) and Eq. (3.36)) due to the nonelectrostatic interaction. Accordingly, the profiles in (b) and (c) decay on the scale of κ more rapidly than their counterparts in Figs. 3.3 (d) and 3.4 (b). For the remaining relevant parameters see Sec. 3.3.1.

wall. Figure 3.5 (c) displays the double Fourier transform $\delta\widehat{\widehat{\varrho}}_2(\boldsymbol{q}_\parallel, q_z)$. Compared with the profiles in Figs. 3.3 and 3.4 for the previously discussed boundary conditions, all present profiles differ significantly from them. Figure 3.5 (a) reveals a much larger decay length in z-direction, i.e., normal to the wall. Also in Fourier space the decay in lateral direction occurs much more rapidly, i.e., on much longer length scales in real space than in the case of the nonelectrostatic wall-fluid interaction (cf. Fig. 3.3). This is indicated by the much narrower peak in the double Fourier transform (see Fig. 3.5 (c)). Furthermore, Fig. 3.5 (a) shows a variation of the decay length in normal direction as function of $|\boldsymbol{q}_\parallel|$. In Fig. 3.5 (b) one observes that the lateral wave numbers $|\boldsymbol{q}_\parallel|$ at which the profiles $\delta\widehat{\varrho}_2 = -\delta\widehat{\varrho}_3$ decay to half of the maximum values decrease upon increasing the distances z from the wall, from which one infers that the lateral decay length in real space increases upon increasing z. The decay with respect to $|\boldsymbol{q}_\parallel|$ is much faster than in the previous case (compare Fig. 3.3 (d)), indicating that in real space there is a slower decay in the lateral direction. Moreover, in Figs. 3.5 (b) and 3.5 (c) the functional form differs from the one shown in Figs. 3.2, 3.3, and 3.4. These differences naturally occur due to the different form of the boundary condition. Since in the case of the boundary condition studied above (see Figs. 3.2, 3.3, and 3.4) the relevant interaction is nonelectrostatic, the length scale dominating the decay is given by the corresponding short-ranged bulk correlation length ξ (see Eq. (3.36)). In contrast, for the system shown in Fig. 3.5, due to the electrostatic nature of the corresponding interaction, the dominating length scale is the Debye length $1/\kappa$ (see Eq. (3.34)). This length is much larger than the correlation length ξ due to the nonelectrostatic interaction, giving rise to the much slower decay in Fig. 3.5 (a) (on the scale of $1/\kappa$) and the much faster decay in Figs. 3.5 (b) and (c) (on the scale of κ).

3.3.4 Circular patch of interaction

Having discussed actually point-like interactions between the wall and the fluid in Sec. 3.3.3, as the next step I now study the influence of interaction patterns on the density deviations close to a wall upon broadening the spatial extent of the interaction area. To this end I analyze the influence of a two-dimensional circular interaction patch of radius R centered at the origin (see Fig. 3.6 (a)).

Due to the radial symmetry, the spatial structures in Fourier space depend only on the absolute value $|\boldsymbol{q}_\parallel|$ of the lateral wave vector $\boldsymbol{q}_\parallel$. Figure 3.7 discusses four distinct configurations.

Alluding to the insights gained in the previous section, Figs. 3.7 (a) and (c) correspond to a homogeneous circular patch of radius R, which interacts with the solvent only, similar

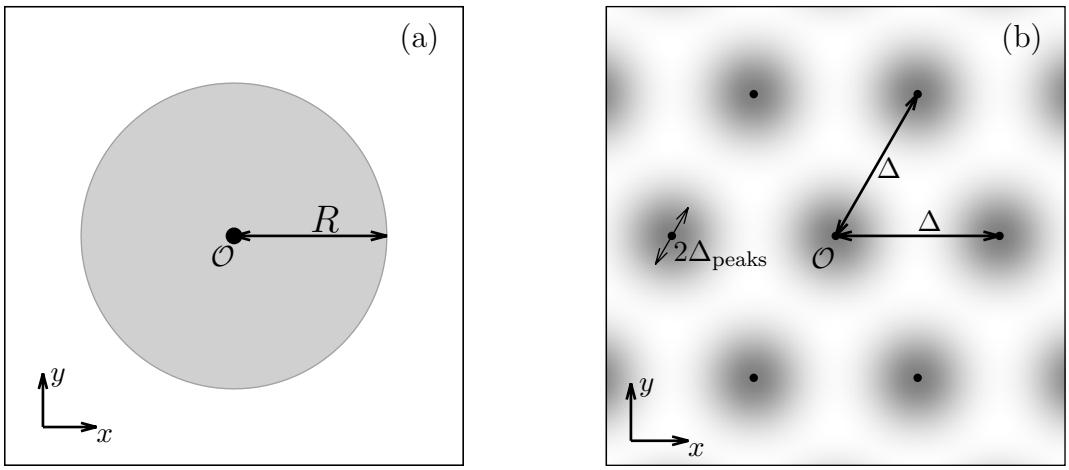

Figure 3.6: Physical configurations studied in Sec. 3.3.4 (a) and in Sec. 3.3.5 (b). In Sec. 3.3.4, a two-dimensional circular patch of radius R centered at the origin is studied (a). The dots in panel (b) correspond to the positions of the centers of the Gaussian interaction sites for the model used in Sec. 3.3.5, which form a two-dimensional hexagonal lattice with lattice constant Δ. The variance of the Gauss distributions is Δ^2_{peaks} (Eqs. (3.52) and (3.53)). The results shown here are based on the choice $\Delta = 5\Delta_{\text{peaks}}$ (cf. Fig. 3.8).

to Figs. 3.2, 3.3, and 3.4. This amounts to the boundary condition (see Eq. (3.15))

$$\begin{aligned} h_1(\boldsymbol{r}_\parallel) &= \bar{h}_1^{(0)}\ \Theta(R - |\boldsymbol{r}|), \\ h_2(\boldsymbol{r}_\parallel) &= h_3(\boldsymbol{r}_\parallel) = \sigma(\boldsymbol{r}_\parallel) = 0 \end{aligned} \tag{3.46}$$

leading to

$$\boldsymbol{v}'(\boldsymbol{q}_\parallel, 0) = -2\pi R^2 \frac{\bar{h}_1^{(0)}}{b} \frac{J_1(|\boldsymbol{q}_\parallel|R)}{|\boldsymbol{q}_\parallel|R}\ (1,0,0,0), \tag{3.47}$$

where the two-dimensional Fourier transform of the Heaviside function $\Theta(R-|\boldsymbol{r}|)$ is given by

$$\int_{\mathbb{R}^2} \mathrm{d}^2 r_\parallel\ \Theta(R - |\boldsymbol{r}_\parallel|) \exp(-i\boldsymbol{q}_\parallel \cdot \boldsymbol{r}_\parallel) = 2\pi R^2 \frac{J_1(|\boldsymbol{q}_\parallel|R)}{|\boldsymbol{q}_\parallel|R}. \tag{3.48}$$

In contrast, Figs. 3.7 (b) and (d) refer to a charged circular patch of radius R, similar to Fig. 3.5:

$$\boldsymbol{h}(\boldsymbol{r}_\parallel) = 0,\ \sigma(\boldsymbol{r}_\parallel) = \bar{\sigma}^{(0)}\Theta(R - |\boldsymbol{r}_\parallel|), \tag{3.49}$$

leading to the boundary condition

$$\boldsymbol{v}'(\boldsymbol{q}_\parallel, 0) = -2\pi R^2 \frac{\beta e \bar{\sigma}^{(0)}}{\varepsilon_0 \varepsilon_r} \frac{J_1(|\boldsymbol{q}_\parallel|R)}{|\boldsymbol{q}_\parallel|R}\ (0,0,0,1). \tag{3.50}$$

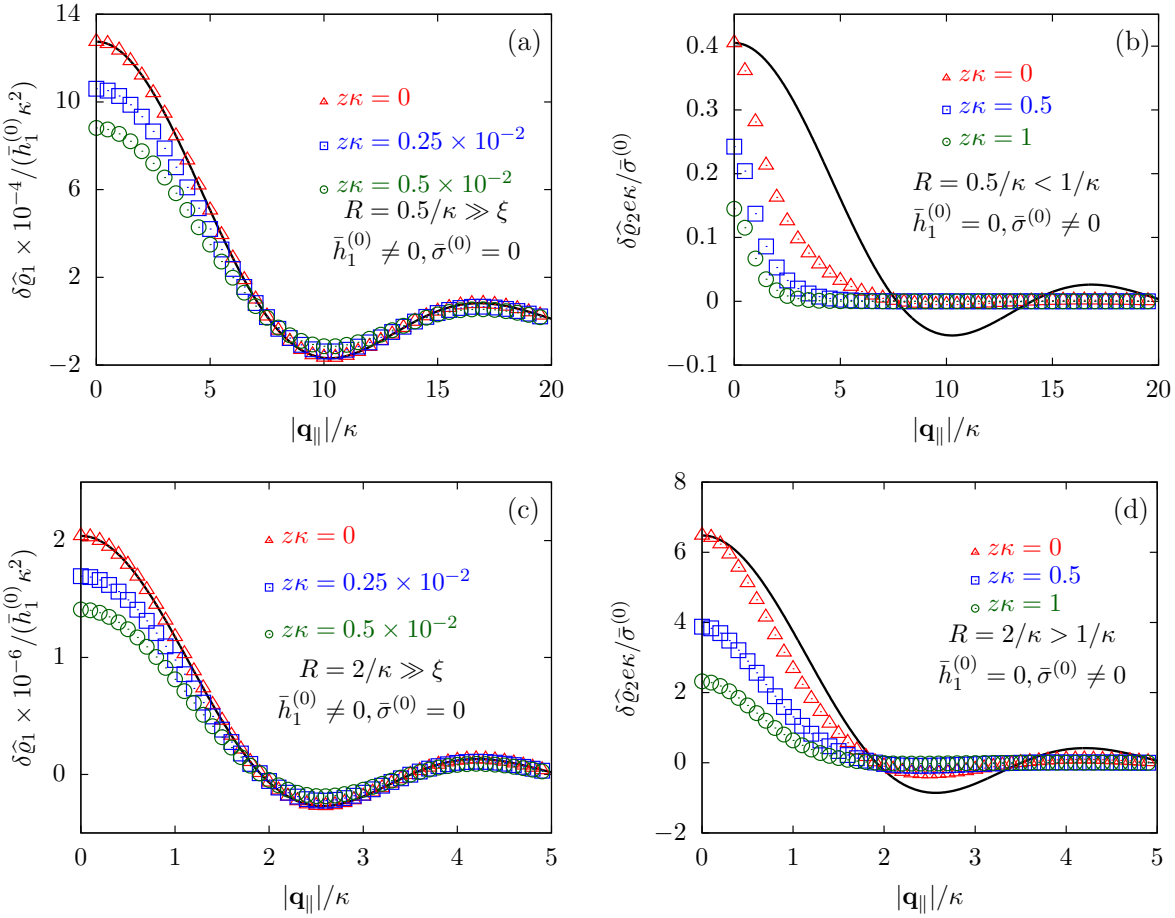

Figure 3.7: Density profiles of the solvent (panels (a) and (c)) and of the ions (panels (b) and (d)) as functions of the absolute value $|\boldsymbol{q}_\parallel|$ of the lateral wave vector for three normal distances z from the wall. The boundary condition corresponds to a circular interaction patch centered at the origin with radius $R > 0$. In the panels (a) and (b) the radius of the patch is $R = 0.5/\kappa$, whereas in the panels (c) and (d) the radius is $R = 2/\kappa$, where $1/\kappa$ is the Debye length (see Eq. (3.34)). All considered patch radii are much larger than the bulk correlation length, $R \gg \xi$ (see Eq. (3.36)). In addition, there are different types of interaction. In panels (a) and (c) the interaction between the wall and the solvent particles is nonelectrostatic ($h_1(\boldsymbol{r}_\parallel) = \bar{h}_1^{(0)}\Theta(R - |\boldsymbol{r}_\parallel|), h_2(\boldsymbol{r}_\parallel) = h_3(\boldsymbol{r}_\parallel) = \sigma(\boldsymbol{r}_\parallel) = 0$, see Eq. (3.46) as well as Figs. 3.2, 3.3 and 3.4), whereas in panels (b) and (d) the patch contains a constant surface charge and therefore interacts with the ions only ($\boldsymbol{h}(\boldsymbol{r}_\parallel) = 0, \sigma(\boldsymbol{r}_\parallel) = \bar{\sigma}^{(0)}\Theta(R - |\boldsymbol{r}_\parallel|)$, see Eq. (3.49) and Fig. 3.5). Besides the profiles, all panels show also the lateral Fourier transform of the boundary condition (Eqs. (3.47) and (3.50)) displayed as a black solid line. In the case of the interaction of the wall with the solvent ((a) and (c)), the decay of the profiles as function of $|\boldsymbol{q}_\parallel|$ is proportional to the lateral Fourier transform of the boundary condition, which implies, that the density deviations in real space closely follow the shape of the patch. However, in the case of a charged patch at the surface the density distribution of the ions reflects the competition between the length scale R of the radius of the patch and the Debye length $1/\kappa$. In the case of small patches ($R < 1/\kappa$, panel (b)), the Debye length dominates and therefore dictates the decay as function of $|\boldsymbol{q}_\parallel|$ without noticeable influence of the patch. (cont.)

Continued Figure 3.7: In contrast, in the case of large patches ($R > 1/\kappa$, panel (d)), in which the radius of the patch is the dominating length scale, the shape of the profiles follows the Fourier transform of the charge distribution at the wall, i.e., the patch of radius R. For the remaining relevant parameters see Sec. 3.3.1.

Figures 3.7 (a) and (b) correspond to the patch size $R = 0.5/\kappa$ whereas Figs. 3.7 (c) and (d) correspond to $R = 2/\kappa$. In all four panels the black line is given by $AJ_1(|\boldsymbol{q}_\parallel|R)/(|\boldsymbol{q}_\parallel|R)$ with A chosen such that the first maximum of the data for $z\kappa = 0$ is reproduced. In Figs. 3.7 (a) and (c) only the solvent density profiles are shown, because, due to linearity, Sec. 3.3.3 indicates, that the ion profiles are proportional to the one of the solvent. Figures 3.7 (a) and (c) clearly show, that the density deviations are proportional to the Fourier transform $\boldsymbol{v}'(\boldsymbol{q}_\parallel, 0)$ of the boundary condition (Eq. (3.47), solid black line). This implies that for increasing lateral distances from the center of the patch the decay of the profiles in real space is dominated by the length scale set by the radius R of the patch. This trend holds for both patch sizes. However, as expected, the amplitudes of the density deviations increase for the larger patch size (note the different scales). In contrast, in Figs. 3.7 (b) and (d), where the density profiles of the positive ions are shown and where the profiles for the solvent are omitted for the same reasons as explained in Sec. 3.3.3, the profiles do not follow the Fourier transform of the boundary conditions (solid black line). This is particularly pronounced in Fig. 3.7 (b), i.e., for the smaller patch size. In this case, the decay as function of $|\boldsymbol{q}_\parallel|$ is faster than the Fourier transform of the boundary condition, which implies that the profiles decay on a length scale larger than that of the radius R of the patch and also the shape of the decay differs from that of the expression $J_1(|\boldsymbol{q}_\parallel|R)/(|\boldsymbol{q}_\parallel|R)$. This behavior can be understood in terms of two distinct dominating length scales. In Figs. 3.7 (b) and (d), where the effect of electrostatic interactions are shown, the dominating internal length scale is the Debye length $1/\kappa$ in contrast to the much smaller correlation length ξ ($\xi \approx 1.3 \times 10^{-2}\ \kappa^{-1}$) induced by the nonelectrostatic interactions characterizing Figs. 3.7 (a) and (c). Since in Fig. 3.7 (b) the radius R of the patch is only half the Debye length $1/\kappa$, the overall dominating length scale is the Debye length $1/\kappa$, so that the density deviations decay in real space on a length scale which is larger than the patch radius R. Also, since the profile in Fourier space is not proportional to the Fourier transform of the boundary condition, one can conclude that the shape of the patch has no significant influence on the decay behavior. The competition of the length scales ξ, $1/\kappa$, and R is also borne out in Fig. 3.7 (d), where the patch size R is twice as large as the Debye length $1/\kappa$. This case is much more similar to the situations discussed in Figs. 3.7 (a) and (c), because the overall dominating length scale is set by the radius R, and consequently the profiles follow rather closely the shape (solid black line)

dictated by the interaction patch. However, the influence of the smaller Debye length scale is still visible, which is the reason for the deviations from the Fourier transform of the boundary condition (solid black line). In conclusion, as already seen in Sec. 3.3.3, the largest length scale sets the decay behavior of the density deviations. In the present case of nonvanishing sizes of the interaction areas, the largest length scale dictates not only the range but also the shape of the density deviations.

3.3.5 Periodic distribution of interaction sites

After having discussed the density profiles in the presence of spatially localized, single interaction sites in Secs. 3.3.3 and 3.3.4, here I study the influence of interaction sites forming a regular hexagonal lattice:

$$\boldsymbol{r}_{\text{peaks}} = (m\Delta + \frac{n}{2}\Delta, \frac{\sqrt{3}}{2}n\Delta), \quad m, n \in \mathbb{Z}, \tag{3.51}$$

see Fig. 3.6 (b); the distance between nearest neighbor sites is denoted as Δ.

Distinct from the previous examples in Secs. 3.3.3 and 3.3.4, the interaction strength around the individual interaction sites $\boldsymbol{r}_{\text{peaks}}$ is taken to form a Gaussian distribution, providing either a nonelectrostatic or an electrostatic interaction with equal amplitudes for all interaction sites:

$$h_i(\boldsymbol{r}) = \bar{h}_i^{(0)} \sum_{\text{peaks}} \exp\left(-\frac{(\boldsymbol{r} - \boldsymbol{r}_{\text{peaks}})^2}{2\Delta_{\text{peaks}}^2}\right), \quad i = 1, 2, 3, \tag{3.52}$$

and

$$\sigma(\boldsymbol{r}) = \bar{\sigma}^{(0)} \sum_{\text{peaks}} \exp\left(-\frac{(\boldsymbol{r} - \boldsymbol{r}_{\text{peaks}})^2}{2\Delta_{\text{peaks}}^2}\right), \tag{3.53}$$

respectively, where Δ_{peaks}^2 is the variance of the Gaussian interaction. Lateral Fourier transformation leads to the corresponding boundary condition $\boldsymbol{v}'$ (see Eq. (3.15)) with

$$v_i'(\boldsymbol{q}_\parallel) = -\frac{\bar{h}_i^{(0)}}{b}(2\pi\Delta_{\text{peaks}}^2)\exp\left(-\frac{{\boldsymbol{q}_\parallel}^2\Delta_{\text{peaks}}^2}{2}\right)|\mathcal{C}_\mathcal{G}|\times \sum_{\boldsymbol{G}\in\mathcal{G}}\delta(\boldsymbol{q}_\parallel - \boldsymbol{G}), \quad i = 1, 2, 3, \tag{3.54}$$

and

$$v_4'(\boldsymbol{q}_\parallel) = -\frac{\beta e\bar{\sigma}^{(0)}}{\varepsilon_0\varepsilon_r}(2\pi\Delta_{\text{peaks}}^2)\exp\left(-\frac{{\boldsymbol{q}_\parallel}^2\Delta_{\text{peaks}}^2}{2}\right)|\mathcal{C}_\mathcal{G}|\times \sum_{\boldsymbol{G}\in\mathcal{G}}\delta(\boldsymbol{q}_\parallel-\boldsymbol{G}), \tag{3.55}$$

where $|\mathcal{C}_\mathcal{G}| = (16\pi^2/(3\Delta^2))\sin(60°)$ is the size of an elementary cell of the corresponding two-dimensional reciprocal lattice $\mathcal{G}$. Using this boundary condition, I have studied four different systems, as shown in Fig. 3.8.

The four panels are arranged as in Fig. 3.7, with the boundary conditions in Figs. 3.8 (a) and (c) corresponding to a chemical interaction between the wall and solvent only,

$$\boldsymbol{v}'(\boldsymbol{q}_\parallel) = -\frac{\bar{h}_1^{(0)}}{b}(2\pi\Delta_{\text{peaks}}^2)\exp\left(-\frac{{\boldsymbol{q}_\parallel}^2\Delta_{\text{peaks}}^2}{2}\right)|\mathcal{C}_\mathcal{G}|\times \sum_{\boldsymbol{G}\in\mathcal{G}}\delta(\boldsymbol{q}_\parallel-\boldsymbol{G})\ (1,0,0,0), \tag{3.56}$$

whereas the boundary conditions in Figs. 3.8 (b) and (d) correspond to an interaction between the wall and ions only, i.e., they are due to a hexagonal lattice of interaction sites with Gaussian intrinsic charge distribution:

$$\boldsymbol{v}'(\boldsymbol{q}_\parallel) = \frac{\beta e\bar{\sigma}^{(0)}}{\varepsilon_0\varepsilon_r}(2\pi\Delta_{\text{peaks}}^2)\exp\left(-\frac{{\boldsymbol{q}_\parallel}^2\Delta_{\text{peaks}}^2}{2}\right)|\mathcal{C}_\mathcal{G}|\times \sum_{\boldsymbol{G}\in\mathcal{G}}\delta(\boldsymbol{q}_\parallel-\boldsymbol{G})\ (0,0,0,1). \tag{3.57}$$

For the same reason as stated in the context of Fig. 3.7, in the former case (Figs. 3.8 (a) and (c)) only the deviations of the solvent density and in the latter case (Figs. 3.8 (b) and (d)) only the deviations of the ion densities are shown. Figures 3.8 (a) and (b) correspond to the lattice constant $\Delta = 0.5/\kappa$, whereas Figs. 3.8 (c) and (d) correspond to $\Delta = 2/\kappa$. The variance Δ_{peaks}^2 of the peaks is taken as $\Delta_{\text{peaks}} = \Delta/5$, so that $\Delta_{\text{peaks}} = 0.1/\kappa$ in Figs. 3.8 (a) and (b) and $\Delta_{\text{peaks}} = 0.4/\kappa$ in Figs. 3.8 (c) and (d). Figures 3.8 (a) and (c) tell that, although different values for $\boldsymbol{q}_\parallel$ change the amplitude of the profiles in all cases, the solvent profile decays exponentially, upon increasing the normal distance z from the wall, on the scale of the bulk correlation length ξ. This holds for both values of the lattice constant Δ. However, the amplitude of the density deviations is slightly increased for the larger lattice constant Δ, which is in line with the also increased variance Δ_{peak}^2 of the interaction sites. In contrast to these findings, Figs. 3.8 (b) and (d) reveal a different picture. In these panels, one still finds an exponential decay of the profiles upon increasing

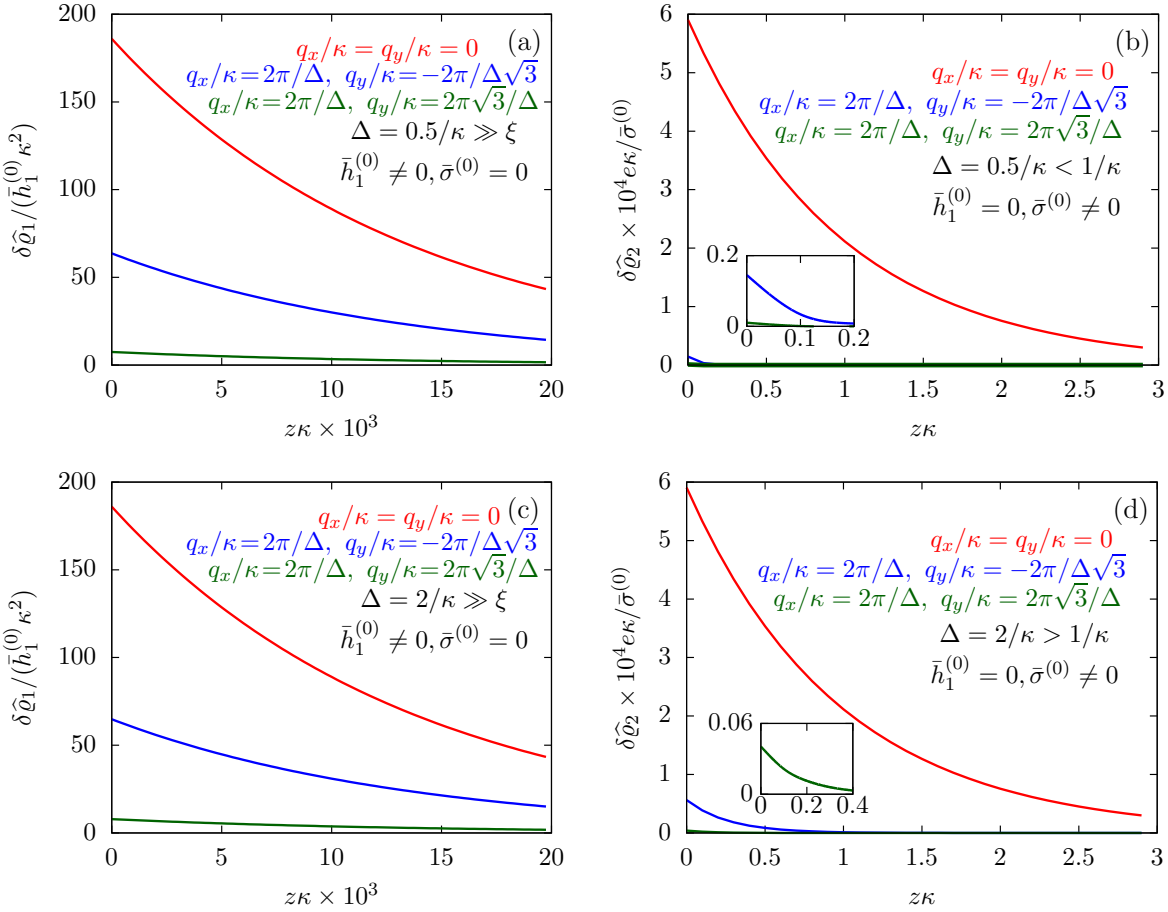

Figure 3.8: Density profiles of the solvent (panels (a) and (c)) and of the ions (panels (b) and (d)) for three lateral wave vectors $\boldsymbol{q}_\parallel = (q_x, q_y)$ as functions of the normal distance z from the wall in units of the Debye length $1/\kappa$. The boundary condition corresponds to a hexagonal lattice of interaction sites with a Gaussian distribution of the interaction strength characterized by a standard deviation $\Delta_{\text{peaks}} = \Delta/5$. The lattice constant is denoted as Δ (see Fig. 3.6). In panels (a) and (b) the lattice constant and the variance are $\Delta = 0.5/\kappa$ and $\Delta_{\text{peaks}} = 0.1/\kappa$, respectively, whereas in panels (c) and (d) the lattice constant and the variance are $\Delta = 2/\kappa$ and $\Delta_{\text{peaks}} = 0.4/\kappa$, respectively, with the Debye length $1/\kappa$ (see Eq. (3.34)). Panels (a) and (c) correspond to systems with a nonelectrostatic interaction between the wall and the solvent particles (see Eq. (3.56)), whereas panels (b) and (d) correspond to systems with electrostatic interaction sites between wall and ions (see Eq. (3.57)). The insets in (b) and (d) show a magnified version of the respective profiles in the main plot. In all cases, the profiles decay exponentially upon increasing the normal distance z from the wall. However, the decay length differs significantly between the two aforementioned types of interactions. In the case of the nonelectrostatic interaction, the decay length is set by the bulk correlation length ξ (see Eq. (3.36)) of the fluid, whereas in the case of the electrostatic interaction it is set by the much larger Debye length $1/\kappa$. This difference in the decay lengths, both in lateral and in normal direction, which leads to a much faster lateral decay in the case of the electrostatic interactions, is also responsible for the decreasing amplitude of the ion profiles for increased wave vectors (panel (b) and (d)). (cont.)

Continued Figure 3.8: Another significant difference between the two interaction types is the variation of the decay length as function of the lateral wave vectors. In panels (a) and (c) all profiles decay exponentially on the same decay length ξ, whereas in panels (b) and (d) the decay length depends significantly on the wave vectors. This effect follows from the dependence of the eigenvalues on $|\boldsymbol{q}_{\parallel}|$ as discussed in Eq. (3.60), corresponding to a lateral decay proportional to $\exp(-\sqrt{\kappa^2 + |\boldsymbol{q}_{\parallel}|^2}z)$. In principle this occurs for both types of interactions. However, only in the case of the electrostatic interactions it is relevant, which again is due to the difference between the dominating length scales. For the remaining relevant parameters see Sec. 3.3.1.

the normal distance z. However, the profiles decay on a much larger length scale than the ones in Figs. 3.8 (a) and (c). Moreover, not only the amplitude but also the decay length changes significantly for different values of $\boldsymbol{q}_{\parallel}$. This was already encountered in Fig. 3.5, where the decay length depends on the value of $|\boldsymbol{q}_{\parallel}|$. This variation of the decay lengths can be inferred from Eq. (3.14), which shows that the eigenvalues and thus the decay length depends on $k = |\boldsymbol{q}_{\parallel}|$. The variation of the decay length can be expressed in terms of the Debye length $1/\kappa$, which determines the length scale in case of $|\boldsymbol{q}_{\parallel}| = 0$. From Eq. (3.60) one finds, that the decay as function of z is proportional to $\exp(-\sqrt{\kappa^2 + |\boldsymbol{q}_{\parallel}|^2}z)$. The large differences in the amplitudes of the various profiles in Figs. 3.8 (b) and (d), as well as the pronounced increase of the decay length in comparison to Figs. 3.8 (a) and (c) can be understood in terms of the differences between the dominating length scale. Analogous to the previous sections, for the systems shown in Figs. 3.8 (a) and (c), the dominating length scale in lateral direction is the length scale set by the boundary conditions and the bulk correlation length ξ, which characterizes the decay of the solvent density in normal direction. However, for the systems shown in Figs. 3.8 (b) and (d), the relevant inherent length scale of the fluid is the Debye length $1/\kappa$, which is significantly larger than the bulk correlation length ξ and thus causes the increase in the length scale of the decay, both in lateral and in normal direction.

3.4 Conclusions and summary

In the present analysis the influence of a chemically or electrostatically structured surface on an adjacent fluid has been studied and described in terms of the number density profiles of the fluid components. The fluid, which comprises a single solvent species and a single univalent salt far away from bulk and wetting phase transitions, has been investigated within classical density functional theory [46, 57, 121]. Within this model four examples of heterogeneous walls have been studied. First, single isolated interaction

sites are discussed, which interact either nonelectrostatically (between the wall and solvent particles) or electrostatically (between the wall and ions) (see Secs. 3.3.3 and 3.3.4). In the case of a δ-like nonelectrostatic interaction, the solvent density increases around the interaction site and decays exponentially on the length scale of the bulk correlation length ξ. The deviations of the ion number densities from their bulk values are proportional to that of the number density of the solvent (see Figs. 3.2, 3.3, and 3.4). For a δ-like electrostatic interaction, within the present model, the solvent does not respond at all, because the deviations induced by the two ion types even out due to symmetries, whereas the density deviations of the ionic particles again decay exponentially. However, the length scale of the latter decay is significantly increased as compared to the former case, because the dominating scale in this case is the Debye length $1/\kappa \gg \xi$ (see Fig. 3.5). The introduction of another length scale by studying interaction sites of nonvanishing extent (see Sec. 3.3.4) shows, that the resulting density profiles strongly depend on the dominant length scale (see Fig. 3.7). If a bulk length scale (bulk correlation length ξ or Debye length $1/\kappa$) dominates, the profiles resemble the ones for δ-like interactions. However, if a length scale set by a boundary condition at the wall dominates or is similar to the dominating length scale in the bulk, the decay of the density deviations increasingly reflects the boundary conditions. Finally, the examination of multiple interaction sites, arranged as a regular hexagonal lattice (see Fig. 3.6 (b)), shows, that the size of the interaction sites and the distance between them influence the amplitude and thus the importance of density deviations for large values of the lateral wave number $|\boldsymbol{q}_{\parallel}|$ (see Fig. 3.8).

In summary, the present study provides a flexible framework to determine the influence of various surface inhomogeneities on the density profiles of a fluid in contact with that substrate. The resulting profiles are found to be sensitive to the type of interaction as well as to the size and the distribution of the interaction sites.

This framework is considered as a starting point for extensions into various directions, aiming for the analysis of more sophisticated and realistic models. First, the model used here to describe the fluid is a very simple one, chosen to lay a foundation for further research and to introduce the approach as such. Concerning future work, more realistic descriptions of the fluid and more elaborate density functional descriptions could be used. For instance, the present restriction to low ionic strengths and equal particle sizes can be removed along the lines of Ref. [145]. Another way of using more precise density functional descriptions is the one used in the following Chap. 4, where fundamental measure theory is used to account for finite sizes of the described particles. Second, for the systems studied here, the fluid is thermodynamically far from any bulk or wetting phase transitions. This is solely done for the sake of simplicity. In future studies of more realistic systems, taking into

account the occurrence of phase transitions and their influence on the systems is expected to be rewarding. Third, this study is restricted to linear response theory. Whereas this allows for a broad overview of structure formation in terms of superpositions of only a few elementary patterns, the occurrence of nonlinear structure formation phenomena requires approaches beyond linear response theory. Again, this limitation is lifted in the research presented in Chap. 4. Finally, studying the influence of disordered surface structures within the present framework appears to be very promising.

3.A Eigenvectors and eigenvalues of $\underline{\underline{\boldsymbol{H}}}(k)$

According to the structure of the matrix $\underline{\underline{\boldsymbol{M}}}$ (Eq. (3.2)), with entries given by Eq. (3.30), and of the vector $\boldsymbol{Z} = (0, 1, -1)$, from Eqs. (3.9) and (3.10) one infers that the matrix $\underline{\underline{\boldsymbol{H}}}(k)$ has the form

$$\underline{\underline{\boldsymbol{H}}}(k) = \begin{pmatrix} s & u & u & 0 \\ u & t & u & iv \\ u & u & t & -iv \\ 0 & iv & -iv & 0 \end{pmatrix} + \mathrm{diag}(k^2) \tag{3.58}$$

with $s, t, u, v \in \mathbb{R}$ and $k = |\boldsymbol{q}_{\|}|$, $s, t > 0$. It can be readily verified that the four vectors

$$\begin{aligned} \boldsymbol{\Lambda}_1(k) &:= (2u, \lambda_1(k) - s, \lambda_1(k) - s, 0), \\ \boldsymbol{\Lambda}_2(k) &:= (\lambda_2(k) - t - u, u, u, 0), \\ \boldsymbol{\Lambda}_3(k) &:= (0, \lambda_3(k), -\lambda_3(k), 2iv), \\ \boldsymbol{\Lambda}_4(k) &:= (0, iv, -iv, \lambda_4(k) - t + u) \end{aligned} \tag{3.59}$$

with $\boldsymbol{\Lambda}_i \in \mathbb{C}^4$ for $i = 1, \ldots, 4$, form a *nonorthogonal* basis of eigenvectors of the matrix $\underline{\underline{\boldsymbol{H}}}(k)$ in Eq. (3.58) with the respective real eigenvalues

$$\begin{aligned} \lambda_1(k) &= \frac{1}{2}\left(s + t + u + \sqrt{(s - t - u)^2 + 8u^2}\right) + k^2, \\ \lambda_2(k) &= \frac{1}{2}\left(s + t + u - \sqrt{(s - t - u)^2 + 8u^2}\right) + k^2, \\ \lambda_3(k) &= \frac{1}{2}\left(t - u + \sqrt{(t - u)^2 - 8v^2}\right) + k^2, \\ \lambda_4(k) &= \frac{1}{2}\left(t - u - \sqrt{(t - u)^2 - 8v^2}\right) + k^2. \end{aligned} \tag{3.60}$$

The expressions for $s, t, u,$ and v can be obtained from the bulk quantities mentioned

in Sec. 3.3.1 and take on the forms (see Eqs. (3.25) and (3.30))

$$s = \frac{M_{11}}{b}, \tag{3.61}$$

$$t = \frac{M_{22}}{b} = \frac{M_{33}}{b}, \tag{3.62}$$

$$u = \frac{M_{12}}{b} = \frac{M_{13}}{b} = \frac{M_{23}}{b}, \tag{3.63}$$

$$v = -\sqrt{\frac{4\pi l_B}{b}}. \tag{3.64}$$

Chapter 4

Hard sphere electrolyte solution using fundamental measure theory

Building on the results of the previous Chap. 3, this chapter deals with investigating the structure of dilute electrolyte solutions close to a surface carrying a spatially inhomogeneous surface charge distribution by means of classical density functional theory (DFT) within the approach of fundamental measure theory (FMT). Here, a fully three-dimensional investigation is performed, which, again, accounts explicitly not only for the ionic solute particles, but also for the solvent particles, and thus provides insight into effects caused by ion-solvent coupling. Furthermore, the usage of FMT by construction includes effects due to the finite size of the considered particles. The approach taken in this chapter introduces a versatile framework to analyze a broad range of types of surface charge heterogeneities even beyond the linear response regime. The study of, e.g, sinusoidal and striped surface charge distributions reveals a sensitive dependence of the number density profiles of the fluid components and of the electrostatic potential on the magnitude of the charge as well as on details of the surface charge patterns at small scales. Up to occasional extensions and modifications, the research presented in this chapter matches the one published in Ref. [7].

4.1 Introduction

In a wide spectrum of research areas and applications — ranging from electrochemistry [122, 123] and wetting phenomena [124, 125] via coating [126] and surface patterning [5, 127] to colloid science [128, 129, 146] and microfluidics [130, 131] — there is a significant interest in understanding the structure of electrolyte solutions at solid substrates. Most of the theoretical studies dealing with such fluids close to a substrate neglect heterogen-

eities in the interaction between the wall and the fluid, modeling the substrate as being uniform. On one hand this approach simplifies the calculations significantly, whereas on the other hand there is a lack of experimental data concerning the actual local structure of these fluids near substrates. In the case of *electrically neutral* fluids and *uncharged* walls this simplification is typically well justified because, besides wetting transitions, the bulk correlation length sets the length scale, on which heterogeneities of surface properties influence the fluid [107]. This bulk correlation length is, sufficiently far from critical points, of the order of a few molecular diameters, rendering any heterogeneity to be of negligible importance. In contrast to this short length scale, a dilute electrolyte solution close to nonuniformities of the *surface charge density* of a charged substrate is influenced on the length scale of the Debye length, which is, for this type of solutions, much larger than the size of the fluid constituents. Additionally, surface charge heterogeneities of typical substrates (e.g., minerals and polyelectrolytes) are usually also of the order of the Debye length of the fluid close to these substrates [108–110]. Consequently, for the treatment of dilute electrolyte solutions in contact with charged surfaces, the approximation of assuming uniform surface charge densities is questionable.

Over the last years, an increasing interest in these surfaces has developed, leading to a number of studies investigating the influence of heterogeneously charged walls, for example on the effective interaction between two substrates in contact with an electrolyte solution [111, 113, 114, 116, 117, 132–137]. These studies revealed, e.g., the effective interaction in case of nonuniform substrates to cause lateral forces in addition to the ones in normal direction, which are commonly known. Despite describing the solute components in a wide range of ways, all those studies neglect the size of the solvent particles and its influence on the permittivity of the fluid, treating it as structureless dielectric continuum. As has been shown in previous studies [118–120], due to a competition between the solvation and the electrostatic interaction, there are coupling effects occurring in bulk electrolyte solutions, which cannot be captured by these simple approaches. However, in particular in the presence of ion-solvent coupling, fluctuations of the solvent density decay on the scale of the Debye length, which leads to inhomogeneities in the wall-solvent interaction influencing the structure of the electrolyte solution in contact with the charged substrate on a length scale much larger than molecular sizes. A very recent example of such a study, deriving exact solutions of the shape of the electrostatic potential in an electrolyte solution close to a heterogeneously charged surface within Poisson-Boltzmann theory, is given by Ref. [147]. There, previous research of coworkers and myself [6] was expanded with respect to the description of nonlinear responses, albeit not explicitly including the solvent and neglecting the spatial extent of all fluid particles. Moreover, in Ref. [148] a one-dimensional wall with a single, isolated step in the surface charge in contact with

a hard-sphere electrolyte solution was studied in a broad parameter range, concerning both surface specifications and characteristics of the electrolyte solution. It was shown, that the valences of the ions, their respective sizes, their concentration, and the strength of the surface charge can lead to various structural effects in the fluid structure both perpendicular and parallel to the wall. However, in that study, the solvent was again treated only implicitly and thus coupling effects have been neglected.

In the present analysis, I aim for a deeper understanding of the structural effects of surface charge nonuniformities on a nearby dilute electrolyte solution in terms of all fluid components. The system is studied by means of DFT in combination with FMT, which has been shown to be a powerful framework for investigating fluid structures in terms of number density profiles [46, 57, 121]. The study at hand is concerned with explicitly calculating the structure of an electrolyte solution composed of neutral solvent particles and a single univalent salt component, described as hard spheres. As for the structure of the two-dimensional surface nonuniformities, they can be arbitrary in strength and also their spatial arrangement can de facto be chosen freely, with the computational capacities being the only limitation. However, here I restrict myself to periodic surface charge patterns. Furthermore, I lift the constraint of overall charge neutral walls, as has been used in Refs. [111, 116, 117, 132]. The research in this chapter addresses the open questions from Chap. 3 and Ref. [6] concerning the influence of microscopic details and nonlinear effects on the structure of a dilute electrolyte solution close to heterogeneously charged walls. In the present study I have chosen a small subset of the parameter range analyzed in Ref. [148], for which it has been shown, that the valences have a negligible effect and that the width of the region, which is influenced by a variation of the surface charge, is computationally manageable (see Sec. 4.2.4). Furthermore, I have focussed on the effect of multiple heterogeneities of the sort of the ones discussed in Ref. [148], thereby creating a two-dimensional patterned surface.

In the following, first the setup and the formalism will be introduced in Sec. 4.2. Secondly, in Sec. 4.3 various selected surface charge patterns are studied. From a simple homogeneously charged surface investigated in Sec. 4.3.2, I move towards more complicated charge distributions such as a sinusoidal shape (Sec. 4.3.3), patch-like, or rectangular patterns (Sec. 4.3.4). Conclusions and a summary are presented in Sec. 4.4.

4.2 Theoretical foundations

4.2.1 Setup

In the present chapter, the interplay of an electrically nonuniform hard wall and a fluid, comprising hard spheres and monovalent ions, is studied. For $z < 0$ the system consists of a semi-infinite impenetrable (hard) wall; on the other hand for $\mathcal{V} = \{\boldsymbol{r} \in \mathbb{R}^3 | z > 0\}$ the system is occupied by a fluid mixture of hard spheres, where z is one of the three spatial coordinates $\boldsymbol{r} = (x, y, z)$. This fluid is an electrolyte solution with three particle species: an uncharged solvent (index "1"), monovalent cations (index "2"), and monovalent anions (index "3"), all of which are taken to be of the same size. All these interactions are either of electrostatic nature, as caused by electric monopoles at the surface of the wall ($z = 0$) and by the monovalent ions, or of a nonelectrostatic, purely repulsive nature caused by the steric repulsion of the hard spheres and the hard wall. The precise geometries of the electric nonuniformities at the wall are given in the context of the various scenarios studied in the subsequent Sec. 4.3.

However, in all cases I assume the nonuniformities at the wall to be periodic with a unit cell of size $L_x \times L_y =: P_x R_1 \times P_y R_1$, where R_1 is the radius of the solvent particles. P_x and P_y are the dimensionless widths of the box, for which the numerical evaluations are performed (see Sec. 4.A). Furthermore, I assume that all deviations from the bulk behavior are located in close proximity to the wall, justifying a restriction of the numerical treatment to a length $L_z = P_z R_1$ in the direction normal to the wall and assuming the densities to take on their respective bulk values for $z > L_z$. With the same justification I assume the electrostatic potential Ψ to decay purely exponentially with the decay length given by the Debye length $1/\kappa = \sqrt{\frac{\varepsilon_r}{8\pi l_{\mathrm{B}0} I}}$ for $z > L_z$, where $l_{\mathrm{B}0} = \frac{e^2}{4\pi\varepsilon_0 k_{\mathrm{B}} T} = 56.8\,\mathrm{nm}$ is the vacuum Bjerrum length, ε_r is the relative permittivity, and $I = \varrho_{2,b} = \varrho_{3,b}$ is the ionic strength, which, in the present case of monovalent ions, equals the bulk number density of the cations and the anions.

In order to tackle the system described above numerically, I introduce a discretization of the system by using discrete versions of the equations derived in the following. However, in order to illustrate the approach, I use the continuous expressions. For further details concerning the discretization see Sec. 4.A.

4.2.2 Density functional theory

In order to determine the equilibrium number density profiles $\boldsymbol{\varrho} = (\varrho_1, \varrho_2, \varrho_3)$ of the three species I use density functional theory [46, 57, 121]. To this end I establish the

approximate density functional $\beta\Omega[\boldsymbol{\varrho} = (\varrho_1, \varrho_2, \varrho_3)]$, which is minimized by the equilibrium number density profiles of the three species.

The exactly known expression for the ideal gas contribution

$$\beta\Omega_{\mathrm{id}}[\boldsymbol{\varrho}] = \int_{\mathcal{V}} \mathrm{d}^3 r \; \sum_i \left(\varrho_i (\ln(\varrho_i \Lambda_i^3) - 1 - \beta\mu_i) \right), \tag{4.1}$$

where $\beta = 1/(k_{\mathrm{B}}T)$ is the inverse thermal energy, μ_i are the chemical potentials of the three species, and Λ_i are the thermal de Broglie wavelengths of the three species. In addition to this, I use FMT in the White Bear I version [73] to account for the hard sphere nature of the fluid constituents. This leads to an excess free-energy functional for the hard core part given by

$$\beta F^{\mathrm{hc}}[\boldsymbol{\varrho}] = \int_{\mathcal{V}} \mathrm{d}^3 r' \; \Phi(\{n_\alpha(\boldsymbol{r}')\}), \tag{4.2}$$

with the volume $\mathcal{V} = \mathbb{R}^2 \times (0, \infty)$ and the reduced free-energy density

$$\Phi = -n_0 \ln(1 - n_3) + \frac{n_1 n_2 - \boldsymbol{n}_1 \cdot \boldsymbol{n}_2}{1 - n_3} + (n_2^3 - 3 n_2 \boldsymbol{n}_2 \cdot \boldsymbol{n}_2) \frac{n_3 + (1 - n_3)^2 \ln(1 - n_3)}{36\pi n_3^2 (1 - n_3)^2} \tag{4.3}$$

as a function of the weighted densities

$$n_\alpha(\boldsymbol{r}) = \sum_{i=1}^{3} \int_{\mathcal{V}} \mathrm{d}^3 r' \; \varrho_i(\boldsymbol{r} - \boldsymbol{r}') \omega_i^{(\alpha)}(\boldsymbol{r}'). \tag{4.4}$$

Following Ref. [73], the weight functions are given by

$$\omega_i^{(3)}(r) = \Theta(R_i - r), \tag{4.5}$$

$$\omega_i^{(2)}(r) = \delta(R_i - r), \tag{4.6}$$

$$\omega_i^{(1)}(r) = \frac{\omega_i^{(2)}(r)}{4\pi R_i}, \tag{4.7}$$

$$\omega_i^{(0)}(r) = \frac{\omega_i^{(2)}(r)}{4\pi R_i^2}, \tag{4.8}$$

$$\boldsymbol{\omega}_i^{(2)}(r) = \frac{\boldsymbol{r}}{r} \delta(R_i - r), \text{ and} \tag{4.9}$$

$$\boldsymbol{\omega}_i^{(1)}(r) = \frac{\boldsymbol{\omega}_i^{(2)}(r)}{4\pi R_i}, \tag{4.10}$$

where R_i are the radii of the three species denoted by index i.

Furthermore, in the present study electrostatic contributions play a role, all of which

are combined in the form of the electric field energy density $\beta U_{\mathrm{el}}[\boldsymbol{\varrho}]$ given by (see Eqs. (4.28) and (4.29))

$$\beta U_{\mathrm{el}}[\boldsymbol{\varrho}] = \frac{\beta}{2} \int_{\mathcal{V}} \mathrm{d}^3 r \; \varepsilon_0 \varepsilon_r(\boldsymbol{r}) (\nabla \Psi(\boldsymbol{r}))^2. \tag{4.11}$$

Here, ε_0 is the vacuum permittivity, ε_r is the relative permittivity, and Ψ is the electrostatic potential profile. The relative permittivity ε_r will be discussed in more detail in Sec. 4.3.1. Furthermore, it should be noted, that the calculation of the electrostatic field energy is mathematically identical to other, commonly used variants, such as the ones in Refs. [97, 106] (see Sec. 4.B). In the context of the present investigation the expression in Eq. (4.11) is chosen due to its close connection to the applied numerical two-step minimization method. Its reliability can readily be tested by comparing the results for a homogeneous wall (Sec. 4.3.2) with corresponding results in Refs. [149–151]. The resulting expression for the density functional used in the present study is

$$\beta \Omega[\boldsymbol{\varrho}] = \int_{\mathcal{V}} \mathrm{d}^3 r \; \left(\sum_i \varrho_i (\ln(\varrho_i \Lambda_i^3) - 1 - \beta \mu_i) \right) + \beta F^{\mathrm{hc}}[\boldsymbol{\varrho}] + \beta U_{\mathrm{el}}[\boldsymbol{\varrho}], \tag{4.12}$$

which in turn can now be used to determine the Euler-Lagrange equations. Whereas the hard-core contribution $\beta F^{\mathrm{hc}}[\boldsymbol{\varrho}]$ to the density functional in Eq. (4.12) is based on the fundamental measure theory (FMT) described by Eqs. (4.2) - (4.10), the electrostatic contribution $\beta U_{\mathrm{el}}[\boldsymbol{\varrho}]$ in Eq. (4.11) is a random-phase approximation (RPA). Hence, one cannot expect that the second-moment Stillinger-Lovett sum rule or the consistency between the test-particle and the Ornstein-Zernike route to the pair distribution functions are fulfilled. However, this should not be regarded as a serious disadvantage, because the present investigation is addressing the fluid structure close to a solid surface, which is strongly dominated by the influence of the external field of the wall and is influenced only to a small extent by correlations from the bulk.

4.2.3 Derivation of the Euler-Lagrange equations

Using the previously established density functional (see Sec. 4.2.2) I now can derive the corresponding Euler-Lagrange equations, which provide the equilibrium density profiles. Since minimizing with respect to all three density profiles and the potential distribution at the same time is computationally very costly, I divide the minimization into first minimizing for the equilibrium form $\Psi(\boldsymbol{r})$ of $\psi(\boldsymbol{r})$ at fixed density profiles $\boldsymbol{\varrho}$ and subsequently minimizing with respect to the three density profiles $\boldsymbol{\varrho}(\boldsymbol{r})$.

In order to determine the equilibrium form of $\psi(\boldsymbol{r})$ for Eq. (4.11), I introduce

$$\mathcal{E}[\psi, q, \varepsilon_r, \sigma] = \int_{\mathcal{V}} \mathrm{d}^3 r \, \left(\frac{\varepsilon_0 \varepsilon_r(\boldsymbol{r})}{2} (\nabla\psi(\boldsymbol{r}))^2 - q(\boldsymbol{r})\psi(\boldsymbol{r}) \right) - \int_{\partial\mathcal{V}} \mathrm{d}^2 s \, \sigma(\boldsymbol{s})\psi(\boldsymbol{s}, 0), \tag{4.13}$$

where $q(\boldsymbol{r}) = e(\varrho_2(\boldsymbol{r}) - \varrho_3(\boldsymbol{r}))$ is the local charge density, and $\sigma(\boldsymbol{s})$ is the surface charge density at the wall surface $\partial\mathcal{V} = \{\boldsymbol{r} \in \mathbb{R}^3 | (x, y, z = 0) = (\boldsymbol{s}, 0)\}$. As shown in Sec. 4.B, the electrostatic field energy can be written as

$$\beta U_{\mathrm{el}}[\boldsymbol{\varrho}] = -\beta\mathcal{E}[\Psi, q, \varepsilon_r, \sigma], \tag{4.14}$$

that is, given the equilibrium potential $\Psi(\boldsymbol{r})$ for a given charge distribution $q(\boldsymbol{r})$, the electrostatic contribution to the density functional can be expressed in terms of $\mathcal{E}[\Psi, q, \varepsilon_r, \sigma]$.

Additionally, by construction the variation of $\mathcal{E}[\psi, q, \varepsilon_r, \sigma]$ with respect to ψ vanishes for the equilibrium profile Ψ (see Sec. 4.C). Therefore, I can find the equilibrium potential distribution Ψ corresponding to a given distribution of the densities, i.e., $\sigma(\boldsymbol{s})$, $q(\boldsymbol{r})$, and $\varepsilon_r(\boldsymbol{r})$, by minimizing $\mathcal{E}$ with respect to ψ. Following these lines and incorporating the numerically necessary discretization as outlined in Sec. 4.2.1, one finds the Euler-Lagrange equations (Eqs. (4.31) - (4.33)) for the electrostatic potential, which depend on the distance from the wall.

After determining the electrostatic potential distribution by solving Eqs. (4.31), (4.32), and (4.33), I can use the resulting solution for $\psi(\boldsymbol{r}) = \Psi(\boldsymbol{r})$ in accordance with Eq. (4.11) in order to determine the density functional and the following Euler-Lagrange equations for the three number densities $\boldsymbol{\varrho}$:

$$\ln(|\mathcal{C}^*|\varrho_j(\boldsymbol{r})) = \mu_j^* - \sum_\alpha \int_{\mathcal{V}} \mathrm{d}^3 r' \, p_\alpha \frac{\partial\Phi(\boldsymbol{r})}{\partial n^\alpha(\boldsymbol{r'})} \omega_j^{(\alpha)}(\boldsymbol{r'} - \boldsymbol{r}) + \frac{\partial\beta\mathcal{E}}{\partial\varrho_j(\boldsymbol{r})}. \tag{4.15}$$

Here $|\mathcal{C}^*|$ is the size of one of the cells used in the numerical implementation (see Sec. 4.A), $\mu_j^* = \beta\mu_j - \ln(\Lambda_j^3/|\mathcal{C}^*|)$ is the dimensionless effective chemical potential of species j, and the prefactor is $p_\alpha = -1$ for vectorial weights $\boldsymbol{\omega}_\alpha$ and $p_\alpha = 1$ for scalar weights. The three terms result from the ideal gas contribution, the FMT contribution, and the electrostatic interactions, respectively.

4.2.4 Choice of parameters

For solving the Euler-Lagrange equations obtained above (Sec. 4.2.3) and in Sec. 4.C, there are certain parameters which have to be fixed in advance. Besides the surface charge distribution $\sigma(\boldsymbol{s})$, which is varied for each calculation, and the permittivity, which will be

discussed later (see Sec. 4.3.1), the bulk packing fraction η, the ionic strength I of the bulk liquid, the radii of the three particle types R_j, and the parameter $\chi = \frac{9\pi l_{\mathrm{B}0}}{R_1}$ (see Sec. 4.C) have to be fixed. When choosing these parameters, I took the respective values for water as guidance, resulting in particle radii $R_1 = R_2 = R_3 = 1.5\,\text{Å}$ and $\chi \approx 1.05 \times 10^4$, where the vacuum Bjerrum length is $l_{\mathrm{B}0} = 56.8\,\mathrm{nm}$. Furthermore, inspired by Ref. [73], the bulk packing fraction is set to $\eta = 0.4257$, which together with the chosen particle diameter corresponds to the bulk number density $\varrho_b^{\mathrm{tot}} = \varrho_{1,b} + \varrho_{2,b} + \varrho_{3,b} = 50\,\mathrm{mol\,l^{-1}} \approx 30\,\mathrm{nm^{-3}}$. Finally, the ionic strength is set to $I = 100\,\mathrm{mM} \approx 6 \times 10^{-2}\,\mathrm{nm^{-3}}$.

4.3 Results and Discussion

4.3.1 Structure of the permittivity

Before moving on to the discussion of the various charge patterns in the following sections, this paragraph focuses on the structure of the permittivity used in the present chapter. It has previously been shown [152], that a solvent density dependent, linear interpolation of the permittivity between its vacuum value $\varepsilon_r^{(0)} = 1$ and its value for the pure system (water) $\varepsilon_r^{(1)} = 80$ matches the behavior of fluid mixtures very well. I have therefore compared two different approaches to set the permittivity in the current study: one is a constant permittivity $\varepsilon_r = 80$ throughout the whole system, the other one is a linear interpolation between the two extreme values, scaled with the weighted solvent density:

$$\varepsilon_r(\boldsymbol{r}) = \varepsilon_r^{(0)} + \frac{3(\varepsilon_r^{(1)} - \varepsilon_r^{(0)})}{4\pi\varrho_{1,b}R_1^3} \int_{\mathcal{V}} \mathrm{d}^3r'\; \varrho_1(\boldsymbol{r} - \boldsymbol{r'})\omega_1^{(3)}(\boldsymbol{r}); \tag{4.16}$$

the structure of this equation is adopted from the FMT approach. In Eq. (4.16) the solvent density is essentially averaged over a particle radius, whereas for the constant permittivity the solvent density is basically averaged over an infinite region. Calculating the density profile for a homogeneous charge distribution $\sigma(\boldsymbol{s}) = \mathrm{const}$, I have compared these two approaches for the permittivity. In Fig. 4.1 the electrostatic potential Ψ for two homogeneous wall charges $\sigma = 10^{-4}\,e/(4\mathrm{R}_1^2)$ and $\sigma = 10^{-5}\,e/(4\mathrm{R}_1^2)$ and for the two cases of the permittivity treatment is shown as function of the normal distance z from the wall. Since there is no lateral variation of the surface charge distribution, there is consequently also no dependence of the electrostatic potential on the lateral position, which is why only the $z-$dependence is shown here. Although the two expressions used for the permittivity are quite distinct, the two approaches yield rather similar results. All differences solely occur on a length scale of fractions of the particle radius R_1 away

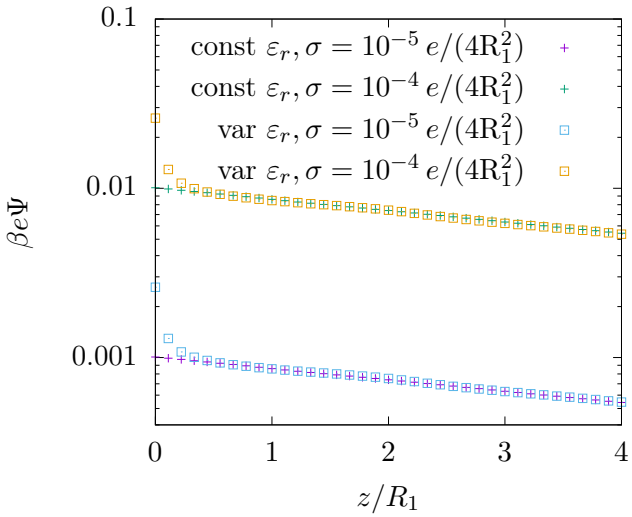

Figure 4.1: Electrostatic potential $\Psi(\boldsymbol{r})$ as function of the distance z from the wall for homogeneously charged walls, i.e., σ = const. Due to the homogeneous charge distribution, Ψ does not depend on x and y. The curves differ both in the strength of the wall charge ($\sigma = 10^{-4}\, e/(4\mathrm{R}_1^2)$ and $\sigma = 10^{-5}\, e/(4\mathrm{R}_1^2)$) and in the way the permittivity is incorporated. For the crosses the permittivity in the whole system is constant ($\varepsilon_r = 80$) and for the squares the permittivity at each position is calculated according to Eq. (4.16). Albeit being vastly different, both treatments of the permittivity produce nearly identical results. All differences occur on the length scale of fractions of the particle radius, where the varying permittivity leads to stronger potentials at the wall.

from the wall, where the varying permittivity ε_r leads to stronger potentials. This is due to the vanishing solvent density $\varrho_1(\boldsymbol{r}) = 0$ for distances smaller than a particle radius $z < R_1$, caused by steric repulsion. Therefore, close to the wall the permittivity decreases, which in turn causes an increasing potential Ψ. However, this increase is restricted to the proximity of the wall, leading to basically indistinguishable profiles even at distances of the order of the particle radius. Since treating the permittivity according to Eq. (4.16) is computationally very costly and the benefits are apparently minor, I treat the permittivity as $\varepsilon_r(\boldsymbol{r})$ = constant = 80 throughout the whole system, i.e., for all $\boldsymbol{r} \in \mathcal{V}$ with $\mathcal{V} = \{\boldsymbol{r} \in \mathbb{R}^3 | (x, y, z > 0) = (\boldsymbol{s}, z > 0)\}$.

4.3.2 Constant wall charge distribution

After studying the influence of the permittivity and describing the form used in the present chapter in the previous Sec. 4.3.1, I now turn towards the analysis of various surface charge patterns, where I first focus on the simplest case of a spatially constant surface charge distribution σ = const and vary solely its strength. First, I studied the case of a vanishing surface charge $\sigma = 0$. In this case, due to the hard sphere nature

of the model, close to the wall layering of the particles occurs (see Fig. 4.2). This is an expected result, as it has been reported in numerous previous studies (e.g., Ref. [73, 153]). If the strength of the surface charge density is slowly increased, one can identify the effects introduced in the system via electrostatics. In Fig. 4.2 the solvent densities for three different surface charge strengths is shown, ranging from a neutral wall ($\sigma = 0$) to a highly charged wall with $\sigma = 10^{-1}\, e/(4\mathrm{R}_1^2) \approx 16\,\mu\mathrm{C\,cm}^{-2}$. As can be seen in Fig. 4.2, only for high wall charges, the density profiles of the solvent start to deviate from the ones found for pure hard spheres with no electrostatic addition. For these high wall charges the solvent density decreases in close proximity to the charged substrate. However, the size and the range of these deviations are relatively small and even for distances of about two particle radii away from the wall, the profiles reduce to the purely hard sphere ones.

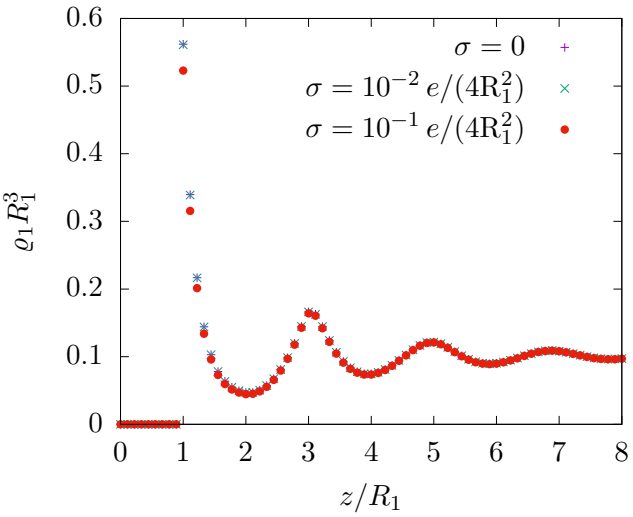

Figure 4.2: Solvent density $\varrho_1(\boldsymbol{r})$ as function of the distance z from the wall for three cases of homogeneous wall charges. The case $\sigma = 0$ corresponds to an uncharged wall. The resulting profile is caused only by steric repulsion of the hard spheres. One can see, that only for high wall charges, i.e., $\sigma = 10^{-1}\, e/(4\mathrm{R}_1^2) \approx 16\,\mu\mathrm{C\,cm}^{-2}$, the density profile deviates from the purely hard sphere profile. For these wall charges the density of the solvent decreases close to the wall, however the amplitude and the range of these changes are rather small. Still, the layer structure, caused by the hard spheres, is predominant.

By studying the charge densities q, and by that the profiles of the ions, a similar observation can be made. In Fig. 4.3, the charge density q is shown for a wide range of wall charges σ, for which the charge density and thus the profiles of the ions vary only by a proportionality factor. However, for high wall charges, the behavior changes. For these instances, the charge density increases directly at the wall and decays faster with the distance z from the wall than in the case of lower charge densities, as can clearly be seen in Fig. 4.3. In combination with the findings for the solvent particles, the reason for this

effect is obvious. For small wall charges σ, the fluid reacts by simply swapping co- and counterions, so that the total density as well as the solvent density is largely unaffected by this replacement of ions. However, if the surface charge is becoming too large, this simple replacement is insufficient to neutralize the charge apparent at the wall. Thus, the density of the counterions has to increase even further by superseding, in parts, the solvent particles. This explains the decrease in the solvent density ϱ_1 close to the wall in the case of high wall charges and the change in the shape of the charge density profiles.

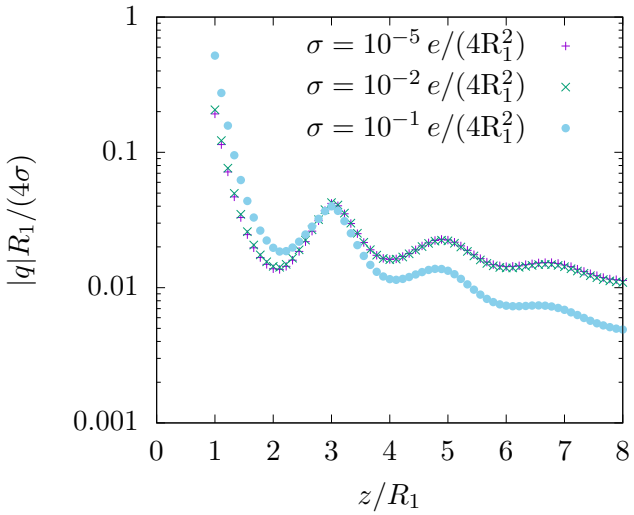

Figure 4.3: Reduced charge density $q(\boldsymbol{r}) = e(\varrho_2(\boldsymbol{r}) - \varrho_3(\boldsymbol{r}))$ as function of the distance z to the wall for three cases of homogeneous wall charges. For all three cases one can clearly see the layer structure in the densities, which is caused by the hard sphere nature of the particles. Similar to the solvent density, the reduced charge density stays more or less constant for a wide range of wall charge strengths and deviates noticeably from the low wall charge behavior only for high wall charges, i.e., $\sigma = 10^{-1}\, e/(4\mathrm{R}_1^2) \approx 16\,\mu\mathrm{C\,cm}^{-2}$. In this case the charge density increases upon approaching closely the wall and decreases for distances larger than three particle radii, when compared with the profiles for smaller wall charges. Also, the hard sphere nature of the particles is still important for high wall charges, as expressed via the layering, which is still apparent.

In addition to the number density profiles, I also studied the profile of the electrostatic potential $\beta e\Psi$ occurring in the case of charged substrates. In Fig. 4.4 it is shown as function of the distance z from the wall for three strengths of the wall charge density. The observations here are similar to the previously discussed cases of the number density profiles. For most of the range of wall charges σ studied here, the potential is only varying by a proportionality factor so that the overall shape of its decay with increasing distances z from the wall stays the same, similar to the results found for the number density profiles. Again, this behavior changes for high values of the surface charge density σ. As previously seen for the particle profiles in Figs. 4.2 and 4.3, the decay of the electrostatic potential

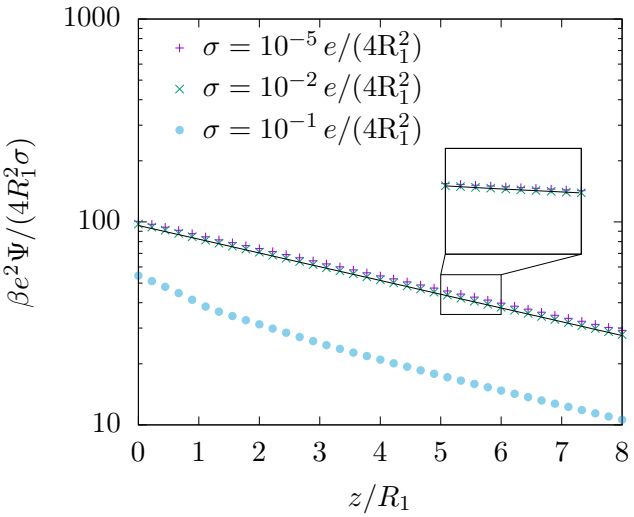

Figure 4.4: Reduced electrostatic potential $\beta e\Psi$ as function of the distance z from the wall for three cases of homogeneous wall charges (various symbols). For all three cases one can clearly see the linear behavior in the region $z < R_1$, which occurs because there is no charge present. Also, in all three cases the potential decreases monotonously with increasing distance z. However, in the case of high wall charge densities, i.e., $\sigma = 10^{-1}\, e/(4\mathrm{R}_1^2) \approx 16\,\mu\mathrm{C\,cm}^{-2}$ (blue circles), there is an apparent change in the behavior: the amplitude of the potential right at the wall decreases, and the profile decays faster in normal direction. Additionally, the results for the wall charge density $\sigma = 10^{-2}\, e/(4\mathrm{R}_1^2)$, calculated within the model used in Chap. 3 and Ref. [6], is shown here as a black line (see the inset). This prediction matches the present results remarkably well.

Ψ changes upon approaching the wall charge density $\sigma = 10^{-1}\, e/(4\mathrm{R}_1^2) \approx 16\,\mu\mathrm{C\,cm}^{-2}$. For sufficiently high wall charges, the potential value right at the wall drops below the corresponding value for lower wall charges, and the decay converges more slowly to the asymptotic behavior with the Debye length as decay length. This change of behavior can be explained in terms of the observations made for the charge distribution q, as a higher absolute value of the charge (the sign is naturally the opposite of the sign of the wall charge) leads to a stronger screening of the wall charges and thus to smaller values of the electrostatic potential Ψ. It also clearly marks the range of surface charge strengths, within which the linear approximation breaks down. Furthermore, Fig. 4.4 shows the result for the corresponding situation of a homogeneous wall charge $\sigma = 10^{-2}\, e/(4\mathrm{R}_1^2)$ calculated within the framework of Chap. 3 (Ref. [6]) (black line, see the inset). This result is a perfect match of our findings for the wall charge within the linear regime. This is remarkable, as the framework of Chap. 3, i.e., Ref. [6], uses a heavily simplified fluid model. Still, as shall be seen in the following sections, it appears to provide reliable results for the electrostatic potential Ψ.

With these insights into the general ranges for which the surface charge σ leads to

structural effects even for a homogeneously charged wall, I move on towards more complex surface charge distributions.

4.3.3 Sinusoidal wall charge

As a first step towards more complex surface charge patterns, I first turn towards a one-dimensional sinusoidal charge distribution

$$\sigma(x, y) = \sigma_{\max} \sin(2\pi x/\lambda) \tag{4.17}$$

with amplitude $\sigma_{\max}$ and wavelength λ. In contrast to the previous cases studied in Sec. 4.3.2, there is no net charge on the wall. Because of this absence of a net charge, one expects a very short-ranged influence of the wall structure on that of the fluid. As can be seen in Fig. 4.5, the effect of the surface charge inhomogeneity on the solvent is indeed limited to a very short range with a small amplitude, as no effects of solvent particle displacement are visible. This hints at small charge density values inside the fluid. In fact, the difference between the two regions of linear and nonlinear fluid response (appearing for $\sigma = \text{const}$) seems to vanish, or at least the transition seems to be shifted as a function of the wall charge amplitude $\sigma_{\max}$. This is in line with the observation that in the case of the sinusoidal surface charge distribution the solvent density $\varrho_1(\boldsymbol{r})$ exhibits no visible deviations from the profiles found for a purely hard sphere system without any electrostatics (see Fig. 4.5).

However, when moving on to the charge density distribution $q(\boldsymbol{r}) \equiv e(\varrho_2(\boldsymbol{r}) - \varrho_3(\boldsymbol{r}))$, which is shown in Fig. 4.6, there are clear effects specific to the sinusoidal charge distribution. Similar to Fig. 4.3, in Fig. 4.6 the charge density distribution $q(\boldsymbol{r})$ is shown as a function of the distance z from the wall. First, as already suspected from the solvent density profiles $\varrho_1(\boldsymbol{r})$ in Fig. 4.5, one can see, that the amplitude of the charge density distribution inside the fluid is indeed significantly smaller than in the case of an electrostatically homogeneous wall. This small amplitude leads to apparent "plateaus" of the profiles, which occur for numerical reasons. This effect, however, is of no importance for any of the following conclusions. Second, the profiles in Fig. 4.6 clearly show, that the wavelength λ of the surface charge pattern has a strong influence on the decay behavior of the charge density inside the fluid. With increasing periodicity, i.e., increasing λ, the decay length of the charge density profiles increases, too. Whereas the charge density decays to (numerically) vanishing values within a length of only a few particle radii for a wavelength of $\lambda = 1 \times \mathrm{R}_1$, it seems to converge to an asymptotically exponential decay for larger wavelengths of the surface charge pattern $\sigma(\boldsymbol{s})$. Furthermore, as stated previ-

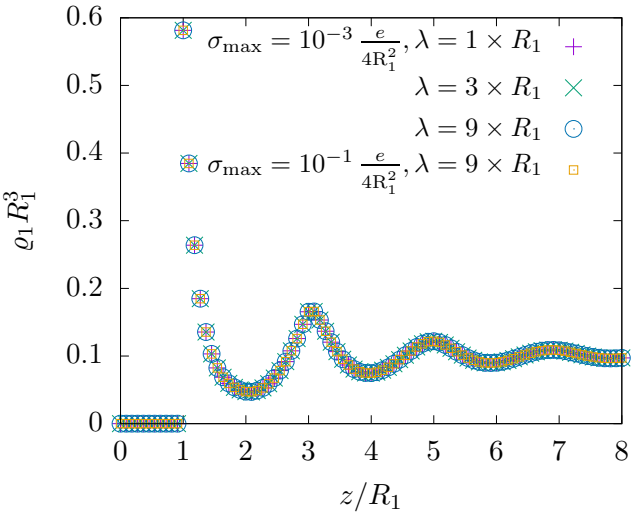

Figure 4.5: Solvent density $\varrho_1(\boldsymbol{r})$ for a sinusoidal surface charge distribution as function of the distance z from the wall for two values of the wall charge strength [$\sigma_{\max} = 10^{-3}\, e/(4\mathrm{R}_1^2)$ and $10^{-1}\, e/(4\mathrm{R}_1^2)$] and three values of the period length [$\lambda = 1 \times \mathrm{R}_1, 3 \times \mathrm{R}_1,$ and $9 \times \mathrm{R}_1$]. The two wall charge amplitudes are taken from the two regimes found in Sec. 4.3.2, with $\sigma_{\max} = 10^{-3}\, e/(4\mathrm{R}_1^2)$ being an exemplary value for the linear response regime. The other value of the wall charge amplitude, $\sigma_{\max} = 10^{-1}\, e/(4\mathrm{R}_1^2)$, is taken from the suspected nonlinear response regime, as identified in Sec. 4.3.2. There is no visible lateral variation of the profiles, because the laterally varying surface charge density is not strong enough to influence the neutral solvent number density profiles. The profiles show the well-known layering of hard spheres close to a hard wall. When compared with Fig. 4.2, it is clearly visible, that neither the wall charge amplitude nor the period length of the wall charge distribution $\sigma(\boldsymbol{s})$ has any influence on the structure of the solvent density $\varrho_1(\boldsymbol{r})$.

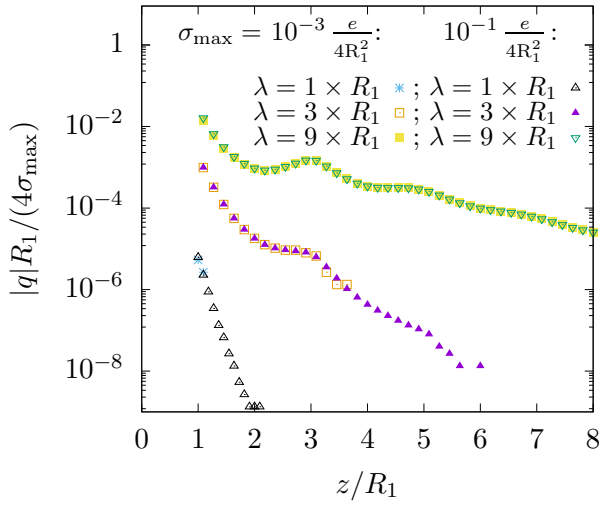

Figure 4.6: Reduced charge density $q(\boldsymbol{r})$ as function of the distance from the wall z evaluated at the maximal amplitude, i.e., at $x = \lambda/4$, for two values of the wall charge strength [$\sigma_{\max} = 10^{-3}\,e/(4R_1^2)$ and $10^{-1}\,e/(4R_1^2)$] and three values of the period length [$\lambda = 1 \times R_1, 3 \times R_1,$ and $9 \times R_1$]. The two wall charge amplitudes are taken from the two regimes found in Sec. 4.3.2, with $\sigma_{\max} = 10^{-3}\,e/(4R_1^2)$ being an exemplary value for the linear response regime. The other value of the wall charge amplitude, $\sigma_{\max} = 10^{-1}\,e/(4R_1^2)$, is taken from the suspected nonlinear response regime, as identified in Sec. 4.3.2. Concerning the lateral variation of the profiles shown, it is strictly following the shape of the surface charge distribution, with the lateral position chosen here serving as an example. The known effect of cancellation of significant digits in the number densities generate the loss of precision for the charge density profile, leading to the plateaus visible in the profiles. The wavelength λ of the underlying surface charge structure $\sigma(\boldsymbol{s})$ (see Eq. (4.17)) clearly influences the decay behavior of the charge density. With increasing period length, the decay length increases. In order to highlight, that the amplitude $\sigma_{\max}$ of the charge distribution has apparently no further influence than that of a proportionality factor, here the charge density q is reduced accordingly by $\sigma_{\max}$.

ously for the solvent density profiles $\varrho_1(\boldsymbol{r})$ in Fig. 4.5, the profiles for the charge density $q(\boldsymbol{r})$ in the fluid show no dependence on the amplitude of the surface charge distribution, although the two values chosen for the amplitude $\sigma_{\max}$ were taken from the two regimes of different fluid reaction, which were found in Sec. 4.3.2.

Finally, as for the homogeneous wall charge (see Sec. 4.3.2), I investigated the electrostatic potential Ψ for the case of a sinusoidal surface charge pattern $\sigma(\boldsymbol{s})$ (see Eq. (4.17)). In Fig. 4.7 the electrostatic potential Ψ is shown for three different wavelengths of the surface charge ($\lambda = 1 \times R_1, 3 \times R_1,$ and $9 \times R_1$). Due to the lack of an effect, as has been shown in Figs. 4.5 and 4.6, here the amplitude of the surface charge pattern is kept constant at $\sigma_{\max} = 10^{-3}\,e/(4R_1^2)$. The various data points for a single value of z correspond to different lateral positions x along one period of the surface charge pattern.

First, although the different wavelengths clearly influence the charge density q of the fluid right next to wall, as can be inferred from Fig. 4.6, there seems to be no significant effect of the surface charge period length on the strength of the electrostatic potential Ψ at the wall. Second, also like seen for the charge density q, the electrostatic potential clearly decays exponentially with increasing distance z from the wall. The decay length of Ψ also clearly depends on the wavelength of the surface charge, where an increasing wavelength λ leads to an increased decay length. Note, that the deviation from the exponential decay for the case $\lambda = 1 \times \mathrm{R}_1$ is due to the numerically caused lack of precision in determining the charge density (see Fig. 4.6). In Fig. 4.7, in addition to the data points, there are three lines indicating the exponential decay corresponding to the prediction in Chap. 3, i.e., Ref. [6]. There, the decay as a function of z turned out to be proportional to

$$\beta e \Psi \propto \exp\left(-\sqrt{\kappa^2 + |\boldsymbol{q}_{\parallel}^2|}z\right), \tag{4.18}$$

where κ is the inverse Debye length and $|\boldsymbol{q}_{\parallel}|$ is the absolute value of the Fourier component of the dominating lateral pattern of the surface charge distribution, which in the present case of the sinusoidal surface charge pattern (see Eq. (4.17)) equals $2\pi/\lambda$. Note that neither the amplitudes of the lines shown in Fig. 4.7, nor the decay lengths are fitting parameters. The lines strictly follow the results obtained from the counterpiece of Eq. (4.18) in Chap. 3, respectively Ref. [6]. Although the system described in Chap. 3 and Ref. [6] was more basic and the description of the fluid was rather simplistic, the findings deliver remarkably accurate predictions when compared with the results of the present analysis using a significantly more elaborate fluid description. With this very good agreement with previous, more simplistic approaches, I move on to compare further, more complex, surface charge distributions $\sigma(\boldsymbol{s})$ with the predictions made in Ref. [6].

4.3.4 Various surface charge patterns

Moving on from the somewhat simple surface charge patterns $\sigma(\boldsymbol{s})$ discussed in Secs. 4.3.2 and 4.3.3, in the present section I investigate more complex charge distributions. The four principal cases of charge patterns studied here are shown in Fig. 4.8, where both lateral lengths L_x and L_y, the dimensionless charge width D, and the amplitude $\sigma_{\max}$ have been varied throughout the calculations. This variation of parameters leads, inter alia, to a variation of the effective surface charges, i.e., the averaged surface charge strengths σ_{av}, as the area fraction of the charged area compared to the total area of the surface charge unit cell $L_x \times L_y$ is changed. The influence of this change can be seen in Fig. 4.9. Here, the charge density $q(\boldsymbol{r})$ is shown as function of the distance z from

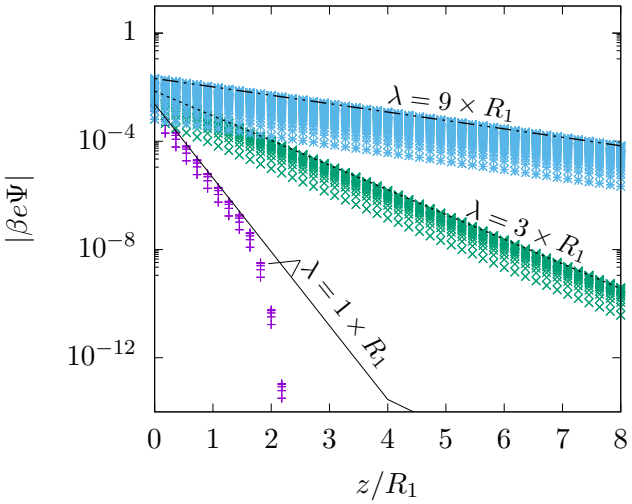

Figure 4.7: Electrostatic potential Ψ as a function of the distance z from the wall for all lateral positions (x, y) studied for three period lengths ($\lambda = 1 \times \mathrm{R}_1, 3 \times \mathrm{R}_1,$ and $9 \times \mathrm{R}_1$) of the sinusoidal wall charge distribution (see Eq. (4.17)). The amplitude of the wall charge is set to $\sigma_{\max} = 10^{-3}\, e/(4\mathrm{R}_1^2)$ for all these period lengths. Different data points of one color (shaded areas) for one normal distance correspond to various lateral positions (x, y) along one period of the surface charge pattern. Laterally varying strength of the surface charge leads to these broad ranges of data points. The width of these ranges provides information about the strength of the lateral variation: the wider the range, the stronger is the lateral variation of the electrostatic potential. The straight lines correspond to an exponential decay with a decay length, which results from a combination of the Debye length and the corresponding inverse dominant length scale following the prediction of the previous study discussed in Chap. 3 (see Eq. (4.18) and Ref. [6]). The agreement between this prediction and the present data is remarkable.

the wall. Note, that for the cases shown here, which all correspond to the case of the shortest lateral wavelength considered ($\lambda = 1 \times \mathrm{R}_1$), the dependence of the potential Ψ on the lateral position $\boldsymbol{s} = (x, y)$ disappears for $z \gtrsim R_1$. Therefore, the shown charge densities do not exhibit any visible lateral dependence. In Fig. 4.9 one can clearly see that, independent of the surface charge amplitude $\sigma_{\max}$, all surface charge patterns lead to qualitatively similar results. The charge decays exponentially with z and shows clear signs of the hard core nature of the particles at small distances from the wall. Furthermore, one can infer from these graphs, that the charge density profiles $q(z)$ smoothly converge towards the ones found in Fig. 4.3 as the area fraction of the charged surface is increased. Especially in the case of the stronger wall charge amplitude ($\sigma_{\max} = 10^{-1}\, e/(4\mathrm{R}_1^2)$, Fig. 4.9 (b)) this is interesting, because these profiles and their associated range of averaged surface charges coincide with the transition region from a linear to a nonlinear fluid reaction, as has been found previously (Sec. 4.3.2). The profiles in Fig. 4.9 corresponding

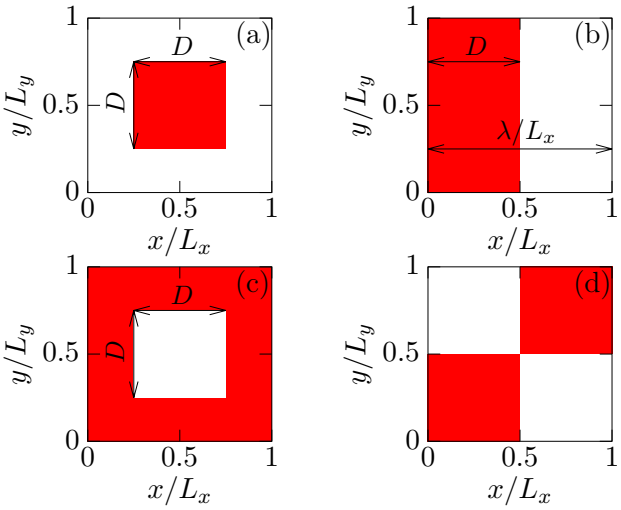

Figure 4.8: Further surface charge patterns $\sigma(\boldsymbol{s})$ considered in the present section. The red areas are regions with nonvanishing surface charges $\sigma(\boldsymbol{s}) = \sigma_{\max}$, whereas the white regions are uncharged. All these patterns correspond to the elementary cell of the surface charge pattern, which is periodically continued in both lateral directions along the wall surface. In panel (b) this leads to a striped pattern.

to a small area fraction and a weak averaged surface charge, respectively, still exhibit a linear response behavior, because the reduced profiles for both wall charge amplitudes $\sigma_{\max} = 10^{-1}\, e/(4\mathrm{R}_1^2)$ and $10^{-5}\, e/(4\mathrm{R}_1^2)$ are the same. Thus, the amplitude is solely a proportionality factor, which matches the behavior characterizing the linear response regime. However, if the area fraction and thus the averaged wall charge is increased, deviations from the respective profiles for the above two wall charge amplitudes increase, until finally the two profiles for the fully charged wall match the previous results in Fig. 4.3. Therefore, the transition between these regions is smooth and does not show any sign of a step-like variation.

Moving on to the case of longer lateral wavelengths, i.e., $\lambda = 3 \times \mathrm{R}_1$ and $\lambda = 9 \times \mathrm{R}_1$, close to the wall the charge density $q(z)$ starts to exhibit a lateral structure. In contrast to the profiles shown in Fig. 4.9, the lateral position $\boldsymbol{s}$ influences the local charge density $q(\boldsymbol{s}, z)$, for boundary conditions with these longer lateral wavelengths. This lateral variation is even more visible in the profiles of the electrostatic potential. Thus, in the following the behavior of the electrostatic potential Ψ for these more complicated charge distributions $\sigma(\boldsymbol{s})$ is studied. Here, I focus on surface charge patterns of the form shown in Fig. 4.8 (b):

$$\sigma(\boldsymbol{s}) = \begin{cases} \sigma_{\max}, & \text{for } N\lambda \leq x \leq (N+D)\lambda \\ 0, & \text{otherwise,} \end{cases} \tag{4.19}$$

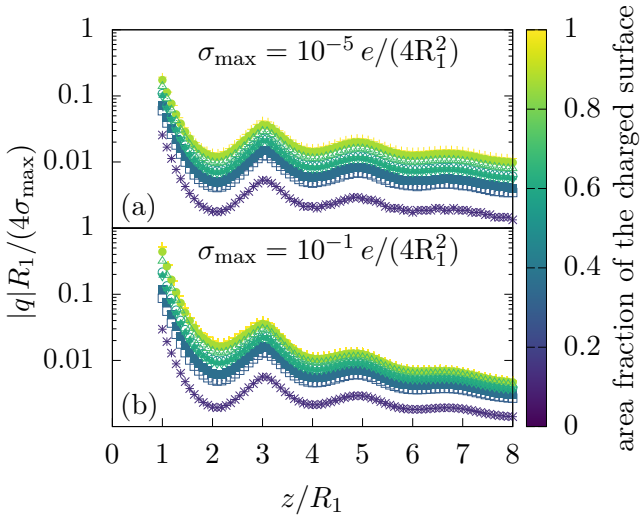

Figure 4.9: Reduced charge density $q(\boldsymbol{r})$ as function of the distance z from the wall and of the area fraction of the charged area per unit cell area for two cases of the wall charge strength: $\sigma_{\max} = 10^{-1}\, e/(4R_1^2)$ and $10^{-5}\, e/(4R_1^2)$. Since the lateral variation of the electrostatic potential Ψ de facto disappears for $z \gtrsim R_1$ for all the situations shown here, there is no visible dependence of the displayed profiles on the lateral position. All the profiles shown here correspond to various realizations of the charge patterns shown in Fig. 4.8. It turns out that the actual configuration (i.e., Figs. 4.8 (a), (b), (c), or (d)) is not important. Instead, only the averaged surface charge, given by the area fraction of the charged surface, appears to matter. One can clearly see, how the increase of the averaged wall charge also leads to increased charge densities inside the fluid and how the curves for increasing area fraction converge towards the ones for the homogeneous wall as shown in Fig. 4.3. Furthermore, the range of averaged surface charges shown in panel (b) coincides with the transition region as identified in Sec. 4.3.2. Therefore, panel (b) resolves this region in more detail.

with $\sigma_{\max}$ as the amplitude, $N \in \mathbb{Z}$, λ as the wavelength, and D being the dimensionless width of the charged stripe. I studied the cases $\lambda = L_x = 1 \times \mathrm{R}_1, 3 \times \mathrm{R}_1,$ and $9 \times \mathrm{R}_1$ with $D \times L_x = 0.5 \times \mathrm{R}_1$. These choices are taken for the sake of simplicity. The findings discussed in the following can easily be verified also for the other charge distributions shown in Fig. 4.8. The resulting profiles for the electrostatic potential Ψ are shown in Fig. 4.10. Here the data are shown together with the asymptotic Debye decay (red solid lines) and with the results for the same boundary conditions $\sigma(\boldsymbol{s})$, but obtained within the framework of Chap. 3, i.e., Ref. [6] (black lines).

First, I note the offset between the three profiles, which is due to the fact, that the net charge differs for the three displayed cases. Here, however, the potential Ψ is reduced with respect to the amplitude $\sigma_{\max}$ only. If one accounts for the different net charges as well by determining the averaged charge and reducing Ψ with respect to the averaged surface charge σ_{av} instead of the maximum charge $\sigma_{\max}$, all three cases render the same asymptotic profile. Second, the wavelength λ of the surface charge pattern $\sigma(\boldsymbol{s})$ strongly influences the behavior of the potential Ψ close to the wall. With increasing wavelength, the potential exhibits a strong dependence on the lateral position, as can be inferred from the range of potential values at $z = 0$. Also, the decay length of the electrostatic potential close to the wall strongly increases with increasing wavelength λ. Far away from the wall all three cases clearly match the predictions of an exponential decay with the decay length given by the Debye length κ^{-1}. Finally, the comparison with the results calculated along the lines proposed in Chap. 4 and Ref. [6] again reveals remarkable agreement, at least for the two larger wavelengths. The results of the calculation within the framework of Chap. 3 and Ref. [6], respectively, are obtained in the middle of one of the charged areas. Therefore, they should follow the highest values of the data obtained from the calculations of the present study. This can easily be verified. The reason for the discrepancy in the case of the smaller wavelength $\lambda = 1 \times \mathrm{R}_1$ can be found by comparison with the situation discussed in Sec. 4.3.2. In that section I found a clear change in the behavior of the electrostatic potential Ψ for high wall charges, where the fluid reaction becomes nonlinear. In Fig. 4.10, the effective surface charges of the three cases lie around this transition, with the case $\lambda = 9 \times \mathrm{R}_1$ still being in the linear regime, the case $\lambda = 1 \times \mathrm{R}_1$ being in the nonlinear regime, and the case $\lambda = 3 \times \mathrm{R}_1$ being very close to the transition. Due to that, I find very good agreement for the largest of the wavelengths and increasing deviations for decreasing wavelengths. Especially for the smallest wavelength, $\lambda = 1 \times \mathrm{R}_1$, one is clearly in the nonlinear regime, which indicates the failure of the model used in Chap. 3 and Ref. [6] (see Fig. 4.4 in Sec. 4.3.2).

Finally, I take a closer look at the decay of the electrostatic potential Ψ for the wavelength of $\lambda = 9 \times \mathrm{R}_1$. In Fig. 4.11, the asymptotic behavior of the electrostatic

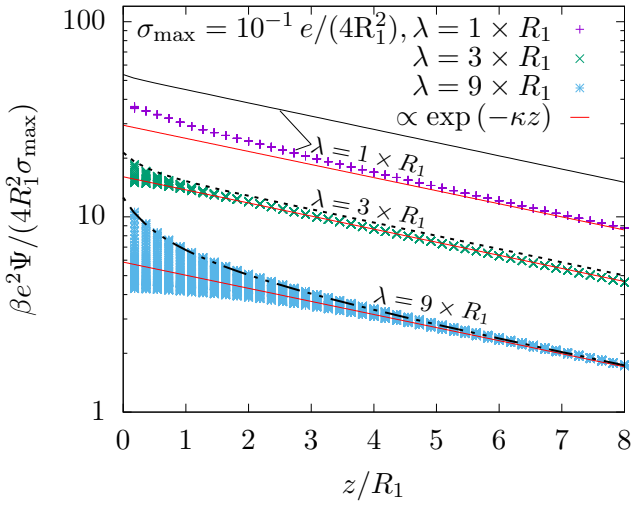

Figure 4.10: Scaled electrostatic potential Ψ as a function of the distance z from the wall for all lateral positions $\boldsymbol{s}$ studied for three wavelengths $\lambda = 1 \times \mathrm{R}_1, 3 \times \mathrm{R}_1$, and $9 \times \mathrm{R}_1$ of the wall charge distribution; here it is a pulse wave-like charge distribution (see Fig. 4.8 (b) and Eq. (4.19)). The duty cycle D, i.e., the dimensionless width of the charged stripe, remains the same ($DL_x = 0.5 \times \mathrm{R}_1$) for all three cases. Similar to Fig. 4.7, the region covered by the spread of the data is due to different lateral positions being shown for the same distance from the wall. Again, this gives information about the strength and the range of lateral variations of the electrostatic potential. However, in contrast to the potentials shown in Fig. 4.7, here the wall carries a net charge. This is the reason for the visible long-ranged decay, which corresponds to the exponential decay of the associated net charge with a decay length equal to the corresponding Debye length κ^{-1} (see Eq. (4.20)). This decay behavior far from the wall occurs for all three cases. However, close to the wall there is a much more complicated decay behavior, which strongly depends on the wavelength of the surface charge pattern. As in previous graphs, the black lines correspond to the results for the same calculations within the framework of Chap. 3 (Ref. [6]). For the two longer wavelengths, $\lambda = 3 \times \mathrm{R}_1$ and $9 \times \mathrm{R}_1$, these results again match the present ones very well. The deviation occurring for the shortest wavelength is due to the fact, that this case is outside the linear response regime (see Sec. 4.3.2).

potential

$$\Psi_{\mathrm{av}} \propto \exp(-\kappa z), \tag{4.20}$$

caused by a nonvanishing average charge σ_{av} of the surface with κ as the Debye length, is subtracted from the data to study shorter ranged contributions to the behavior of the potential close to the wall. As given in Eq. (4.18), the theoretical predictions from Chap. 3, i.e., Ref. [6] for a linear response approximation hints at a decay with a decay length depending on the wavenumber $q_{\parallel}$ of the surface charge pattern $\sigma(\boldsymbol{s})$. In fact, there are multiple further exponential decays involved, all of which depend on the wavenumber; Eq. (4.18) represents only the next smaller (to $1/\kappa$) length scale of the decay of the potential. This prediction is shown as a green solid line in Fig. 4.11. Again, I also include the results given by Chap. 3 (Ref. [6]) for the same surface charge distribution (blue circles). The various data points for the same distance z correspond to different lateral positions. Close to the wall, the potential Ψ exhibits a faster decay than the one given by the displayed prediction (green line), which agrees with the expected occurrence of further short-ranged decays influencing the behavior in close proximity to the wall. However, within the intermediate range of distances from the wall ($6 \times \mathrm{R}_1 \gtrsim z \gtrsim 2 \times \mathrm{R}_1$), the data closely follow the lowest order predictions from Chap. 3 (Ref. [6]). The present data clearly shows an exponential decay, with the decay indeed given by Eq. (4.18). Nevertheless, even upon closer examination, our findings match remarkably well with the full corresponding results from Chap. 3 (see Ref. [6]) (blue dots).

Finally, I compare the previously discussed surface charge patterns with respect to the surface contribution (see Refs. [124, 125])

$$\Omega_S = \frac{\Omega^{\mathrm{eq}} + pV}{A} \tag{4.21}$$

of the grand potential Ω^{eq}, where p is the bulk pressure, $V = |\mathcal{V}|$ is the size of the system, and $A = |\partial\mathcal{V}|$ is the area of the charged wall. Note that the quantity Ω_S, which has the dimension of energy per area, is sometimes called "surface tension", whereas some authors decompose it into the surface tension of a uniform wall, the line tension, etc. $\Omega_S A$ measures the cost of free energy to create an area A with the respective surface charge pattern. The resulting values for the various configurations of the wall charge are shown in Fig. 4.12. There, the surface contributions Ω_S are shown for a surface charge amplitude of $\sigma_{\max} = 10^{-1}\, e/(4\mathrm{R}_1^2)$, or $\sigma = 10^{-1}\, e/(4\mathrm{R}_1^2)$ for the constant wall charge, respectively. For smaller wall charge amplitudes, there is no significant effect visible. For the shown strength of the surface charge, however, there are some interesting features. First, the surface contribution Ω_S for the constant surface charge distribution is much higher than

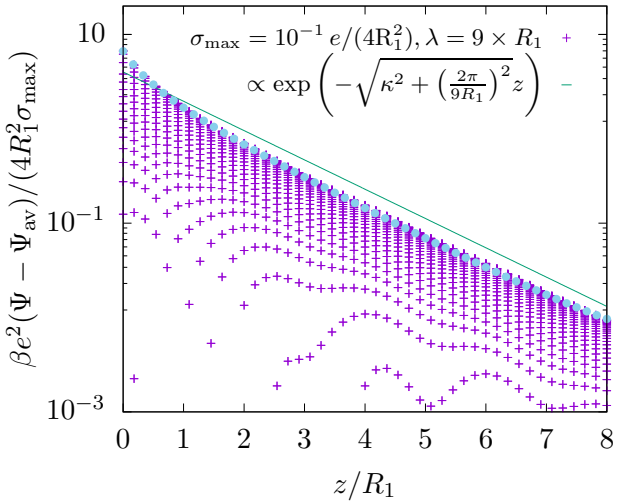

Figure 4.11: Electrostatic potential Ψ reduced by the surface charge amplitude $\sigma_{\max}$ as a function of the distance z from the wall for all lateral positions $\boldsymbol{s}$ studied for the case of an underlying surface charge pattern $\sigma(\boldsymbol{s})$ corresponding to Fig. 4.8 (b) with wavelength $\lambda = 9 \times \mathrm{R}_1$. Since all lateral positions are shown, there are multiple data points for one distance z, leading to the region covered by the spread of the data. Additionally, the asymptotic profile Ψ_{av} with the Debye length $1/\kappa$ as decay length is subtracted from the data in order to gain insight into the next shorter, subdominant length scale involved (see Eq. (4.20)). The green line corresponds to this shorter length scale as it is obtained from Eq. (4.18). Furthermore, the blue circles depict the results for the same system derived via the framework of Chap. 3 (Ref. [6]). Not only do the data follow the theoretical predictions very well, also both data sets match remarkably well, despite large differences in the details of the fluid description.

for all the other cases. Because the overall charge in this case is the highest, this large influence on the structure is understandable. Second, in the case of the sinusoidal wall charge distribution, the surface contribution Ω_S clearly increases with the wavelength of the surface structure. This is understandable, too, because the lateral variation of, e.g., the electrostatic potential, and also the range of this variation normal to the surface, becomes more pronounced for increasing wavelengths (see Figs. 4.7 and 4.10), which reflects the influence of the surface on the fluid. Thus, the surface contribution Ω_S increases for larger wavelengths. This effect, however, seems to be reversed if the surface is arranged as shown in Fig. 4.8(b), i.e., as a striped pattern. For this case Fig. 4.12 indicates, that the surface contribution Ω_S decreases for increased wavelengths. However, in contrast to the sinusoidal charge pattern, the striped pattern carries an average charge, which increases with decreasing wavelength (DL_x is kept constant, see Fig. 4.12). This competition of increasing range and decreasing average charge leads to the observed behavior. Thus, the surface contribution Ω_S nicely echoes the previous findings, for which the fluid structure

depends on both the average charge of the wall, especially for small scale surface charge patterns (see Fig. 4.9), and the wavelength of the surface charge distribution (see Figs. 4.10 and 4.11).

The observed dependence also provides information about the solubility of particles carrying a surface charge. As mentioned above, the surface contribution $\Omega_S A$ measures the cost of free energy to form an interface of area A. Therefore, large surface contributions lead to weak solubilities, because creating the interface is energetically costly. The planar surface charge patterns studied here can be regarded as surface segments of particles, which are large compared to the fluid constituents, i.e., for which a planar surface is an acceptable approximation. Hence, I find the solubility of such large particles, which carry a surface charge pattern associated with the corresponding surface contribution $\Omega_S A$ (see Fig. 4.12), to vary with the wavelength and the average charge of the pattern.

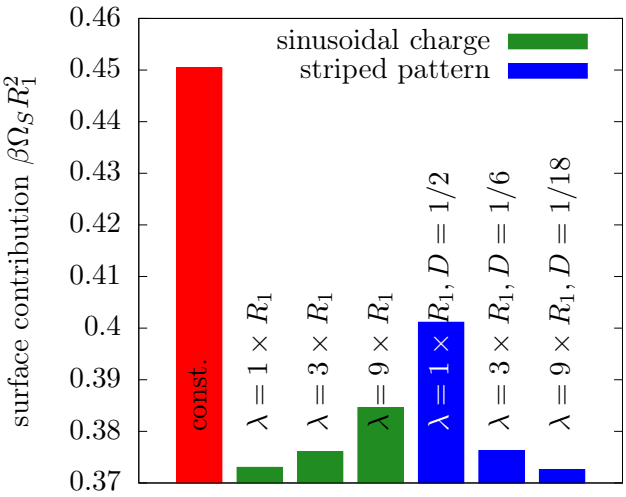

Figure 4.12: Dimensionless surface contribution Ω_S to the grand potential for the different surface charge configurations studied here (see Eq. (4.21)). For all cases, the surface charge amplitude is set to $\sigma_{\max} = 10^{-1}\, e/(4\mathrm{R}_1^2)$, or $\sigma = 10^{-1}\, e/(4\mathrm{R}_1^2)$ for the constant wall charge, respectively. In the case of a purely repulsive hard wall, the surface contribution is $\beta\Omega_S R_1^2 = 0.36972$ (not shown here). For values of the wall charge smaller than the one shown here, the variations of Ω_S are negligibly small. Additionally, for the striped pattern the duty cycle D, i.e., the dimensionless width of the charged stripe, is kept constant ($DL_x = 0.5 \times \mathrm{R}_1$). As the overall charge in the case of the constant wall charge is the highest by far, this case clearly shows the largest surface contribution Ω_S. However, for the other cases with spatially varying surface charge the surface contribution Ω_S depends on the wavelength of the pattern and on the average charge of the wall.

4.4 Conclusions and summary

In the present chapter the effects of surface charge heterogeneities on a nearby electrolyte solution have been investigated with respect to the density profiles of all three fluid components and the electrostatic potential inside the system. The fluid comprises a neutral solvent and a single univalent salt component. They are treated explicitly as hard spheres by means of classical density functional theory within the framework of fundamental measure theory, which has been proven to be a powerful approach to study fluid structures in terms of number density profiles [46, 57, 73, 121]. In order to gain further insight into this system, a variety of surface charge patterns has been studied, starting with the case of a homogeneous wall charge distribution (see Sec. 4.3.2). For such homogeneously charged walls I have naturally found no dependence of any of the profiles on the lateral position. For increasing distances from the wall (see Figs. 4.2, 4.3, and 4.4) I have been able to identify an exponential decay on the length scale of the Debye length κ^{-1} for all studied values of the constant surface charge density. Beyond that, the density profiles of the three fluid components are dominated by well-known layering effects caused by the hard sphere nature of all particles. Furthermore, for various wall charge strengths I have identified two regimes of the fluid response. For low surface charges I have found a linear response of the fluid, whereas replacement of solvent particles by counterions leads to nonlinear response phenomena for high surface charge strengths.

In Sec. 4.3.3, replacing the homogeneously charged (and therefore overall charged) wall by a sinusoidal charge distribution (with no overall charge), I have found a strong dependence of both the solute densities and the electrostatic potential on the wavelength of the underlying surface charge pattern (see Figs. 4.6 and 4.7). However, the solvent densities remain de facto unchanged upon a change of the wavelength (see Fig. 4.5). Also, for all studied values, there are no dependences on the amplitude of the surface charge other than a proportionality factor.

Finally, in Sec. 4.3.4 I have studied more complex surface charge structures, combining both aspects discussed above: a nonvanishing net charge of the wall and small-scale heterogeneities of the surface charge distribution (see Fig. 4.8). First, I have found a way to fine tune the behavior of the fluid with respect to the transition between the linear and the nonlinear response regime by adjusting the area fraction of the charged surface and thus effectively tuning the net charge of the wall (see Fig. 4.9). Second, I have found a clear dependence of the decay behavior of the electrostatic potential on the lateral wavelength of the surface charge structure, where longer wavelengths translate into a longer-ranged decay of the potential away from the wall (see Fig. 4.10). This effect, as

well as all other behaviors of the decay of the potential found in the present study can readily be understood on the basis of analytic predictions obtained in the previous Chap. 3 (cf. Ref. [6]), where a connection between the lateral wavelengths and the normal decay behavior has been derived (see Eq. (4.18)). I note, that within the linear regime the predictions of this previous study provide excellent agreements with the present results, despite its much more simplistic fluid description. Finally, I compared the surface charge distributions discussed in the present study in terms of the surface contribution to the grand potential. This confirmed the different influences of the average surface charge as well as of the wavelength of the actual surface charge distribution. Since the strength of the surface contributions is linked directly to the solubility of the corresponding surfaces, our analysis also provides insights into the solubility of large particles carrying a surface charge.

In conclusion, the present study displays a powerful and very flexible approach to study the effect on the density profiles and the electrostatic potential in contact with surfaces with a broad range of possible surface charge heterogeneities. The fully three-dimensional results reveal a strong sensitivity on the overall charge as well as on the detailed shape of the surface pattern.

Building on previous, more simplistic fluid descriptions (Chap. 3, [6]), this framework still can be extended in various ways in order to incorporate more realistic and sophisticated models. First, much more elaborate density functionals have already been used to account for even more reliable fluid descriptions. These provide a starting point for further extensions of the present analysis. For example, analyzing equal particle sizes and low ionic strengths heavily narrows the range of occurrence of important effects, where, e.g., Ref. [145] shows possible ways for studies beyond these restrictions. Second, in the present study, no wetting or bulk phase transitions have been investigated. In the future, the study of such transitions and their influence on the fluid behavior appears to be promising. Finally, the present study has been restricted to periodic surface charge patterns. This is solely done for the sake of simplicity. The investigation of random, disordered surface charge distributions is likely to lead to further interesting effects.

4.A Details of the discretization of the system

In order to tackle the situation described in Sec. 4.2, the system of size $L_x \times L_y \times L_z$ is divided in N_x, N_y, and N_z cells in the respective directions of space. Each cell is of size $|\mathcal{C}^*| = \Delta_x^* \times \Delta_y^* \times \Delta_z^*$ with

$$\Delta_i^* = \frac{L_i}{N_i} = \frac{P_i R_1}{N_i}, \tag{4.22}$$

where Δ_i^* is the resolution of the numeric calculations with $i \in \{x, y, z\}$, and P_i is the length in units of the particle radius R_1. Consequently, $\Delta_i = \frac{P_i}{N_i}$ is the dimensionless resolution and $|\mathcal{C}| = \Delta_x \times \Delta_y \times \Delta_z$ the dimensionless cell size. With this division into cells, the position dependence can be captured by indices, which denote the respective cell. E.g., $\varrho_{i,j,k}^{(\alpha)}$ describes the density of particle species $\alpha \in \{1, 2, 3\}$ in the cell located at the interval $(i\Delta_x, (i+1)\Delta_x] \times (j\Delta_y, (j+1)\Delta_y] \times (k\Delta_z, (k+1)\Delta_z]$. Let me note that — in contrast to $q, \boldsymbol{\varrho} = (\varrho_1, \varrho_2, \varrho_3)$, and ε_r — the electrostatic potential Ψ is defined at the corners of the cells, i.e., $\Psi_{i,j,k}$ is the electrostatic potential at the point $(i\Delta_x, j\Delta_y, k\Delta_z)$. This leads to the discrete version of the Euler-Lagrange equations (see Eq. (4.15))

$$\ln \varphi_{i,j,k}^{(\alpha)} = \mu_\alpha^* - \sum_{a,b,c,\beta} p_\beta \frac{\partial \Phi}{\partial n_{a,b,c}^{(\beta)}} \omega_\alpha^{(\beta)}(a-i, b-j, c-k) + \frac{\partial \beta \mathcal{E}}{\partial \varphi_{i,j,k}^{(\alpha)}}. \tag{4.23}$$

Here, $\varphi^{(\alpha)} = |\mathcal{C}^*|\varrho_\alpha$ is the dimensionless density of species α, $\mu_\alpha^* = \beta\mu_\alpha - \ln(\Lambda_\alpha^3/|\mathcal{C}^*|)$ is the corresponding dimensionless effective chemical potential, and the prefactor is $p_\beta = -1$ for vectorial weights $\boldsymbol{\omega}^{(\beta)}$ and $p_\beta = 1$ for scalar weights. The three terms result from the ideal gas contribution, the FMT contribution, and the electrostatic interactions, respectively.

4.B Derivation of the expression for the electrostatic field energy

As illustrated, e.g., in Ref. [144], one possible way of determining the equilibrium form $\Psi(\boldsymbol{r})$ of $\psi(\boldsymbol{r})$ in Eq. (4.11) is a variational approach. Along these lines I introduce

$$\mathcal{E}[\psi, q, \varepsilon_r, \sigma] = \int_{\mathcal{V}} \mathrm{d}^3 r \, \left(\frac{\varepsilon_0 \varepsilon_r(\boldsymbol{r})}{2} (\nabla\psi(\boldsymbol{r}))^2 - q(\boldsymbol{r})\psi(\boldsymbol{r}) \right) - \int_{\partial\mathcal{V}} \mathrm{d}^2 s \, \sigma(\boldsymbol{s})\psi(\boldsymbol{s}, 0), \tag{4.24}$$

where $q(\boldsymbol{r}) = e(\varrho_2(\boldsymbol{r}) - \varrho_3(\boldsymbol{r}))$ is the local charge density, and $\sigma(\boldsymbol{s})$ is the surface charge density at the wall $\partial\mathcal{V} = \{\boldsymbol{r} \in \mathbb{R}^3 | \boldsymbol{r} = (\boldsymbol{s}, z = 0) = (x, y, 0)\}$. Furthermore, the equilibrium

distribution of the electrical potential Ψ has to fulfill the Poisson equation

$$\nabla(-\varepsilon_0\varepsilon_r(\boldsymbol{r})\nabla\Psi(\boldsymbol{r})) = q(\boldsymbol{r}) \tag{4.25}$$

with the boundary condition corresponding to the slope at the wall. This is represented by

$$\varepsilon_0\varepsilon_r(\boldsymbol{s},0)\boldsymbol{n}(\boldsymbol{s},0)\cdot\nabla\Psi(\boldsymbol{s},0) = \sigma(\boldsymbol{s}), \tag{4.26}$$

where $\boldsymbol{n}(\boldsymbol{s},0) = -\boldsymbol{e}_z$ is the outer normal vector at $\boldsymbol{r} = (\boldsymbol{s},0)$. The boundary condition corresponding to a homogeneous bulk system far from the wall is represented by

$$\Psi(\boldsymbol{s},\infty) = 0. \tag{4.27}$$

Provided the correct potential Ψ has been found, $\mathcal{E}$ can be rewritten as

$$\begin{aligned}
\mathcal{E}[\Psi,q,\varepsilon_r,\sigma] &= \int_{\mathcal{V}} \mathrm{d}^3r \left(\frac{\varepsilon_0\varepsilon_r(\boldsymbol{r})}{2}(\nabla\Psi(\boldsymbol{r}))^2 - q(\boldsymbol{r})\Psi(\boldsymbol{r})\right) - \int_{\partial\mathcal{V}} \mathrm{d}^2s\ \sigma(\boldsymbol{s})\Psi(\boldsymbol{s},0) \\
&\overset{(4.25)}{=} \int_{\mathcal{V}} \mathrm{d}^3r \left(\frac{\varepsilon_0\varepsilon_r(\boldsymbol{r})}{2}(\nabla\Psi(\boldsymbol{r}))^2 - \nabla(-\varepsilon_0\varepsilon_r(\boldsymbol{r})\nabla\Psi(\boldsymbol{r}))\Psi(\boldsymbol{r})\right) \\
&\quad - \int_{\partial\mathcal{V}} \mathrm{d}^2s\ \sigma(\boldsymbol{s})\Psi(\boldsymbol{s},0) \\
&\overset{\text{p.i.}}{=} \int_{\mathcal{V}} \mathrm{d}^3r \left(-\frac{\varepsilon_0\varepsilon_r(\boldsymbol{r})}{2}(\nabla\Psi(\boldsymbol{r}))^2\right) - \int_{\partial\mathcal{V}} \mathrm{d}^2s \left[(\varepsilon_0\varepsilon_r(\boldsymbol{s},0)\boldsymbol{n}(\boldsymbol{s},0)\cdot\nabla\Psi(\boldsymbol{s},0))\cdot\right. \\
&\quad \left.\Psi(\boldsymbol{s},0)\right] - \int_{\partial\mathcal{V}} \mathrm{d}^2s\ \sigma(\boldsymbol{s})\Psi(\boldsymbol{s},0) \\
&\overset{(4.26)}{=} \int_{\mathcal{V}} \mathrm{d}^3r \left(-\frac{\varepsilon_0\varepsilon_r(\boldsymbol{r})}{2}(\nabla\Psi(\boldsymbol{r}))^2\right),
\end{aligned} \tag{4.28}$$

leading to

$$\beta U_{\mathrm{el.}}[\boldsymbol{\varrho}] = -\beta\mathcal{E}[\Psi,q,\varepsilon_r,\sigma]. \tag{4.29}$$

Therefore, given the correct potential $\Psi(\boldsymbol{r})$ for the given charge distribution $q(\boldsymbol{r})$, the electrostatic contribution to the density functional can be expressed via $\mathcal{E}[\Psi,q,\varepsilon_r,\sigma]$.

4.C Minimization of the auxiliary functional $\mathcal{E}$

The auxiliary functional $\mathcal{E}$, which is introduced in Eqs. (4.13) and (4.24), respectively, is constructed in a way, that its variation with respect to the electrostatic potential ψ is vanishing for the equilibrium potential distribution $\psi = \Psi$ due to the Poisson equation

(4.25) and its boundary conditions:

$$\begin{aligned}
\delta\mathcal{E} &= \int_{\mathcal{V}} \mathrm{d}^3 r \ (\varepsilon_0 \varepsilon_r(\boldsymbol{r}) \nabla\psi(\boldsymbol{r})(\nabla\delta\psi) - q(\boldsymbol{r})\delta\psi) - \int_{\partial\mathcal{V}} \mathrm{d}^2 s \ \sigma(\boldsymbol{s})\delta\psi + \mathcal{O}(\delta q, \delta\varepsilon_r) \\
&= \int_{\mathcal{V}} \mathrm{d}^3 r \ (\nabla(\varepsilon_0 \varepsilon_r(\boldsymbol{r}) \nabla\psi(\boldsymbol{r})\delta\psi) - \varepsilon_0 \nabla\cdot(\varepsilon_r(\boldsymbol{r})\nabla\psi)\delta\psi - q(\boldsymbol{r})\delta\psi) - \int_{\partial\mathcal{V}} \mathrm{d}^2 s \ \sigma(\boldsymbol{s})\delta\psi + \dots \\
&= \int_{\mathcal{V}} \mathrm{d}^3 r \ ((-\varepsilon_0 \nabla\cdot(\varepsilon_r(\boldsymbol{r})\nabla\psi) - q(\boldsymbol{r}))\delta\psi) + \int_{\partial\mathcal{V}} \mathrm{d}^2 s \ ((\varepsilon_0 \varepsilon_r(\boldsymbol{s},0)\boldsymbol{n}(\boldsymbol{s},0)\cdot\nabla\psi - \sigma(\boldsymbol{s}))\delta\psi) \\
&\quad + \dots \\
&\overset{(4.25)}{\underset{(4.26)}{=}} 0 \times \delta\psi + \mathcal{O}(\delta q, \delta\varepsilon_r).
\end{aligned} \tag{4.30}$$

From this it follows, that for a given and fixed distribution of particles and therefore for a given and fixed charge distribution q and permittivity ε_r, the minimum of $\mathcal{E}$ is reached for $\psi = \Psi$, i.e., the equilibrium potential can be found by a simple minimization of $\mathcal{E}$. This in turn leads to three types of Euler-Lagrange equations, depending on the distance from the wall, which can be rewritten as

$$\begin{aligned}
\Psi_{i,j,0} = &\left[2\left(\frac{1}{\Delta_x^2}+\frac{1}{\Delta_y^2}+\frac{1}{\Delta_z^2}\right)\sum_{\alpha,\beta\in\{0,1\}} \varepsilon_{r;i-\alpha,j-\beta,0}\right]^{-1} \cdot \Bigg(\sum_{\alpha,\beta\in\{0,1\}} \varepsilon_{r;i-\alpha,j-\beta,0}\Bigg[\frac{1}{\Delta_x^2}[2\Psi_{i+1-2\alpha,j,0} \\
&+ (\Psi_{i+1-2\alpha,j+1-2\beta,0} - \Psi_{i,j+1-2\beta,0}) + (\Psi_{i+1-2\alpha,j,1} - \Psi_{i,j,1}) + \frac{1}{2}(\Psi_{i+1-2\alpha,j+1-2\beta,1} \\
&- \Psi_{i,j+1-2\beta,1})] + \frac{1}{\Delta_y^2}[2\Psi_{i,j+1-2\beta,0} + (\Psi_{i+1-2\alpha,j+1-2\beta,0} - \Psi_{i+1-2\alpha,j,0}) \\
&+ (\Psi_{i,j+1-2\beta,1} - \Psi_{i,j,1}) + \frac{1}{2}(\Psi_{i+1-2\alpha,j+1-2\beta,1} - \Psi_{i+1-2\alpha,j,1})\Bigg] + \frac{1}{\Delta_z^2}[2\Psi_{i,j,1} \\
&+ (\Psi_{i+1-2\alpha,j,1} - \Psi_{i+1-2\alpha,j,0}) + (\Psi_{i,j+1-2\beta,1} - \Psi_{i,j+1-2\beta,0}) + \frac{1}{2}(\Psi_{i+1-2\alpha,j+1-2\beta,1} \\
&- \Psi_{i+1-2\alpha,j+1-2\beta,0})]] + \frac{\chi}{|\mathcal{C}|}\sum_{\alpha,\beta\in\{0,1\}} q_{i-\alpha,j-\beta,0} + 2\frac{\chi}{|\mathcal{C}|}\sum_{\alpha,\beta\in\{0,1\}} \sigma_{i-\alpha,j-\beta}\Bigg),
\end{aligned} \tag{4.31}$$

$$
\begin{aligned}
\Psi_{i,j,0<k<N_z} = & \left[2\left(\frac{1}{\Delta_x^2}+\frac{1}{\Delta_y^2}+\frac{1}{\Delta_z^2}\right) \sum_{\alpha,\beta,\gamma\in\{0,1\}} \varepsilon_{r;i-\alpha,j-\beta,k-\gamma} \right]^{-1} \cdot \Bigg(\sum_{\alpha,\beta,\gamma\in\{0,1\}} \varepsilon_{r;i-\alpha,j-\beta,k-\gamma} \cdot \\
& \left[\frac{1}{\Delta_x^2} \left[2\Psi_{i+1-2\alpha,j,k} + (\Psi_{i+1-2\alpha,j+1-2\beta,k} - \Psi_{i,j+1-2\beta,k}) + (\Psi_{i+1-2\alpha,j,k+1-2\gamma} \right. \right. \\
& \left. \left. - \Psi_{i,j,k+1-2\gamma}) + \frac{1}{2}(\Psi_{i+1-2\alpha,j+1-2\beta,k+1-2\gamma} - \Psi_{i,j+1-2\beta,k+1-2\gamma}) \right] + \frac{1}{\Delta_y^2} \cdot \right. \\
& \left[2\Psi_{i,j+1-2\beta,k} + (\Psi_{i+1-2\alpha,j+1-2\beta,k} - \Psi_{i+1-2\alpha,j,k}) + (\Psi_{i,j+1-2\beta,k+1-2\gamma} \right. \\
& \left. - \Psi_{i,j,k+1-2\gamma}) + \frac{1}{2}(\Psi_{i+1-2\alpha,j+1-2\beta,k+1-2\gamma} - \Psi_{i+1-2\alpha,j,k+1-2\gamma}) \right] \\
& + \frac{1}{\Delta_z^2} \left[2\Psi_{i,j,k+1-2\gamma} + (\Psi_{i+1-2\alpha,j,k+1-2\gamma} - \Psi_{i+1-2\alpha,j,k}) + (\Psi_{i,j+1-2\beta,k+1-2\gamma} \right. \\
& \left. \left. - \Psi_{i,j+1-2\beta,k}) + \frac{1}{2}(\Psi_{i+1-2\alpha,j+1-2\beta,k+1-2\gamma} - \Psi_{i+1-2\alpha,j+1-2\beta,k}) \right] \right] \\
& + \frac{\chi}{|\mathcal{C}|} \sum_{\alpha,\beta,\gamma\in\{0,1\}} q_{i-\alpha,j-\beta,k-\gamma} \Bigg),
\end{aligned}
\tag{4.32}
$$

$$
\begin{aligned}
\Psi_{i,j,N_z} = & \left[2\left[\left(\frac{1}{\Delta_x^2}+\frac{1}{\Delta_y^2}+\frac{1}{\Delta_z^2}\right) + \frac{\kappa R_1}{\Delta_z} \right] \sum_{\alpha,\beta\in\{0,1\}} \varepsilon_{r;i-\alpha,j-\beta,N_z-1} \right]^{-1} \cdot \Bigg(\sum_{\alpha,\beta\in\{0,1\}} \varepsilon_{r;i-\alpha,j-\beta,N_z-1} \cdot \\
& \left[\frac{1}{\Delta_x^2} \left[2\Psi_{i+1-2\alpha,j,N_z} + (\Psi_{i+1-2\alpha,j+1-2\beta,N_z} - \Psi_{i,j+1-2\beta,N_z}) + (\Psi_{i+1-2\alpha,j,N_z-1} \right. \right. \\
& \left. \left. - \Psi_{i,j,N_z-1}) + \frac{1}{2}(\Psi_{i+1-2\alpha,j+1-2\beta,N_z-1} - \Psi_{i,j+1-2\beta,N_z-1}) \right] + \frac{1}{\Delta_y^2} \left[2\Psi_{i,j+1-2\beta,N_z} \right. \right. \\
& \left. \left. + (\Psi_{i+1-2\alpha,j+1-2\beta,N_z} - \Psi_{i+1-2\alpha,j,N_z}) + (\Psi_{i,j+1-2\beta,N_z-1} - \Psi_{i,j,N_z-1}) \right. \right. \\
& \left. \left. + \frac{1}{2}(\Psi_{i+1-2\alpha,j+1-2\beta,N_z-1} - \Psi_{i+1-2\alpha,j,N_z-1}) \right] + \frac{1}{\Delta_z^2} \left[2\Psi_{i,j,N_z-1} + (\Psi_{i+1-2\alpha,j,N_z-1} \right. \right. \\
& \left. \left. - \Psi_{i+1-2\alpha,j,N_z}) + (\Psi_{i,j+1-2\beta,N_z-1} - \Psi_{i,j+1-2\beta,N_z}) \right. \right. \\
& \left. \left. + \frac{1}{2}(\Psi_{i+1-2\alpha,j+1-2\beta,N_z-1} - \Psi_{i+1-2\alpha,j+1-2\beta,N_z}) \right] \right] + \frac{\chi}{|\mathcal{C}|} \sum_{\alpha,\beta\in\{0,1\}} q_{i-\alpha,j-\beta,N_z-1} \\
& - \frac{\kappa R_1}{\Delta_z} \sum_{\alpha,\beta\in\{0,1\}} \varepsilon_{r;i-\alpha,j-\beta,N_z-1} (\Psi_{i+1-2\alpha,j,N_z} + \Psi_{i,j+1-2\beta,N_z} + \frac{1}{2}\Psi_{i+1-2\alpha,j+1-2\beta,N_z}) \Bigg).
\end{aligned}
\tag{4.33}
$$

Besides the dimensionless resolutions Δ_i, the dimensionless cell volume $|\mathcal{C}|$, the solvent particle radius R_1, and the Debye length $1/\kappa$, the parameter $\chi = \frac{9\pi l_{\mathrm{B}0}}{R_1}$ with the vacuum Bjerrum length $l_{\mathrm{B}0}$ is introduced here.

Chapter 5

Conclusions and outlook

The goal of this dissertation was to study the behavior of electrolyte solutions adjacent to inhomogeneous surfaces. Two different approaches within the framework of density functional theory were used to analyze this behavior in terms of number density profiles of the fluid components. Specifically, all three types of particles contained in the electrolyte solution, the neutral solvent and two types of monovalent ions, were studied. The main focus of the research was on the influence of heterogeneous distributions of interaction sites on the surface of the substrate.

In Chap. 3, a basic, plain model was used with the goal of deriving closed-form analytical expressions. An electrolyte solution far from any bulk or wetting phase transition was modeled within the framework of density functional theory using a Cahn-Hilliard-like square gradient approximation (see Chap. 3.2.2). Nonelectrostatic interactions between all three fluid components considered, the solvent and the ionic particles, were modeled by a square-well pair potential (see Chap. 3.3.1), all electrostatic interactions were treated on a mean field level via the electrostatic field energy. The electrolyte solution was then assumed to be in contact with a chemically and electrostatically heterogeneous wall, and four exemplary types of walls were studied. First, δ-like, isolated interaction sites were analyzed in Sec. 3.3.3. Both types of interactions between wall and fluid particles were studied. In the case of attractive nonelectrostatic interactions, where the wall directly interacted only with the solvent particles, the solvent density consequently increased. This density variation decayed on the length scale of the bulk correlation length ξ (see Figs. 3.2, 3.3, and 3.4). Furthermore, the change of the solvent density also led to changes in the ion densities, which were proportional to the increase of the solvent density. In contrast to this finding, the density of the solvent remained unchanged when analyzing electrostatic δ-like interaction sites. This effect is a result of the model used here, in which the deviations in the solvent density induced by the two types of ions even out

because of symmetry reasons. The changes in the ion densities for this case of electrostatic interactions, however, were of much longer range than in the nonelectrostatic case. Here, the ion density deviations decayed on a length scale given by the Debye length $1/\kappa \gg \xi$. Nevertheless, the density deviations of the ions decayed exponentially on this longer length scale (see Fig. 3.5). To analyze the influence of competing length scales, another length scale in the form of the size of a circular region of interaction was introduced in Sec. 3.3.4. The analysis of such an interaction site of nonvanishing extent revealed, that the resulting density profiles were very sensitive to the dominant length scale. For bulk length scales (Debye length $1/\kappa$, bulk correlation length ξ) dominating the systems studied, the density profiles closely resembled the ones found for the δ-like interactions. On the other hand, if the system was dominated by a length scale set by the boundary conditions at the wall, the lateral density deviations closely resembled the structures of the corresponding boundary condition. For intermediate regimes, where the external length scales set by the boundary conditions on the wall and the internal length scales set by the correlation lengths competed, a transition between the two extremes was observed (see Fig. 3.7). Finally, the first model was used to study the influence of multiple interaction sites, arranged as a regular hexagonal lattice, on the adjacent fluid (see Sec. 3.3.5). Here, again the size of the interaction sites was found to influence the amplitude of the observed density deviations (see Fig. 3.8). In addition, the distance between the interaction sites shaped the response of the density profiles, particularly with respect to the influence of variation of the lateral wave number $|\boldsymbol{q}_{\parallel}|$. Despite its simplicity, this first model still proved very versatile in studying different types and shapes of boundary conditions.

To gain more insights into the behavior and enhance the precision of the analysis of electrolyte solutions in contact with heterogeneously patterned substrates, the density functional approach used in Chap. 4 was considerably refined. Building on the results and also on potential shortcomings of the first method (Chap. 3), the density functional description was amended in several ways, including lifting the restriction to a linear response regime and accounting for the previously neglected finite size of the fluid constituents. To this end, the methods of fundamental measure theory were incorporated into the density functional approach (see Sec. 4.2). In a first step, the resulting hard sphere fluid was placed near a homogeneously charged wall (Sec. 4.3.2). For this homogeneous wall charge distribution, the profiles obviously showed no lateral variation, but, confirming results from the simple approach of Chap. 3, the observed density deviations showed an exponential decay with increasing distances from the substrate, where the decay length was again given by the Debye length $1/\kappa$. In addition to this exponential decay, however, the expected layering structure caused by the hard sphere nature of the fluid particles dom-

inated the density profiles close to the hard substrate. Analyzing the resulting density profiles for the homogeneously charged wall, two regimes of qualitatively different fluid responses were found. For low surface charges there was a linear response of the fluid, with the amplitude of the surface charge being merely a proportionality factor. Higher surface charges, however, led to extrusion of the solvent particles and therefore to nonlinear response phenomena (see Figs. 4.2, 4.3, and 4.4). Introducing lateral variation of the surface charge distribution in the form of a sinusoidal charge distribution in Sec. 4.3.3 had a strong influence on impact of the surface pattern. In addition to the amplitude of the surface charge, which had no effects other than being a proportionality factor, both ion densities and the profile of the electrostatic potential strongly varied in dependence from the lateral wavelength of the underlying surface charge pattern (see Figs. 4.6 and 4.7). However, due to the vanishing overall charge of the wall for this charge distribution, the solvent densities remained de facto unchanged upon a change of wavelength or amplitude (see Fig. 4.5). As a final step in Sec. 4.3.4, the model derived in Sec. 4.2 was used to study various more complex surface charge structures. In this section the surface charge distributions considered combined both, a nonvanishing net charge of the substrate and small-scale heterogeneities (see Fig. 4.8). Within these structures, two main effects were observed. First, studying different structures varying in area fraction of the charged surface and thus average charge, revealed that this average charge is the only relevant parameter in the case of small scale heterogeneities (see Fig. 4.9). Second, the decay of, e.g., the electrostatic potential strongly depended on the lateral wavelengths of the structure of the surface charge. Longer wavelengths of the surface charge pattern translated into longer-ranged decays of the potential away from the wall and longer wavelengths also led to a greater heterogeneity of the electrostatic potential close to the wall. Notably, the predictions derived from the simple model described in Chap. 3 were successful in explaining the behavior of the electrostatic potential for this much more complex case (see Figs. 4.10 and 4.11). Nevertheless, clear limitations of the simple model from Chap. 3 became obvious, when the applied boundary conditions led to nonlinear responses of the electrolyte solution.

In conclusion, the approaches used in this dissertation to study the behavior of an electrolyte solution near a heterogeneously charged wall proved to be flexible and versatile in determining the influence of a broad range of surface configurations. Furthermore, the results of these studies in terms of density and potential profiles, which were sensitive to the surface charge structure, demonstrated the importance of considering inhomogeneities in the surface charge distribution when analyzing the effects of charged walls on electrolyte solutions.

Finally, with regard to future exploration in this area, the results of this dissertation

suggest some obvious starting points. I will briefly highlight some promising applications and expansions of the research presented in this thesis. First, the systems studied here have been restricted mostly to periodic or spatially limited surface charge structures. This was solely done for the sake of simplicity, because particularly the fully three-dimensional calculations in Chap. 4 are computationally costly. However, lifting these restrictions by investigating, for example, random, disordered surface charges appears highly likely to provide insights into a variety of additional interesting effects, e.g., long-ranged disorder effects, anti-fragility (see Ref. [132]). The same applies to the context of introducing additional substrates and revisiting the work of, e.g., [113, 114], among others, with respect to forces between two substrates mediated by an enclosed electrolyte solution. Second, in both approaches considered here, the effects of both bulk and wetting transitions were neglected, assuming the fluid to be far away from any phase transitions. In future research, the investigation of such transitions and their potential effects on the behavior of the fluid could be rewarding. Previous studies (e.g., [154]) already demonstrated, that the presence of charges changes the wetting behavior drastically. If combined with heterogeneous surface charge properties, this is likely to create a number of interesting phenomena, for example, the occurrence of local wetting transitions and spatially varying wetting properties (see Refs. [155, 156]). Another promising application of the methods presented here would be the analysis of surfaces with not only inhomogeneous interactions with the adjacent fluid, but also with geometric inhomogeneities (cf. [157, 158]). The interplay of various heterogeneities competing for influence may lead to further, unexpected effects. One can also imagine, that introducing multiple different length scales in the form of more complex boundary conditions could provide ways to synthesize and structure macromolecules. Again, also the introduction of multiple interacting surfaces appears promising (see, e.g., [113, 114]). Furthermore, the research presented in this thesis already offered two very distinct versions of describing an electrolyte solution with respect to the degree of complexity of the model applied. Both methods could be extended in various ways in order to gain more accurate characterizations of the fluid and its internal structure. For example, the investigation of equal particle sizes (see Ref. [159]) and the restriction to low ionic strengths narrow the number of important effects, but these limitations could be lifted, e.g., along the lines of Ref. [145]. Also, neglecting any attractive interactions between the fluid components and the constraint of identical interactions between all fluid particles may serve as inspirations for subsequent research. Finally, apart from the static considerations studied in this thesis, it also seems possible to include the framework introduced in this research in dynamic studies of fluids near walls, e.g., in studies of dynamic density functional theory or power functional theory (cf. [160]).

Bibliography

[1] P. Simon and Y. Gogotsi, "Materials for electrochemical capacitors", in *Nanosc. Techn.* (World Scientific, 2010), pp. 320–329.

[2] M. V. Fedorov and A. A. Kornyshev, Chem. Rev. **114**, 2978 (2014).

[3] O. Shirai, S. Kihara, Y. Yoshida, and M. Matsui, J. Electroanal. Chem. **389**, 61 (1995).

[4] O. D. Velev and E. W. Kaler, Langmuir **15**, 3693 (1999).

[5] N. Vogel, *Surface Patterning with colloidal monolayers* (Springer, Berlin, 2012).

[6] M. Mußotter, M. Bier, and S. Dietrich, Soft Matter **14**, 4126 (2018).

[7] M. Mußotter, M. Bier, and S. Dietrich, J. Chem. Phys. **152**, 234703 (2020).

[8] G. A. Tokaty, *A History and Philosophy of Fluid Mechanics* (G. T. Foulis, 1971).

[9] R. A. L. Jones, *Soft Condensed Matter*, Oxford Master Series in Physics (Oxford University Press, Oxford, 2002).

[10] D. F. Young, B. R. Munson, T. H. Okiishi, and W. W. Huebsch, *A Brief Introduction to Fluid Mechanics* (Wiley, 2010).

[11] J. L. Lebowitz and E. M. Waisman, "On the equiliubrium theory of fluids: an introductory overview", in *The liquid state of matter: fluids, simple and complex*, edited by E. Montroll and J. L. Lebowitz (North Holland, Amsterdam, 1982).

[12] D. F. Evans and H. Wennerstrom, *Colloidal domain* (Wiley-Vch, New York, 1999).

[13] H. Geiger and K. Scheel, *Handbuch der Physik, Band I, Geschichte der Physik, Vorlesungstechnik* (Springer, 1926).

[14] D. Bernoulli, *Hydrodynamica: sive de viribus et motibus fluidorum commentarii* (Johannis Reinholdi Dulseckeri, 1738).

[15] H. Schlichting and K. Gersten, *Grenzschicht-Theorie* (Springer, Berlin & Heidelberg, 2006).

[16] G. G. Stokes, Trans. Cambridge Phil. Soc. **8** (1880).

[17] J. Fröhlich, *A Journey Through Statistical Physics: From Foundations to the Quan tum Hall Effect: Selecta of Jürg Fröhlich* (Springer, 2009).

[18] F. Schwabl, *Statistische Mechanik* (Springer, Berlin & Heidelberg, 2000).

[19] F. Reif, *Grundlagen der physikalischen Statistik und der Physik der Wärme* (Walter de Gruyter, 1976).

[20] J. Dalton, Mem. Lit. Phil. Soc. Manchester **5**, 535 (1802).

[21] S. Carnot, *Réflexions sur la puissance motrice du feu*, 26 (Vrin, 1978).

[22] W. Ebeling and I. M. Sokolov, *Statistical thermodynamics and stochastic theory of nonequilibrium systems*, Vol. 8 (World Scientific, 2005).

[23] R. Clausius, Ann. d. Phys. **169**, 481 (1854).

[24] W. Thomson, London, Edinburgh, and Dublin Phil. Mag. J. Sci. **4**, 105 (1852).

[25] H. von Helmholtz, *Über die Erhaltung der Kraft, eine physikalische Abhandlung* (Culture et civilisation, 1847).

[26] J. W. Gibbs, *The collected works of JW Gibbs* (Longmans, Green and Co., New York, 1928).

[27] J. C. Maxwell, London, Edinburgh, and Dublin Phil. Mag. J. Sci. **19**, 19 (1860).

[28] J. Z. Wu, "Density functional theory for liquid structures and thermodynamics", in *Molecular thermodynamics of complex systems*, Vol. 131, edited by Y. Lu, Xiaohua and Hu (Springer, Berlin, 2008).

[29] J. W. Gibbs, in Proc. Am. Ass. Adv. Sci. (1884), pp. 57–58.

[30] J. W. Gibbs, Conn. Acad. III **108**, 1878 (1876).

[31] H.-D. Dörfler, *Grenzflächen und kolloid-disperse Systeme* (Springer, Berlin, 2002).

[32] J. D. der Waals, Z. Phys. Chem. **13**, 657 (1894).

[33] L. Rayleigh, London, Edinburgh, and Dublin Phil. Mag. J. Sci. **33**, 209 (1892).

[34] M. v. Smoluchowski, Ann. d. Phys. **330**, 205 (1908).

[35] J. S. Rowlinson and B. Widom, *Molecular theory of capillarity* (Courier Corporation, 2013).

[36] H. Löwen, J. Phys. Cond. Mat. **14**, 11897 (2002).

[37] E. Schrödinger, Phys. Rev. **28**, 1049 (1926).

[38] L. H. Thomas, in Math. Proc. Cam. Phil. Soc. Vol. 23, 5 (Cambridge University Press, 1927), pp. 542–548.

[39] E. Fermi, Z. Phys. **48**, 73 (1928).

[40] N. H. March, Adv. Phys. **6**, 1 (1957).

[41] J. W. Cahn and J. E. Hilliard, J. Chem. Phys. **28**, 258 (1958).

[42] P. A. M. Dirac, in Math. Proc. Cam. Phil. Soc. Vol. 26, 3 (Cambridge University Press, 1930), pp. 376–385.

[43] H. W. Lewis, Phys. Rev. **111**, 1554 (1958).

[44] P. Hohenberg and W. Kohn, Phys. Rev. **136**, B864 (1964).

[45] W. Kohn and L. J. Sham, Phys. Rev. **140**, A1133 (1965).

[46] R. Evans, "Density functionals in the theory of nonuniform fluids", in *Fundamentals of inhomogeneous fluids*, edited by D. Henderson (Dekker, New York, 1992).

[47] W. Kohn, Reviews of Modern Physics **71**, 1253 (1999).

[48] N. D. Mermin, Phys. Rev. **137**, A1441 (1965).

[49] E. W. Montroll and J. E. Mayer, J. Chem. Phys. **9**, 626 (1941).

[50] H. D. Ursell, in Math. Proc. Cam. Phil. Soc. Vol. 23, 6 (Cambridge University Press, 1927), pp. 685–697.

[51] J. E. Mayer, J. Chem. Phys. **5**, 67 (1937).

[52] T. Morita and K. Hiroike, Prog. Theo. Phys. **23**, 1003 (1960).

[53] T. Morita and K. Hiroike, Prog. Theo. Phys. **25**, 537 (1961).

[54] J. K. Percus and G. J. Yevick, Phys. Rev. **110**, 1 (1958).

[55] J. K. Percus, "The Pair Distribution Function in Classical Statistical Mechanics", in *The Equilibrium Theory of Classical Fluids*, edited by H. L. Frisch and J. L. Lebowitz (W. A. Benjamin Inc., New York, 1964).

[56] C. De Dominicis, J. Math. Phys. **3**, 983 (1962).

[57] R. Evans, Adv. Phys. **28**, 143 (1979).

[58] V. Bongiorno and H. T. Davis, Phys. Rev. A **12**, 2213 (1975).

[59] S. Toxvaerd, J. Chem. Phys. **55**, 3116 (1971).

[60] S. Toxvaerd, Mol. Phys. **26**, 91 (1973).

[61] C. Ebner and W. F. Saam, Phys. Rev. B **12**, 923 (1975).

[62] C. Ebner, W. F. Saam, and D. Stroud, Phys. Rev. A **14**, 2264 (1976).

[63] W. F. Saam and C. Ebner, Phys. Rev. A **15**, 2566 (1977).

[64] R. Roth, J. Phys. Cond. Mat. **22**, 63102 (2010).

[65] J.-P. Hansen and I. R. McDonald, *Theory of Simple Liquids* (Academic Press, Burlington, 2008).

[66] S. Nordholm, M. Johnson, and B. C. Freasier, Aus. J. Chem. **33**, 2139 (1980).

[67] M. Johnson and S. Nordholm, J. Chem. Phys. **75**, 1953 (1981).

[68] P. Tarazona and R. Evans, Mol. Phys. **52**, 847 (1984).

[69] P. Tarazona, Phys. Rev. A **31**, 2672 (1985).

[70] Y. Rosenfeld, Phys. Rev. Lett. **63**, 980 (1989).

[71] Y. Rosenfeld, D. Levesque, and J.-J. Weis, J. Chem. Phys. **92**, 6818 (1990).

[72] E. Kierlik and M. L. Rosinberg, Phys. Rev. A **42**, 3382 (1990).

[73] R. Roth, R. Evans, A. Lang, and G. Kahl, J. Phys. Cond. Mat. **14**, 12063 (2002).

[74] G. A. Mansoori, N. F. Carnahan, K. E. Starling, and T. W. Leland Jr, J. Chem. Phys. **54**, 1523 (1971).

[75] H. Hansen-Goos and R. Roth, J. Phys. Cond. Mat. **18**, 8413 (2006).

[76] T. Bernet, M. M. Piñeiro, F. Plantier, and C. Miqueu, J. Phys. Chem. C **121**, 6184 (2017).

[77] J. Jiang, V. V. Ginzburg, and Z.-G. Wang, Soft Matter **14**, 5878 (2018).

[78] A. A. Kornyshev, J. Phys. Chem. B **111**, 5545 (2007).

[79] H.-J. Butt, K. Graf, and M. Kappl, *Physics and Chemistry of Interfaces* (Wiley, Weinheim, 2008).

[80] J.-P. Hansen and H. Löwen, Ann. Rev. Phys. Chem. **51**, 209 (2000).

[81] J. Wu, T. Jiang, D.-E. Jiang, Z. Jin, and D. Henderson, Soft Matter **7**, 11222 (2011).

[82] H. V. Helmholtz, Ann. d. Phys. **243**, 337 (1879).

[83] R. Parsons and R. Payne, Z. Phys. Chem. **98**, 9 (1975).

[84] D. C. Grahame, J. Am. Chem. Soc. **76**, 4819 (1954).

[85] M. Gouy, J. Phys. Theor. Appl. **9**, 457 (1910).

[86] D. L. Chapman, London, Edinburgh, and Dublin Phil. Mag. J. Sci. **25**, 475 (1913).

[87] G. Gouy, Ann. d. Phys. **9**, 129 (1917).

[88] P. Debye and E. Hückel, Phys. Z. **24**, 185 (1923).

[89] O. Stern, Z. Elektrochem. Ang. Phys. Chem. **30**, 508 (1924).

[90] A. Ciach, J. Mol. Liq. **270**, 138 (2018).

[91] D. N. Card and J. P. Valleau, J. Chem. Phys. **52**, 6232 (1970).

[92] D. M. Heyes, Chem. Phys. **69**, 155 (1982).

[93] G.-W. Wu, M. Lee, and K.-Y. Chan, Chem. Phys. Lett. **307**, 419 (1999).

[94] G. M. Torrie and J. P. Valleau, J. Chem. Phys. **73**, 5807 (1980).

[95] L. Degrève, M. Lozada-Cassou, E. Sánchez, and E. González-Tovar, J. Chem. Phys. **98**, 8905 (1993).

[96] C. N. Patra, J. Phys. Chem. B **113**, 13980 (2009).

[97] D. Gillespie, M. Valiskó, and D. Boda, J. Phys. Cond. Mat. **17**, 6609 (2005).

[98] J. G. Kirkwood, J. Chem. Phys. **2**, 351 (1934).

[99] J. J. Bikerman, London, Edinburgh, and Dublin Phil. Mag. J. Sci. **33**, 384 (1942).

[100] S. Levine and G. M. Bell, J. Phys. Chem. **64**, 1188 (1960).

[101] L. B. Bhuiyan, C. W. Outhwaite, and S. Levine, Chem. Phys. Lett. **66**, 321 (1979).

[102] C. W. Outhwaite, L. B. Bhuiyan, and S. Levine, J. Chem. Soc., Faraday Trans. II **76**, 1388 (1980).

[103] C. W. Outhwaite and L. B. Bhuiyan, J. Chem. Soc., Faraday Trans. II **79**, 707 (1983).

[104] C. W. Outhwaite and L. B. Bhuiyan, J. Chem. Phys. **84**, 3461 (1986).

[105] B. Larsen, J. Chem. Phys. **68**, 4511 (1978).

[106] D. Gillespie, W. Nonner, and R. S. Eisenberg, Phys. Rev. E **68**, 31503 (2003).

[107] D. Andelman and J. F. Joanny, Macromolecules **24**, 6040 (1991).

[108] W. Chen, S. Tan, T.-K. Ng, W. T. Ford, and P. Tong, Phys. Rev. Lett. **95**, 218301 (2005).

[109] W. Chen, S. Tan, Z. Huang, T.-K. Ng, W. T. Ford, and P. Tong, Phys. Rev. E **74**, 21406 (2006).

[110] W. Chen, S. Tan, Y. Zhou, T.-K. Ng, W. T. Ford, and P. Tong, Phys. Rev. E **79**, 41403 (2009).

[111] M. Ghodrat, A. Naji, H. Komaie-Moghaddam, and R. Podgornik, J. Chem. Phys. **143** (2015).

[112] J. Y. Walz, Adv. Colloid Interface Sc. **74**, 119 (1998).

[113] D. Ben-Yaakov, D. Andelman, and H. Diamant, Phys. Rev. E **87**, 1 (2013).

[114] A. Bakhshandeh, A. P. dos Santos, A. Diehl, and Y. Levin, J. Chem. Phys. **142**, 194707 (2015).

[115] E. Locatelli and E. Bianchi, Soft Matter **14**, 8119 (2018).

[116] R. M. Adar, D. Andelman, and H. Diamant, Phys. Rev. E **94**, 22803 (2016).

[117] S. Zhou, J. Stat. Phys. **169**, 1019 (2017).

[118] A. Onuki and H. Kitamura, J. Chem. Phys. **121**, 3143 (2004).

[119] M. Bier, A. Gambassi, and S. Dietrich, J. Chem. Phys. **137**, 34504 (2012).

[120] M. Bier and L. Harnau, Z. Phys. Chem. **226**, 807 (2012).

[121] R. Evans, "Microscopic theories of simple fluids and their interfaces", in *Liquids at Interfaces*, Vol. 48, edited by J. Charvolin, J. F. Joanny, and J. Zinn-Justin (North Holland, Amsterdam, 1990).

[122] V. S. Bagotsky, *Fundamentals of Electrochemistry* (John Wiley & Sons Inc., Hoboken, 2006).

[123] W. Schmickler and E. Santos, *Interfacial electrochemistry* (Springer, Berlin, 2010).

[124] S. Dietrich, "Wetting phenomena", in *Phase Transitions and Critical Phenomena, Vol. 12*, edited by C. Domb and J. L. Lebowitz (Academic, London, 1988).

[125] M. Schick, "Introduction to wetting phenomena", in *Liquids at interfaces*, edited by J. Charvolin, J. F. Joanny, and J. Zinn-Justin (North Holland, Amsterdam, 1990).

[126] M. Wen and K. Dušek, *Protective Coatings* (Springer, Berlin, 2017).

[127] A. Y. C. Nee, *Handbook of manufacturing engineering and technology* (Springer, London, 2015).

[128] W. B. Russel, D. A. Saville, and W. R. Schowalter, *Colloidal dispersions* (Cambridge University Press, Cambridge, 1991).

[129] R. J. Hunter, *Foundations of colloid science* (Oxford University Press, Oxford, 2001).

[130] B. Lin, *Microfluidics: technologies and applications*, Vol. 304 (Springer, Berlin, 2011).

[131] F. J. Galindo-Rosales, "Complex Fluids and Rheometry in Microfluidics", in *Complex Fluid-Flows in Microfluidics* (Springer, Cham, 2018), pp. 1–23.

[132] A. Naji, D. S. Dean, J. Sarabadani, R. R. Horgan, and R. Podgornik, Phys. Rev. Lett. **104**, 60601 (2010).

[133] A. Naji, M. Ghodrat, H. Komaie-Moghaddam, and R. Podgornik, J. Chem. Phys. **141**, 174704 (2014).

[134] M. Ghodrat, A. Naji, H. Komaie-Moghaddam, and R. Podgornik, Soft Matter **11**, 3441 (2015).

[135] R. M. Adar and D. Andelman, Eur. Phys. J. E **41**, 11 (2018).

[136] R. M. Adar, D. Andelman, and H. Diamant, Adv. Colloid Interface Sc. **247**, 198 (2017).

[137] S. Ghosal and J. D. Sherwood, Proc. Roy. Soc. A **473**, 20160906 (2017).

[138] D. R. Lide, *Handbook of Chemistry and Physics* (CRC Press, Boca Raton, 1998).

[139] L. Bocquet, E. Trizac, and M. Aubouy, J. Chem. Phys. **117**, 8138 (2002).

[140] S. J. Suresh and V. M. Naik, J. Chem. Phys. **113**, 9727 (2000).

[141] J. Y. Walz, Curr. Opin. Colloid Interface Sc. **2**, 600 (1997).

[142] J. Als-Nielsen and D. McMorrow, *Elements of modern X-ray physics* (John Wiley & Sons, New York, 2001).

[143] S. Dietrich and A. Haase, Phys. Rep. **260**, 1 (1995).

[144] J. D. Jackson, *Classical electrodynamics* (Wiley, Hoboken, 1999).

[145] A. C. Maggs and R. Podgornik, Soft Matter **12**, 1219 (2016).

[146] A. Bakhshandeh and M. Segala, J. Mol. Liq. **294**, 111673 (2019).

[147] L. Šamaj and E. Trizac, Phys. Rev. E **100**, 42611 (2019).

[148] C. McCallum, S. Pennathur, and D. Gillespie, Langmuir **33**, 5642 (2017).

[149] L. B. Bhuiyan and C. W. Outhwaite, Phys. Chem. Chem. Phys. **6**, 3467 (2004).

[150] L. B. Bhuiyan, C. W. Outhwaite, D. Henderson, and M. Alawneh, Mol. Phys. **105**, 1395 (2007).

[151] M. Valiskó, T. Kristóf, D. Gillespie, and D. Boda, AIP Advances **8**, 025320 (2018).

[152] U. Kaatze and D. Woermann, J. Phys. Chem. **88**, 284 (1984).

[153] I. K. Snook and D. Henderson, J. Chem. Phys. **68**, 2134 (1978).

[154] I. Ibagon, M. Bier, and S. Dietrich, J. Chem. Phys. **138**, 214703 (2013).

[155] T. M. Fischer and M. Lösche, "Pattern formation in Langmuir monolayers due to long-range electrostatic interactions", in *Molecules in Interaction with Surfaces and Interfaces* (Springer, 2004), pp. 383–394.

[156] P. G. De Gennes, X. Hua, and P. Levinson, J. Fluid Mech. **212**, 55 (1990).

[157] C. Rascón and A. O. Parry, Phys. Rev. Lett. **94**, 96103 (2005).

[158] M. Mußotter and M. Bier, Phys. Rev. E **96**, 32605 (2017).

[159] A. Reindl, M. Bier, and S. Dietrich, J. Chem. Phys. **146**, 154704 (2017).

[160] L. Qing, Y. Li, W. Tang, D. Zhang, Y. Han, and S. Zhao, Langmuir **35**, 4254 (2019).

Danksagung

An dieser Stelle möchte ich noch die Gelegenheit nutzen, den Menschen zu danken, ohne deren Unterstützung es diese Dissertation nicht gegeben hätte.

Zuallererst gilt mein Dank Herrn Prof. Dr. Siegfried Dietrich. Vielen herzlichen Dank dafür, dass Sie mir diese Arbeit ermöglicht haben. Für Ihre herausragende Expertise und Ihre umfangreiche Erfahrung, mit der Sie nicht nur mich, sondern bereits viele frühere Generationen von Doktoranden und jungen Wissenschaftlern unterstützt und an die Forschung herangeführt haben, bewundere ich Sie sehr. Insbesondere möchte ich Ihnen auch für Ihre stets freundliche, hilfsbereite, ermutigende Art und die Freiheit, selbstständig arbeiten und eigene Ideen verfolgen zu können, danken. Ich habe die vergangenen Jahre an Ihrem Institut und die angenehme und kooperative Atmosphäre, die dort herrscht und nicht zuletzt durch Sie gelebt wird, sehr genossen.

Außerdem möchte ich Herrn Prof. Dr. Markus Bier aufrichtig danken. Ich weiß nicht, wie der Ausdruck „eine offene Tür haben“ auf jemanden besser passen könnte. In all den Jahren hast Du mich bei unzähligen Fragen und Problemen unterstützt, Du standest mir stets mit Rat und Tat zur Seite und hast mich immer freundlich, offen und hilfsbereit begleitet. Deine Begeisterung für die Materie war immer spürbar, absolut ansteckend und ich danke Dir herzlichst für all Deine Arbeit, ohne die diese Dissertation nicht möglich gewesen wäre.

Des Weiteren möchte ich Herrn Dr. Nima Farahmand Bafi, Herrn Dr. Hendrik Bartsch und all den anderen Kollegen unserer Abteilung für die offene, humorvolle und stets kollegiale Atmosphäre danken, in der ich in den letzten Jahren lernen und arbeiten durfte. Auch Frau Anke Geigle möchte ich für die zuvorkommende und freundliche Hilfe bei den verwaltungstechnischen Problemen des Doktorandenalltags danken.

Abgesehen von den Menschen des Institutsumfeldes möchte ich an dieser Stelle auch meiner Familie meinen zutiefst empfundenen Dank aussprechen. Ihr habt mich immer unterstützt und mir einen sicheren, liebevollen Rückhalt geboten, mich gefordert, gefördert, ermutigt Neues zu versuchen und nicht vor Herausforderungen zurückzuschrecken. Für all Eure Hilfe und Ratschläge möchte ich Euch von ganzem Herzen danken.

Darüber hinaus gilt mein Dank meiner Frau Johanna. Ohne Dich, Deine tagtägliche Rückendeckung, Deine immer aufbauende, aufmunternde Art und Deine liebevolle Zuneigung wäre mein Leben ein völlig anderes. Deine Begeisterungsfähigkeit, Dein Frohsinn und Deine Lebensfreude sind ansteckend und helfen durch alle Rückschläge, die im Verlauf einer Doktorarbeit so auftreten. Für all das und noch so vieles mehr, insbesondere auch die viele Hilfe beim Erstellen und Korrigieren dieser Arbeit, möchte ich Dir von ganzem Herzen danken.

Last but not least möchte ich außerdem ganz ehrlich und herzlich meinen Freunden aus dem gemeinsamen Physikstudium, Kai Guther, Lukas Fischer, Jonas Heverhagen, Matthias Werner, Toni Peter und insbesondere auch Euch, Matthias und Ruben Pöhnl, danken. Die Jahre mit Euch waren der Knaller und obwohl nicht alle Diskussionen studienrelevant waren, so war auch das ein oder andere fachliche und sehr lehrreiche Gespräch dabei. Ihr habt mir stets das Gefühl gegeben, dass ich mit meinen Fragen, ganz gleich welcher Art, zu Euch kommen kann und die vielen gemeinsamen Stunden haben die letzten Jahre zu einer unvergesslichen Zeit gemacht. Danke dafür!